BARC
newsletter

On Atomistic Modeling & Simulations
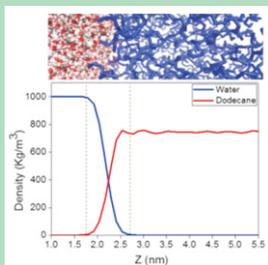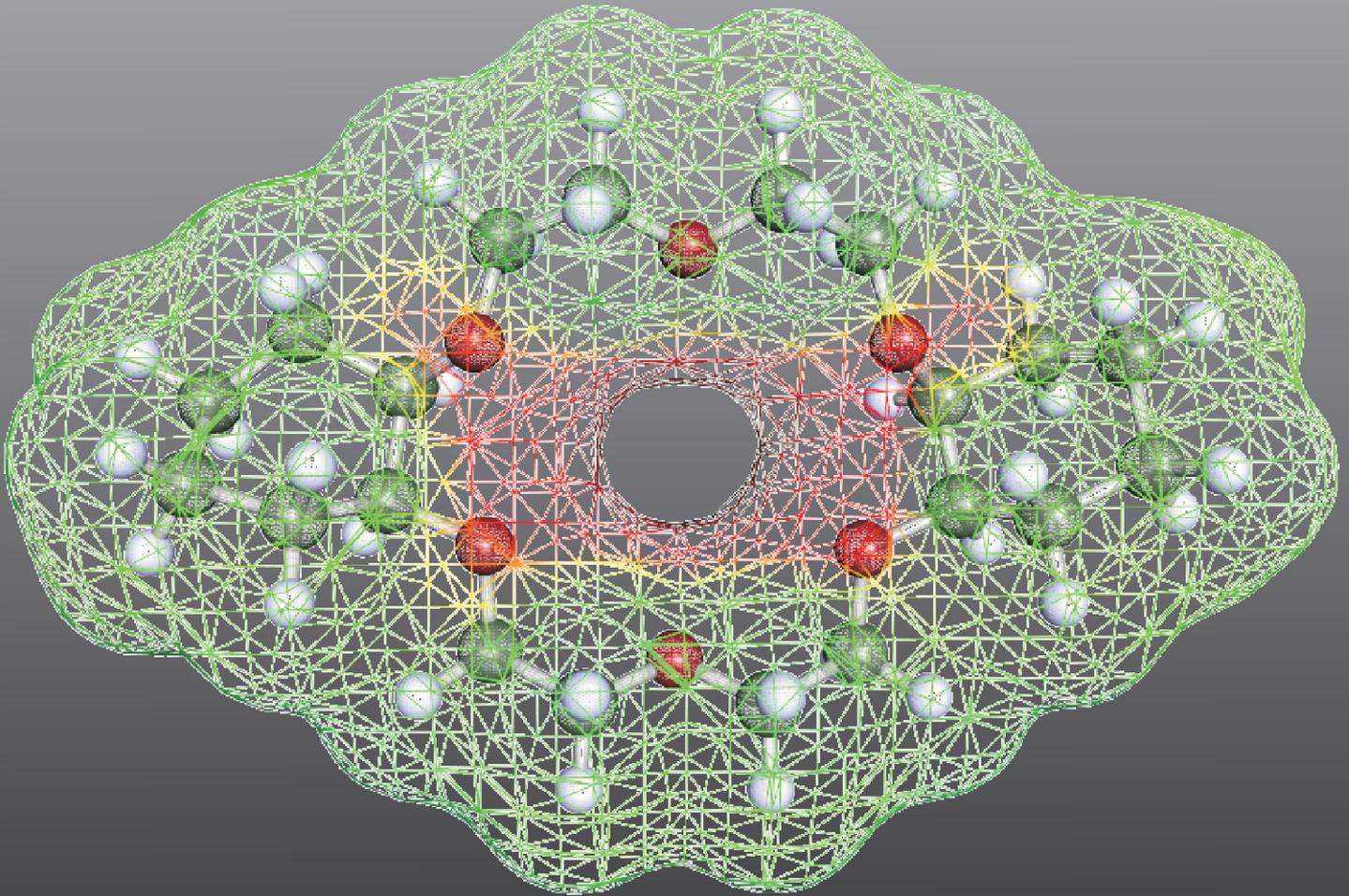
Fuel Reprocessing
Role of Radionuclide-Ligand-Solvent Systems

Acid Dissociation
Microhydration Induced Dissociation of Acid

Bird's eye view of
Bhabha Atomic Research Centre
Mumbai
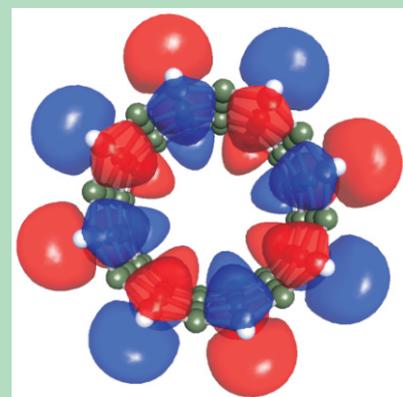
Molecular Orbital of CNT
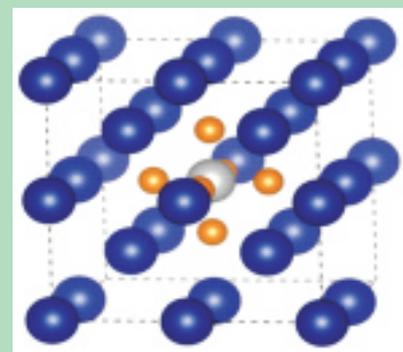
Vacancies-mediated H absorption

Noble gas included vdW complex

On the Cover
Molecular Electrostatic Potential of Dicyclohexano-18-crown-6
@ BARC Photo

associate editor's
MESSAGE

It gives me colossal gratification to bring out this special issue of BARC newsletter on "Atomistic Modeling and Simulations". The scientists and engineers of BARC are engaged in the development of the cutting edge technology by understanding the atomic level events with the aid of Atomistic Modeling and Simulations (AMS). Chemical Engineering Division has played a key role in the field of AMS and hence taken the lead to bring out a special issue on AMS.

Atomistic Modeling and Simulations is a core science area that fosters a broad spectrum of disciplines, including physics, chemistry and biochemistry, materials science, nanoscience, energy and environmental sciences. The AMS field has achieved incredible accomplishment by creating computational models and algorithms that are now used by hundreds of thousands of scientists worldwide, via numerous academic and industrial software packages stemming from decades of research effort. Their translation and deployment have resulted in innovative products coming from the chemical, pharmaceutical, medical and advanced engineering industries that have and expectantly will continue to improve the quality of living.

In this special issue, there are articles covering wide range of topics from electronic structure, atomistic description, molecular dynamics simulations and also multiscale modeling. In this issue, Prof. Maity presented molecular and energy parameters of microhydrated cluster applying electronic structure theory and thus helped to understand several properties of molecules and ions in water medium that has far reaching consequences including extraction behavior. High level *ab initio* based quantum computational techniques were used by the group of Prof. Ghanty to explore the unusual chemical bonding in Noble gas compounds which has a promise for the design of new materials to trap radioactive noble gases in nuclear establishments. The Separation and complexation behavior of trivalent actinides and lanthanides has been investigated using density functional theoretical calculations by A. Bhattacharya. Experimental observations on the complexation of these elements in relevance to their mutual separation could be explained successfully with the help of DFT.

Boda *et. al* presented the molecular assessment of tritium barrier materials from first principles DFT. Their computed results on diffusion, permeation and solubility of hydrogen isotopes in metal is of great technological significance as it helps in controlling the hydrogen induced embrittlement and also in the selection of structural materials for reactors with minimum permeability of tritium. Arya Das *et al* have employed MD simulations and Quantum electronic structure calculations as virtual experimental methods for selection of ligand-solvent systems in nuclear waste reprocessing. Pooja Sahu *et al* have designed nanochannels based membrane for water desalination using MD simulations which might be applied for futuristic nanomembrane based waste water purification. Prof. Arya and group have investigated thermo-physical and diffusional properties of U, Th and Np based MOX fuel using a multi-pronged atomistic simulation approach. The generation of thermo-physical and diffusional properties database will help in the design and fabrication of new fuels and perform safety analysis. Prof. N. Choudhury presented the results of multiscale modelling and simulation as effective approaches towards exploring problems ranging from molecules to materials. These approaches have been used for design of MOF for Xe storage, solvent dependent pattern formation and protein-drag interaction in the development of therapeutic inhibitors of viral shells. Pooja Sahu *et al* have established a methodology for selection of suitable glass composition for vitrification of high-level radioactive waste (HLWs) in nuclear waste reprocessing using atomistic simulations. This provides a microscopic understanding of the glass structure and phenomena associated with the change in glass compositions. The presented results will be of great scientific use for making future glasses in various applications including nuclear waste immobilization. I believe this thematic and dedicated newsletter will help the younger generation for guiding and pursuing research in this highly fascinating area.

(Sk. Musharaf Ali)
Chemical Engineering Division

RESEARCH ARTICLES

Microhydration: Understanding Solute-Solvent Interactions at Molecular Level

*D.K. Maity[1,2]

[1]Director's Office, Bhabha Atomic Research Centre, Trombay, Mumbai-400085, India
[2]Homi Bhabha National Institute, Mumbai-400094, India

ABSTRACT

Structure, molecular properties and energy parameters of microhydrated clusters of a few chemical systems are reported. Ground and excited state calculations are carried out applying sophisticated electronic structure theory to account dispersion interactions accurately. Dissociation of acid molecules in water, understanding of photoacidity and solubility of halogen gases are discussed following studies on microhydrated clusters.

Keywords: Cluster, molecular property, solute-solvent interaction, microhydration, photoacid, first principle calculation.

Introduction

In recent years, the study on microhydration of neutral and charged chemical species has been a subject of intense research both from experimental and theoretical points of view to understand the structural, energetic, spectroscopic, and dynamic aspects of hydration at molecular level.[1-9] This is mainly because of the strong dependency of the properties on size and geometry of the hydrated clusters of these species. When a solute is added to a solvent water medium, the water molecules those are in immediate vicinity of the solute get rearranged to allow the solute going through the hydration process. The electron distribution pattern of the added solute plays the key role to shape up the structure of the water network around the solute. The properties of these solute embedded water clusters provide basic understanding of the fundamental interactions those are responsible for hydration process at molecular level and thus it is important not only to chemists but also to physicists, biologists and researchers in material science. Microhydrated clusters are formed by the step-wise addition of water molecules to a chemical species. These clusters are stabilized by hydrogen bonding. Hydrogen bonds play a key role in determining the three dimensional structures of the cluster. It is known that implicit macroscopic solvation models fail to accurately describe the effect of hydration on the structure and properties of molecules in many cases. Thus, consideration of explicit solvent water molecules is very essential to understand the effect of hydration.

In what follows, computed results of microhydrated clusters of certain interesting systems are presented focusing on three selected molecular properties. Calculations are carried out applying high level electronic structure theory.

Results and Discussion

Acid Dissociation

Acids (AH) are ubiquitous in nature. Acidic solutions play a major role in a wide range of fields. A plethora of chemical, physical and biological phenomena involves acid-water interactions. Be it an enzyme catalysed reaction in a biological system or the formation of cloud condensation nuclei in the atmosphere, it all depends on the proton transfer process between the acid and water molecules, that is, acidity of the acid. Further, acid-water molecular clusters provide an ideal system to study the relation between solvation and reactivity, as ionization of the acid molecule occurs during the progress from molecular clusters to aqueous solution. In macroscopic description, a strong acid signifies an acid that ionizes completely in an aqueous solution whereas a weak acid does not ionize fully in such an environment. Thus, the ability to transfer a proton to a water molecule is the answer to differentiate an acid based on its strength. In the context of the microscopic or molecular level description of the strength of an acid, one may ask a
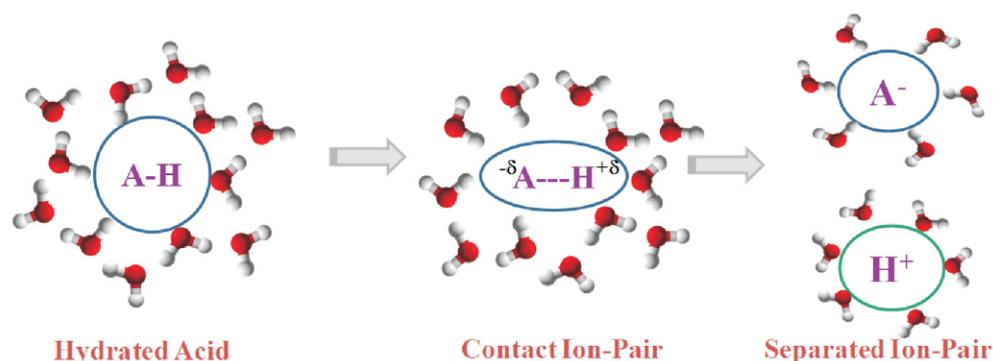
Scheme 1: Schematic representation of hydration of acids. AH represents the acid molecule and the red and grey balls represent oxygen and hydrogen atoms of the water molecule respectively. The reorientation of the water molecules around the acid molecule, the weakening of the A-H bond and formation of solvent separated ion pair is shown.

fundamental question: How much water is required to ionize an acid? The answer to this question involves a microscopic study of the hydration of acids. In acid-water clusters (AH.nH_2O), solute acid molecule forms hydrogen bonds with the solvent water molecules present in the immediate neighbourhood. As a result of intermolecular interactions between the acid molecule and solvent water molecules, the A-H bond of the acid molecule weakens and proton transfer from the acid molecule to solvent water molecules occurs, leading to dissociation of the acid molecule, as depicted in Scheme 1.

The process of hydration of an acid molecule involves formation of contact ion pair followed by solvent separated ion pair, and yields hydrated protons in either Eigen ($H_3O^+ \cdot 3H_2O$) or Zundel ($H_3O^+ \cdot H_2O$) forms. Thus, determining the number of water molecules needed to stabilize the hydrated ion pair will tell us the number of water molecules that are needed to ionize an acid. A few recent theoretical studies report the number of water molecules needed to ionize H_2SO_4, HCl, HNO_3 and $HClO_4$. Experimental reports of proton transfer in hydrated acid molecules are mainly based on matrix isolation and thin-film IR studies. Based on the study of amorphous thin films of HNO_3 and water, it is reported that three solvent water molecules are required to stabilize ionized HNO_3. Gas-phase ultra-fast pump-probe experiments on HBr-water clusters led to the conclusion that five water molecules are needed to induce ionization of HBr.[5] High resolution mass-selective infrared laser spectroscopy are also employed to observe the formation of hydronium ion in the tetra-hydrated cluster of HCl, within superfluid He cluster, at a temperature of 0.37 K. Ab initio molecular dynamics simulations technique used to explore the free energy surface of the HCl-water system and to explain how the proton transfer barrier is surmounted under the cryogenic conditions of the experiment. The addition of a fourth water molecule to the unionized tri-hydrate is predicted to yield a "partially aggregated" complex which then transforms into the structure containing Cl^- and $H_3O^+(H_2O)_3$.[3]

The A-H bond length is an indicator for ionization of acid molecules in hydrated acid clusters. Upon hydration, due to hydrogen bonding between the proton of the acid molecule and O atom of the nearest water molecule, weakening of the A-H bond occurs. This leads to elongation of A-H bond. With increase in size of the hydrated acid cluster, the A-H bond length also increases and finally after dissociation of the acid, the A-H bond distance would be in the range of H-Bond lengths. There is a corresponding decrease in the H..O H-bond distance, which finally reduces to O-H covalent bond length of the hydronium ion, upon acid dissociation. These distances are usually determined computationally, as their experimental measurement is difficult because the increase is usually a few hundredths of an angstrom.

Stabilization and interaction energy

Based on the geometry of the most stable conformers of free and hydrated molecules, energy parameters are defined to understand the molecular interactions existing within the molecular clusters. Solvent-induced stabilization energy of hydrated clusters of the molecule, M.nH_2O, is defined as $E_{stab} = E_{M.nH2O} - (n.EH_2O + E_M)$, where, $EM.nH_2O$ refers to the energy of the hydrated cluster, M.nH_2O, E_{H2O} and E_M correspond to the energy of a single water and molecule, respectively. By definition, E_{stab} represents stabilization of the molecule due to its interactions with the solvent water molecules. E_{stab} gives the stabilization of the molecule on account of addition of solvent water molecules, which includes both solute-solvent as well as solvent-solvent interactions, as depicted in Scheme 2a for
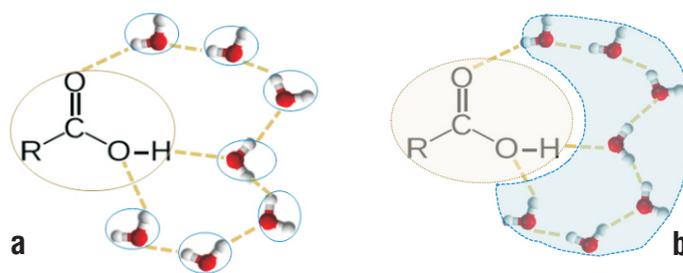
Scheme 2: a) Schematic diagram depicting the solvent stabilization energy, E_{stab}, for a hydrated carboxylic acid system, RCOOH.nH_2O. This energy parameter includes solute-solvent as well as solvent-solvent interactions. The red and white balls represent oxygen and hydrogen atoms respectively of water molecule. b) Schematic diagram depicting the interaction energy, E_{int}, for a hydrated carboxylic acid system, RCOOH.nH_2O. This energy parameter contains only solute-solvent interactions. The red and white balls represent oxygen and hydrogen atoms respectively of water molecule.

carboxylic acid system. To isolate the solute-solvent interactions from the solvent stabilization energy, excluding any solvent-solvent stabilization, interaction energy, E_{int} is defined as $E_{int} = E_{M-nH2O} - (E_{(H2O)n} + E_{M^*})$. $E_{(H2O)n}$ and E_{M^*} correspond to the energy of the water cluster and the acid molecule, respectively, in the same geometry as is present in the hydrated acid cluster.

For evaluation of $E_{(H2O)n}$, solute part RCOOH is removed from the optimized geometry of the cluster, followed by a single-point energy calculation. Following a similar procedure for the evaluation of E_M, the $(H_2O)_n$ part is removed from the optimized geometry of the hydrated cluster, followed by a single-point energy calculation. Thus, the interaction energy includes only solute-solvent interactions, removing all solvent-solvent interactions as depicted in Scheme 2b. The calculations are done at ωB97X-D/aug-cc-pVDZ level of theory.

The plot of calculated interaction energy (E_{int}) vs. n, number of water molecules for HCOOH.nH_2O clusters are also displayed in Fig. 1a. Calculated stabilization and interaction energy is very close for a few small size clusters. But when inter molecular hydrogen
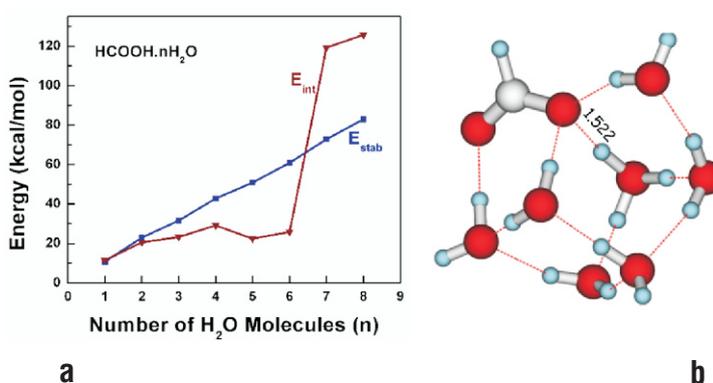
Fig.1: a) Plot of calculated stabilization energy, E_{stab} and interaction energy, E_{int} at B97XD/aug-cc-pVDZ level in kcal/mol vs. n, number of water molecules for HCOOH.nH_2O clusters. A minimum of seven water molecules are needed to dissociate formic acid molecule; b) Optimized minimum energy structure of HCOOH.$7H_2O$ cluster showing bond distance of the dissociating O-H bond.

bond among water molecules starts to build up; solvation energy surpasses the interaction energy. The variation of solvent stabilization energy with size of the cluster (n) is observed to be linear. Interaction energy calculated for cluster size (n=4-6) is much smaller than solvent stabilization energy for same size clusters. Note that interaction energy is much higher for charged system. Thus, variation of interaction energy with size of the cluster (n) shows sharp increase for hepta- and octa- hydrated cluster as these represents charge separated state of formic acid. The interaction energy (E_{int}) is the measure of the interaction between formic acid and solvent water units. Interaction energy of these clusters is decomposed into different components and electrostatic interaction is observed to be the major contributor.[7]

The structure of a hydrated acid cluster depends on the delicate balance between the hydrogen bond stabilization, coulombic attraction and proton transfer energy. An interesting point noted is the extra stability of hydrogen bonded closed ring conformers of the hydrated acid clusters, relative to open chain conformers. This is not surprising as the number of stabilizing hydrogen bonds are more in case of the closed ring conformers. An elongation is seen in the acidic O-H bonds of the hydrated acid clusters, in all cases, with increase in number of water molecules. This is expected as the hydrogen bonds between the acid molecule and the water molecules causes weakening of the acidic hydroxyl bonds. It is observed that a minimum of six water molecules are needed to dissociate trifluoroacetic acid molecule while eight water molecules are needed for the dissociation of benzoic acid molecule. In case of oxalic acid molecule, the dissociation of the first acidic proton requires the presence of at least seven water molecules. The structure of the ionized acid-water cluster resembles that of the Eigen cation interacting with the carboxylate anion surrounded by the remaining water molecules. The proton transfer in $CH_3COOH.nH_2O$ and second proton transfer in $(COOH)_2.nH_2O$ are not observed even when n=8. The proton transfer from an acid molecule to the solvent water molecules in a hydrated acid cluster can be explained by the stronger stabilization of the contact ion pairs upon hydration, compared to the neutral acid molecule.

Photoacids

Photo acids undergo significant enhancement in their acidity upon electronic excitation. This leads to excited state proton transfer to the solvent. The change in electron density distribution of a photo acid can be determined from its excited state acidity constant. This information is of much interest to both photo chemists, who can study the differences in reactivity of molecules in ground and excited state, and theoretical chemists, who can calculate the excited state electronic structure and the nature of the transitions involved. The significant change in acidity of these molecules makes them an ideal system to probe solute-solvent interactions and solvent polarities. Photo acids can be used as molecular probes for determining the structural transitions of proteins under various conditions. Water accessibility in biological surfaces can also be probed using photo acids. The excited state pKa of a photo acid is generally determined from the Farster cycle, based on absorption and emission data. It can also be determined using photo-potentiometry.

In aqueous solution, aromatic compounds like phenol and 2-naphthol have ground state pKa values of 10.0 and 9.2 respectively, while their excited state pKa values are just 3.6 and 2.8 respectively. Theoretical calculations to explain excited state proton transfer in phenols has been reported. Two different explanations

have been proposed for the increase in acidity in the first excited singlet state. One proposition attributes the increase in acidity to a charge transfer in the photo acid. According to the other proposition, the enhanced excited state acidity is largely determined by the deprotonated photo acid.

It is reported that the acidity constants of ground and first excited triplet states of 2-naphthol are comparable while that of the first excited singlet state differ by a factor of ~10[6]. The studies were based on flash photolysis, fluorescence and phosphorescence measurements. They provide a qualitative explanation for this observation based on electron density. The difference in the pKa value of ground state and excited states of 2-naphthol could be reflected in the number (n) of water molecules needed for their ionization. Studies on microhydration of 2-naphthol (nap) at ground (nap_{S0}), first excited triplet (nap_{T1}) and first excited singlet (nap_{S1}) states is carried out applying DFT based electronic structure method considering a suitable functional for excited sate calculations. It is seen that even in the presence of four water molecules, proton transfer from naphthol to water molecules is not observed for either ground or first excited triplet state. However, proton transfer becomes a barrier-less process for first excited singlet state of tetra-hydrate of naphthol.[8]

A rigid potential energy scan of the acidic O-H bond of nap.4H$_2$O at the first excited singlet state reveals that in the presence of four water molecules, the acidic proton transfer from nap to the neighbouring water molecule becomes a barrier-less process, as shown in Fig. 2. In fact, in the first excited singlet state, the tetra-hydrate becomes unstable at O-H bond distances less than 1.4 Å. The potential energy profiles show that a barrier exists for proton transfer from nap to solvent water molecules in all cases except the tetra-hydrate of nap at the first excited singlet state. In case of first excited singlet state spontaneous dissociation of the O-H bond is observed for the tetrahydrate cluster of 2-napthol. This is in line with the experimentally observed fact that first excited singlet state is
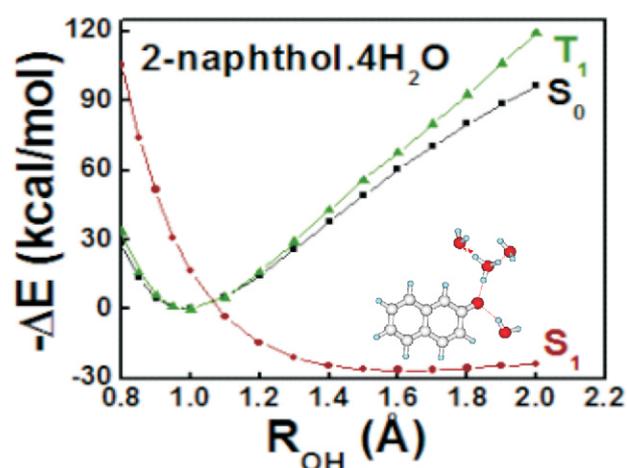
Fig.2: Rigid potential energy scan carried out applying TD-DFT at CAM-B3LYP/ aug-cc-pVDZ level for O-H bond of 2-naphthol.4H$_2$O, at ground, first excited triplet and singlet state. ΔE gives the relative energy of the system at each point of the scan of the dissociating O-H bond, with respect to the energy of the equilibrium geometry. Curves marked as S_0, T_1 and S_1 represent potential energy surfaces of ground, first excited triplet and singlet states respectively of 2-naphthol.4H$_2$O, upon increasing the bond distance of dissociating O-H bond of the acid.

Species $X_2 \cdot n H_2O$	Stabilization energy of $X_2 \cdot n H_2O$ clusters (kcal/mol)		Interaction energy of $X_2 \cdot n H_2O$ clusters (kcal/mol)	
	X=Cl	X=Br	X=Cl	X=Br
$n = 1$	2.85	3.86	3.07	4.11
$n = 2$	9.85	5.52	4.36	5.76
$n = 3$	9.88	13.53	3.91	7.74
$n = 4$	25.82	27.68	7.42	9.58
$n = 5$	28.24	30.23	8.49	11.02
$n = 6$	45.66	47.87	9.31	11.66
$n = 7$	65.00	60.03	4.55	11.32
$n = 8$	73.25	71.26	6.57	13.73

Table 1. Calculated stabilization and interaction energy in kcal/mol for $X_2 \cdot n H_2O$ systems (X=Cl, Br; n=1-8) at MP2/6-311++G(d,p) level of theory.

more acidic than the ground and first excited triplet state. It is worth mentioning that no such bond dissociation is predicted in water medium when the computation is performed considering macroscopic solvent model.

Solubility of Cl_2 / Br_2 gas in water

Solubility of bromine gas is 14.9 gm compared to 0.729 gm for chlorine gas in 100 gm of water at room temperature. As these molecular species (Cl_2/ Br_2) are having zero dipole moment, one has to apply explicit solvation model to study the solvent effect rather than taking a macroscopic solvation model like Onsager's continuum reaction field model. The molecular interaction between a neutral solute and solvent water molecules as well as the hydrogen bonding interactions among the solvent water molecules can be examined in such studies placing explicit solvent molecules around a solute. Such studies provide information on the evolution of hydration motifs of X_2 (X=Cl & Br) systems in water. Electronic polarization in condensed phase can guide to evolve polarizable point charge model in studying various properties and processes including solvent effect. Thus, a systematic study in halogen-water clusters are of considerable interest to understand solute-solvent and solvent-solvent intermolecular interactions in water medium and hence for molecular modelling in aqueous phase. Calculated structures suggest that Br_2 exists as a charge separated ($Br^{+\delta}$-$Br^{-\delta}$) entity in the hydrated clusters but Cl_2 does not exist as a charge separated ion pair in presence of solvent water units.[9] Table 1 presents calculated stabilization and interaction energy of Cl_2 and Br_2 hydrated clusters. One can see from the table that solvent stabilization energy increases steadily for both Cl_2 and Br_2 hydrated clusters. However, interaction energy profiles show different features for the two different gases. In case of $Br_2 \cdot n H_2O$ clusters the said energy increases and for $Cl_2 \cdot n H_2O$ clusters it increases slowly showing fluctuations and finally reaches to a lower value. The numerical values are smaller than those for hydrated clusters of Br_2. Calculated higher interaction energy for $Br_2 \cdot n H_2O$ clusters than that for $Cl_2 \cdot n H_2O$ cluster is able to explain the higher solubility of bromine gas over chlorine gas in bulk water.

Conclusion

Implicit macroscopic solvation models fail to describe the effect of hydration on the structure and properties of several class of molecules. Explicit hydration (microhydration), leading to dissociation of acid molecules are studied. Calculated stabilization energy increases linearly on successive addition of solvent water molecules whereas sudden increase in interaction energy is predicted for the hydrated clusters of acid indicating dissociation of the acid molecules. Rigid potential energy scan for O-H bond of $RCOOH \cdot n H_2O$ cluster maybe used as an indicator to study microhydration in acid molecules to track proton transfer and formation of contact ion pairs. Microhydration studies of 2-naphthol at ground, first excited triplet and singlet states are carried out using TD-DFT. It is seen that even in the presence of four water molecules, proton transfer from 2-naphthol to water molecules is not observed for either ground or first excited triplet state. However, proton transfer becomes a barrier-less process for first excited singlet state of tetra-hydrate cluster of 2-naphthol. Higher solubility of Br_2 gas over Cl_2 gas in water could be explained based on studies of microhydrated clusters of Br_2 and Cl_2. Overall, studies on microhydration is very important to understand several properties of molecules and ions (including metal ions) in water medium and has far reaching consequences including extraction behaviour.

Corresponding Author*

D.K. Maity (dkmaity@barc.gov.in)

References

[1]   X. Wang, X. Yang, J.B. Nicholas, L. Wang, *Science*, 2001, **94**, 1322.

[2]   M. Miyazaki, A. Fujii, T. Ebata, Mikami, *N. Science*, 2004, **304**, 1134.

[3]   J.M. Headrick, E.G. Diken, R.S. Walters, N.I. Hammer, R.A. Christie, J. Cui, E.M. Myshakin, M.A. Duncan, M. A. Johnson, K.D. Jordan, *Science*, 2005, **308**, 1765.

[4]   A. Gutberlet, G. Schwaab, Ö. Birer, M. Masia, A. Kaczmarek, H. Forbert, M. Havenith, D. Marx, *Science*, 2009, **324**. 1545.

[5]   K.R. Leopold, *Annu. Rev. Phys. Chem.* 2011, **62**, 327.

[6]   D.B. Millet, *Nature Geoscience*, 2012, **5**, 8.

[7]   D.K. Maity, *J. Phys. Chem. A*, 2013, **117**, 8660.

[8]   K. Parvathi, R. Kar, D.K. Maity, *J. Phys. Chem. A*, 2018, **122**, 929.

[9]   A.K. Pathak, T. Mukherjee, D.K. Maity, *J. Phys. Chem. A* 2008, **112**, 744.

Exploration of Unusual Chemical Bonding in Noble Gas Compounds

Ayan Ghosh[1,3] and *Tapan K. Ghanty[2,3]

[1]Laser and Plasma Technology Division, Beam Technology Development Group,
Bhabha Atomic Research Centre, Mumbai-400 085, India
[2]Bio-Science Group, Bhabha Atomic Research Centre, Mumbai-400 085, India
[3]Homi Bhabha National Institute, Mumbai-400094, India

ABSTRACT

Noble gases were considered as highly inert and unreactive in the early days. In 1933, Pauling first predicted that the heavier noble gas atoms, *viz.*, Kr and Xe can form stable molecules with the other elements since their less strongly bound valence electrons are at a large distance from their nuclei and hence more susceptible to chemical bond formation. Successful experimental identification of the first noble gas compound, $XePtF_6$, by Bartlett in 1962 not only validates the Pauling's prediction but also alters the fundamental perception of the "inert" nature of noble gas elements. Although several different kinds of noble gas compounds have been reported, there are few interesting classes of noble gas compounds that attract the scientists to a larger extent in the present era, *viz.*, various kinds of noble gas (Ng) insertion compounds, 'superstrong' van der Waals (vdW) complexes, and entrapment of Ng atoms in various materials. In this article, we aim to review this growing field of noble gas chemistry based on our recent findings on few series of novel Ng insertion compounds, 'superstrong' vdW complexes, and Ng encapsulated molecular cages which are predicted through high level *ab initio* based quantum computational techniques.

Keywords: Noble gas, Chemical bonding, vdW complexes, Stability, DFT, abinitio quantum computations.

Introduction

In general, the bulk properties of the noble gases are mainly dependent by the weak van der Waals forces acting between the atoms. The rise of melting point, boiling point, enthalpy of vaporization, density, and solubility on going from helium to radon is due to the increase in the polarizibility since the attractive force increases with the increase in size of the atoms. The electronic configuration of noble-gas atom was first reported by Kossel[1] and Lewis[2] in 1916 emphasizing the most stable electronic configuration among all the elements exists in nature. Due to full valence electron shell, the Ng atoms are extremely reluctant to form chemical bond with the other elements[3] indicating the inert nature of the noble gas atoms. Mendeleev assigned them as 'Group 0' as a separate group in the periodic table and 'noble gas notation'[4] is broadly used to represent any electronic configuration of any other element in the periodic table.

The remarkable discovery of first noble gas compound, $Xe[PtF_6]$[5] by Bartlett, attracted the scientists to explore the field of noble gas chemistry. The successful identification of the HArF [6] molecule possessing unusual H-Ar covalent bonding by Khriachtchev *et al.* through low temperature matrix isolation infrared spectroscopic technique, has revolutionized the field of 'noble gas chemistry'. Since then, there is a surge to explore the field of noble gas chemistry for both theoreticians and experimentalists and has experienced a renaissance during the past two decades.[7-14] In recent years, a unique category of novel noble gas hydrides of the type HNgY (Ng = Ar, Kr, and Xe; Y = electronegative element or group) has received considerable attention among researchers.[7,8] Various neutral or ionic insertion molecules of noble-gas atoms possessing environmental importance, like HOX [9] (X = F, Cl, Br), H_3O^+ [10] and species with astronomical significance, such as (HCO^+) [11], (Hn_2^+) [12] and so on have been theoretically investigated by us using various computational methods. The first ever noble gas-containing compounds had been detected in space, i.e., noble gas hydride cations ($^{36}ArH^+$) in the Crab Nebula by Barlow and co-workers.[13] Of late, Khriachtchev *et al.*[14] has successfully prepared and characterized one of the Ng insertion molecules, HXeOBr, using IR spectroscopic technique which was theoretically predicted earlier by our group.[9]

The bonding between noble gas and noble metal is completely unusual from the view point of their extreme inert nature. First noble gas-noble metal compounds, $XeAu^+$ and $XeAuXe^+$, were experimentally identified through mass spectrometry in 1998 by Schroder *et al.*,[15] although they were first conceived theoretically by Pyykko, in 1995.[16] Later, Seidel and Seppelt[17] had successfully synthesized the first thermally stable $[AuXe_4][Sb_2F_{11}]_2$ complex containing Ng-noble metal bond. A series of compounds containing Ng-M bond (Ng = Ar, Kr, and Xe; M = Au, Ag, and Cu), *viz.*, NgMX (X =F, Cl, and Br) have been investigated both experimentally as well as theoretically.[18]

A single gold atom can exhibit chemistry analogous to the hydrogen atom found in $SiAu_n$ clusters.[19] By employing this gold-hydrogen analogy, earlier our group have explored the feasibility study of noble gas inserted compounds involving noble metal atoms, *viz.*, MNgF and MNgOH (M = Cu, Ag, and Au; Ng = Ar, Kr, and Xe) using *ab initio* quantum chemical calculations.[20] Recently, Fielicke and co-workers[21] raised a point about the controversial

nature of the noble gas- noble metal bonding by proposing trimeric coinage metal cluster as a prototype system to unravel the nature of Ar- M bonding (M = Ag and Au). Motivated by the aforementioned findings, we have explored the unprecedented enhancement of Ng- M bonding strength in NgM_3^+ (Ng = Ar, Kr, and Xe; M = Cu, Ag, and Au) ions through hydrogen doping by employing various *ab initio* based techniques.[22]

One of the major issues in nuclear fuel reprocessing and reactor accidental scenarios is to manage radioactive fission gases including Xe and Kr. Due to the extreme inert nature of noble gases, it is very difficult to trap the radioactive noble gases in suitable matrix by van der Waals interactions using simple physisorption process. Theoretical modelling is necessary to select a suitable metal-organic framework (MOF) based materials required for the adsorption/separation of radioactive noble gas due to its high intake capacity, better selectivity and tunable chemical properties. In recent times, scientists have exhaustively studied the adsorption of Ng atom with a large number of MOF systems, viz., Sb-MOF-2,[23] Sb-MOF-1,[24] M-MOF-74,[25] etc. Very recently, our group has reported theoretically the enhancement of the adsorption of fission gases Xe and Kr on doped graphene, graphyne and graphidiyne.[26] Moreover, enhancement of Ng adsorption on doped MoS_2 monolayer and confined induced adsorption of Ng on MOF MFM-300 has been found very recently by us and found to be promising.[27]

As far as the nuclear fuel is concerned, the reactivity of noble gas atoms towards the uranium atoms is one of the most important aspects in nuclear reactor. In 2002, Andrews and co-workers have found first Ng-U (Ng = Ar, Kr, Xe) bonding in CUO molecule formed from the reaction of laser-ablated U atoms with CO in low temperature noble gas matrices through IR spectroscopic techniques.[28] Unusual IR shift in the U-O and U-C stretching modes confirms the generation of CUO·Ng molecules where U-Ar bond length and binding energy have been found to be 3.16 Å and 3.2 kcal mol^{-1}, respectively.[28] Subsequently, several $CUONg_nNg'_m$ molecules have been prepared and characterized experimentally supported by theoretical calculations.[29] Evidence for direct U-Ar bonding has also been reported by the same group of scientists for investigating the electronic structure of the UO_2 molecule at low temperature Ng matrices through IR spectroscopy with the formation of UO_2Ar, $UO_2(Ar)_5$,[30] and $UO_2(Ng)_4$ (Ng = Ne, Ar).[31]

Recently, Chattaraj and co-workers have studied confinement-induced binding of noble gas atoms within magic BN-fullerenes like $B_{12}N_{12}$ and $B_{16}N_{16}$[32] and BN doped carbon nanotubes.[33] Moving one step forward, we have also explored the structure and stability of the Ng encapsulated inorganic fullerene, viz., plumbaspherene

($Ng@Pb_{12}^{2-}$) and stannaspherene ($Ng@Sn_{12}^{2-}$) followed by molecular dynamic simulations.[34] The superelectrophilic behaviour of $B_{12}Cl_{11}^-$,[35] $B_{12}(CN)_{12}^{2-}$ and its fragment $[B_{12}(CN)_{11}]^-$ ion[36] is confirmed by their spontaneous covalent bonding with Ng atoms and the formation of thermodynamically stable $[NgB_{12}Cl_{11}]^-$ (Ng = Kr, Xe) and $[NgB_{12}(CN)_{11}]^-$ (Ng = Ar) compounds. Very recently, for the first time we have predicted thermodynamically stable dianionic noble gas compounds, viz., $[NgBeB_{11}(CN)_{11}]^{2-}$ (Ng = Ar, Kr, Xe),37 and $B_{12}Ng_{12}F_{12}^{2-}$ (Ng = Kr, Xe).[34]

A Typical Bonding in Novel Class of Noble Gas Insertion Compounds

Motivated from the discovery of HArF by Räsänen and co-workers,[6] we have predicted interesting noble gas insertion compounds by using ab initio quantum chemical techniques, viz., protonated nitrogen cations ($HNgN_2^+$),[12] formyl cations ($HNgCO^+$),[11] thioformyl cations ($HNgCS^+$)[39] (Fig.1(i)), hydride ions of boron ($HNgBF^+$),[40] protonated silicone monoxide cations ($HNgOSi^+$)[41] (Fig. 1(ii)), hypohalous acids (HXeOX; X = F, Cl, Br),[9] hydroxides of icosagens (HYO-HOY; Y = B, Al),[42] and hydronium ions ($HNgOH_2^+$)[10] (Fig.1(iii)),. Apart from the noble gas hydrides, we have also explored the possibility for the existence of noble gas halo compounds, viz., fluoro(sulphido)boron (FNgBS),[43] halocarbenes (FNgCX; X = F, Cl, Br, I)[44] (Fig.1(iv)), formyl cations (XNgCO$^+$; X = F, Cl).[45] We have also predicted the metastable metal-noble gas complexes, viz., XM-Ng-F (X = H, F; M = Be, Mg),[46] F-Ng-MF$_2$ (M = B, Al).[47] Exploiting the gold-hydrogen analogy, Ng insertion compounds involving most unusual noble gas-noble metal bonding, viz., MNgF and MNgOH (M = Cu, Ag, and Au; Ng = Ar, Kr, and Xe) have been predicted by us in the recent past.[20] All these compounds possess closed-shell geometries and they have been found to be singlet in their respective potential energy surfaces.

The CCSD(T) computed H- Ng bond length values have been found to be 0.766- 1.620 Å in $HNgCS^+$,[39] 0.764- 1.610 Å in $HNgCO^+$,[11] 0.765- 1.607Å in $HNgN_2^+$,[12] 0.771- 1.620Å in $HNgBF^+$,[40] 0.751- 1.615Å in $HNgOSi^+$[41] and 0.754- 1.609 Å in $HNgOH_2^+$[10] ions on going from He to Xe whereas the corresponding H–Ng bond lengths are from 0.824 to 1.680 Å in HNgF species and from 0.776 to 1.607 Å in bare H- Ng$^+$ ions.[48-50] Due to the close proximity of the H- Ng bond lengths, the comparable H- Ng bond strength with HNgF and bare HNg$^+$ ions indicates that there exists a strong bonding between the H and Ng atom in all the predicted ions. On going from He to Xe, the Ng- C bond lengths (2.036- 2.872 Å) in HNgCS$^+$ ions are found to be smaller than Ng- B (2.240- 3.090 Å) in HNgBF$^+$, Ng- N (2.138- 3.093 Å) in HNgN$_2^+$ and Ng- C (2.221- 3.124 Å) in HNgCO$^+$ bond lengths as obtained by CCSD(T) method.
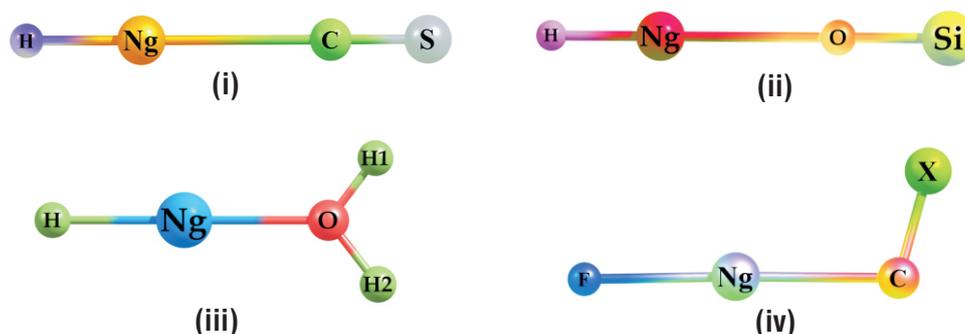
Fig.1: Optimized minima structures of (I) HNgCS$^+$, (ii) HNgOSi$^+$, (iii) HNgOH$_2^+$, and (iv) FNgCX compounds.
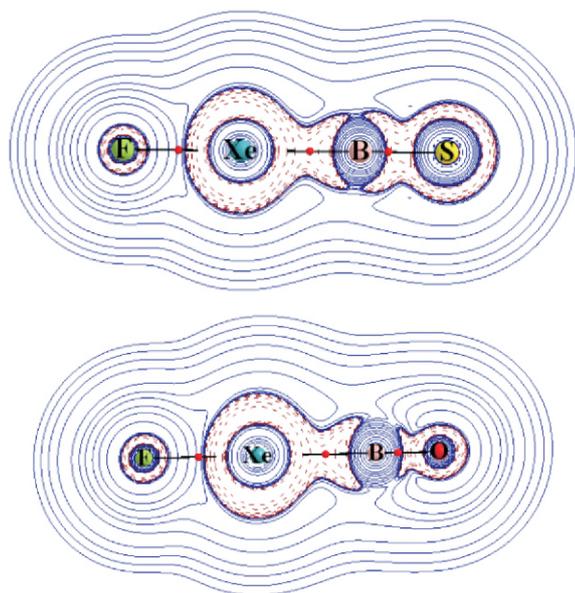
Fig.2: Contour plots of Laplacian of electron density ($\nabla^2\rho$) of (i) FXeBS, (ii) FXeBO, at the respective molecular plane calculated at the B3LYP level. The dotted lines are the regions of charge concentration and solid lines are the regions of charge depletion.

The contour lines corresponding to the Laplacian ($\nabla^2\rho$) distribution (Fig.2) show more or less a uniform charge accumulation around the noble gas-boron-sulfur region in the FNgBS molecules; however, it is somewhat nonuniform in the case of FNgBO systems. Nevertheless, charge concentration in the Ng-B bonding region indicates that the Ng-B bond is rather covalent in nature whereas B-S bond is found to be more covalent than the B-O bond.

Stimulated by the open shell noble gas insertion compound with a doublet ground electronic state HXeO ($^2\Sigma$),[51] ^{2}HXeCC[52] and ^{3}FN–XeF$^+$,[53] for the first time we have predicted the neutral Ng insertion compound in the triplet electronic state, ^{3}FNgY (Ng = Kr, Xe; Y = N, P).[54] Subsequently, we have reported the neutral Ng insertion compound with heavier pnictides, ^{3}FNgY (Ng = Kr, Xe; Y = As, Sb, Bi) with triplet state.[55] Similar to the singlet Ng hydrides, we have also predicted the first Ng hydrides, *i.e.*, Ng inserted ketenyl cations (^{3}HNgCCO$^+$)[56] in the triplet ground state. For all the predicted ^{3}FNgY and ^{3}HNgCCO$^+$ species, significantly higher singlet-triplet energy gaps would prevent intersystem crossing (ISC) even at a very low temperature.

All the predicted species are found to be thermodynamically stable with respect to all possible 2-body and 3-body dissociation channels, except the dissociation path leading to the respective global minimum products. Nevertheless, all these compounds are found to be kinetically stable with finite barrier heights corresponding to their transition states, which are connected to their respective global minima products. The atoms-in-molecules (AIM) analysis strongly reveals that there exists conventional chemical bonding with the noble gas atom in all the predicted compounds.

'Superstrong' vdW Complexes with Ng: H Doping in NgM$_3^+$ (M = Noble Metal)

Following the footsteps of Fielicke and co-workers,[21] we have explored the exceptional enhancement of Ng-M bonding strength in NgM$_3^+$ (Ng = Ar, Kr, Xe; M = Cu, Ag, Au) ions through hydrogen

doping by employing various *ab initio* based techniques.[22] The precursor ions, *viz.*, Au$_3^+$, Au$_3$H$^+$, and AuH$_2^+$ exhibit a nonlinear planar structure for the minima. Now the interaction of the Ng atom with these ions leads to the formation of strongly bonded NgAu$_3^+$, NgAu$_2$H$^+$, and NgAuH$_2^+$ complexes, as depicted in Fig. 3 which shows the variation of Ar-Au bond lengths in these complexes. The decrease in the Ar-Au bond length value from 2.605 Å in ArAu$_3^+$ to 2.518 Å in ArAu$_2$H$^+$ and 2.429 Å in ArAuH$_2^+$, respectively, as obtained by CCSD(T) indicates that the Ng-Au interaction is increased considerably in ArAuH$_2^+$ species. It implies that the Ng-Au bond strength is enhanced drastically with the doping of two hydrogen atoms in a pure Au trimer cation. In this context it is important to note that the CCSD(T) computed Ng-Au bond length values in NgAu$^+$ are generally larger (2.537, 2.553, and 2.617 Å in ArAu$^+$, KrAu$^+$, and XeAu$^+$, respectively) than that in the NgAuH$_2^+$ complexes, which indicate that the Ng-Au bond strength is greater in the latter complexes.
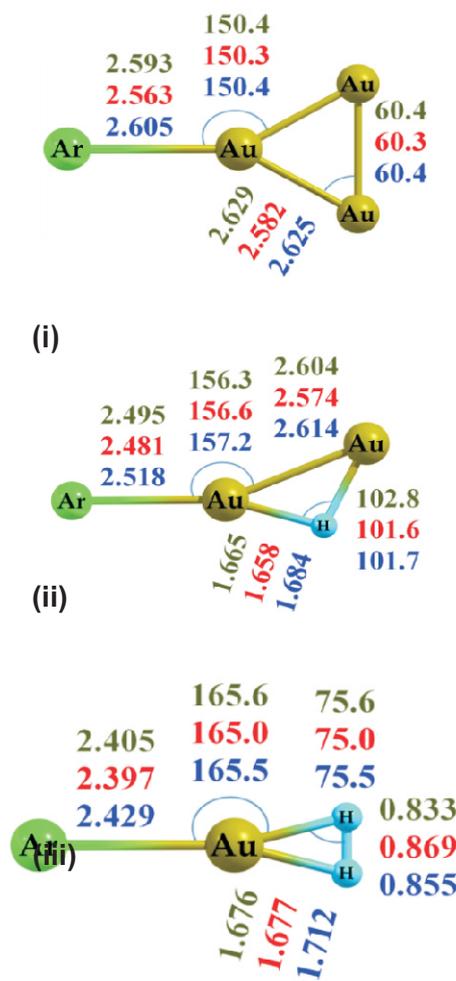
Fig.3: Optimized geometrical parameters of planer ArAu$_3^+$(i), ArAu$_2$H$^+$ (ii) and ArAuH$_2^+$ (iii) where the bond lengths are in Å and bond angles are in degrees. The values in green, red, and blue are computed at the ωB97X-D/DEF2, MP2/DEF2, and CCSD(T)/AVTZ levels of theory, respectively.

Table 1 lists all the bond dissociation energy, stretching frequency and force constant values for the Ng-Au bond in NgAu$_3^+$, NgAu$_2$H$^+$, and NgAuH$_2^+$complexes. As far as binding energy is concerned, the Ng-Au bonding interaction has been found to be increased by 2.26 times for Ar, 1.99 times for Kr, and 1.75 times for Xe complexes in going from NgAu$_3^+$ to NgAuH$_2^+$ complex as shown in the Table 1. The Ng-Au binding energy in NgAuH$_2^+$ ions are even more stronger than the corresponding energy in NgAuF and NgAu$^+$

Table 1. CCSD(T) Computed Bond Dissociation Energy (BE in kJ mol^{-1}) and MP2 Calculated Stretching Frequency (ν in cm^{-1}) and Force Constant (k in Nm^{-1}) Values for Ng-Au Bond in NgAu$_3^+$, NgAu$_2$H$^+$ and NgAuH$_2^+$ Species.

Ions	BE (Ng-Au)			ν (Ng-Au)			k (Ng-Au)		
	Ar	Kr	Xe	Ar	Kr	Xe	Ar	Kr	Xe
NgAu$_3^+$	31.9	50.7	81.2	120.5	116.7	114.1	39.4	60.3	81.0
NgAuH$_2^+$	47.5	69.3	102.4	142.2	126.3	116.4	63.4	81.1	95.6
NgAuH$_2^+$	72.0	100.7	142.0	223.2	183.0	166.2	97.8	115.2	125.3

which are found to be 46.0, 44.1 kJ mol^{-1} in Ar, 64.4, 73.5 kJ mol^{-1} in Kr, and 92.4, 121.6 kJ mol^{-1} in Xe containing complexes, respectively, at the same level. The MP2/DEF2 computed Ng-Au stretching vibrational frequency value changes from 120.5 to 223.2 cm^{-1} in Ar, 116.7 to 183.0 cm^{-1} in Kr, and 114.1 to 166.2 cm^{-1} in Xe containing complexes on going from NgAu$_3^+$ to NgAuH$_2^+$ species, respectively, and the corresponding force constant values are changed from 39.4 to 97.8 N m^{-1} in Ar, 60.3 to 115.2 N m^{-1} in Kr, and 81.0 to 125.3 N m^{-1} in Xe containing complexes (Table 1). Both the Ng-Au stretching frequency and force constant values strongly reveals that the Ng-Au bonding strength is greatly enhanced with the hydrogen doping in pure Au trimers which is found to be in concurrence with the optimized structures and energetics.

The unprecedented enhancement of noble gas-noble metal bonding strength in NgM$_3^+$ (Ng = Ar, Kr, and Xe; M = Cu, Ag, and Au) ions through hydrogen doping have been explored by using various *ab initio* based techniques. The concept of gold-hydrogen analogy has been used to evolve this pronounced effect of hydrogen doping in Au trimers leading to the strongest Ng-Au bond in NgAuH$_3^+$ species, as revealed from the calculated values of Ng-Au bond length, bond energy, vibrational frequency and force constant. Similar trends have been found in the case of Ng-Ag and Ng-Cu complexes. The enhancement of Ng-M bonding interaction in Ng-MH$_2^+$ (Ng = Ar, Kr, and Xe; M = Cu, Ag, and Au) as compared to that in Ng-M$_3^+$ can be attributed to considerable increase in the Ng-M covalency as revealed from the electron density based topological properties and energy decomposition analysis. Calculated values of HOMO and LUMO energies, and partial atomic charges further indicate that an enhancement in the charge-induced dipole interaction is also responsible for the surprisingly high Ng-M bonding interaction in Ng-MH$_2^+$ species.
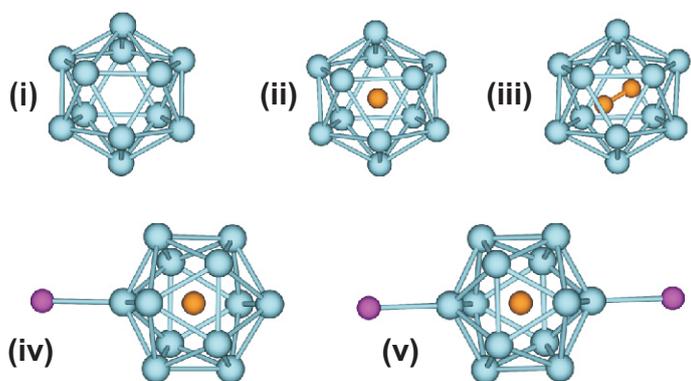
Fig.4: Optimized geometry of the (i) bare Pb$_{12}^{2-}$, (ii) Ng@Pb$_{12}^{2-}$, (iii) Ng$_2$@Pb$_{12}^{2-}$, (iv) Ng@KPb$_{12}^-$, and (v) Ng@K$_2$Pb$_{12}$.

Endohedral Encapsulation of Ng in Molecular Cages

In recent times, we have explored the possibility of the existence of noble gas encapsulated inorganic fullerene clusters by evaluating the stability of the Ng encapsulated endohedral Zintl ions, Ng@M$_{12}^{2-}$ (Ng = He, Ne, Ar, and Kr; M = Sn and Pb)[34] through density functional theory. Figure 4 depicts that the Ng@M$_{12}^{2-}$ cluster exhibits Ih symmetry while the D5d symmetry has been assigned to Ng$_2$@M$_{12}^{2-}$.

The cage diameter for Sn$_{12}^{2-}$ has been expanded from 6.061 Å to 6.111-6.555 Å while it is expanded from 6.303 Å to 6.344-6.764 Å in the Pb$_{12}^{2-}$ cage after the encapsulation of the Ng atoms. The
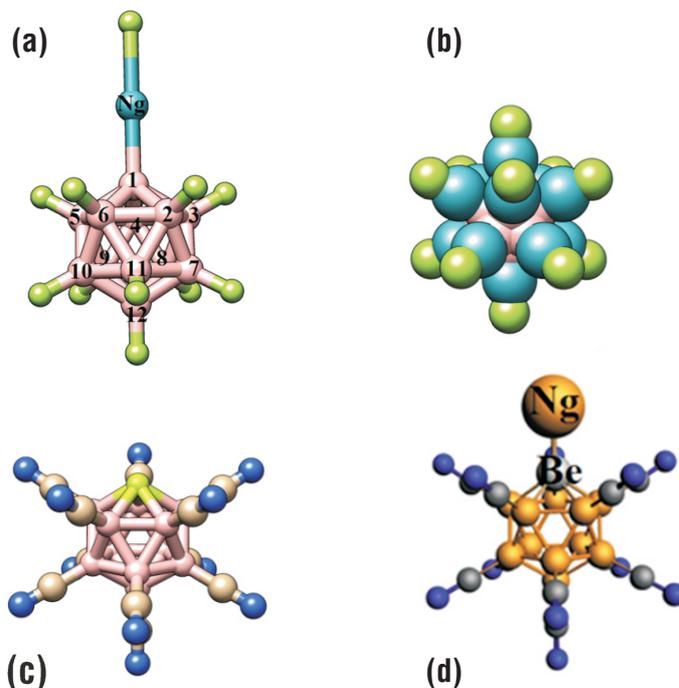
Fig.5: Optimized structures of (a) B$_{12}$NgF$_{12}^{2-}$, (b) B12Ng12F$_{12}^{2-}$, (c) BeB$_{11}$(CN)$_{11}^{2-}$, and (d) NgBeB$_{11}$(CN)$_{11}^{2-}$

B3LYP/def-TZVP computed Pb-Pb and Ng-Pb distances have been found to be in the range of 3.335-3.556 Å and 3.172-3.382 Å, respectively. A remarkable observation is that the He-He bond length (1.561 Å) in the He$_2$@Pb$_{12}^{2-}$ cluster is considerably shorter than that in the free He-He dimer (3.852 Å). The B3LYP/def-TZVP calculated binding energy are -15.2 to -147.2 kcal mol^{-1} in Ng@Pb$_{12}^{2-}$ clusters (Ng = He - Kr), while the same have been found to be 116.6 to 24.5 kcal mol^{-1} in Ng@KPb$_{12}^{2-}$ clusters and 199.4 to 105.9 kcal mol^{-1} in Ng@K$_2$Pb$_{12}$ clusters (Ng = He - Ar). These binding energy values clearly indicate that the Ng@Pb$_{12}^{2-}$ are thermodynamically unstable clusters while potassium salt of these are found to be stable. The kinetic stability of the Ng@Pb$_{12}^{2-}$ clusters has been studied through ab initio molecular dynamics simulation. Therefore, the Ng@M$_{12}^{2-}$ clusters are kinetically stable and thermodynamically unstable whereas the K$^+$ salt of Ng@M$_{12}^{2-}$ clusters are found to be both kinetically as well as thermodynamically stable.

Very recently, for the first time we have predicted a thermodynamically stable dianionic noble gas compound, viz., [NgBeB$_{11}$(CN)$_{11}$]$^{2-}$ (Ng = Ar, Kr, Xe).[37] Since the electron affinity of noble gas atoms is negative, therefore, a Ng atom can bind with the anions or dianions which are supposed to be superelectrophilic in nature due to the presence of a high positive charge on the free B or Be atom in these anions.[37]

Subsequently, we have further reported the unprecedented stabilization of multiply charged anion, $B_{12}F_{12}^{2-}$, through insertion of Ng atoms into B–F bonds, resulting in the formation of stable icosahedral $B_{12}Ng_{12}F_{12}^{2-}$ anions[38] (Fig.5) where the HOMO is stabilized significantly and the binding energy of the second excess electron is increased remarkably. Unprecedented stability enhancement with Ng insertion might be due to a strong covalent B–Ng bond, increased charge delocalization and increased electrostatic interaction between the oppositely charged centers.

In a nutshell, various high level quantum computational techniques provide all possible future directions to explore the different aspects of selective complexation and cluster formation using a specific noble gas atom with several interesting molecular systems utilizing various fundamental chemical concepts. Herein, the progress in the investigation of a novel class of chemically bound Ng compounds is reviewed. Reported work in the literature indicates that the field of noble gas chemistry is at an early developmental stage with a large number of open questions on the astonishing properties and the synthetic mechanisms of the Ng molecular systems, which put forward a real challenge to the contemporary researchers. Moreover, investigations of noble gas compounds would be highly promising not just from the view point of fundamental chemical bonding but also for the design of new materials to trap radioactive noble gases in nuclear establishments.

Corresponding Author*

Tapan K. Ghanty (tapang@barc.gov.in)

References

[1]   W. Kossel, *Ann. Phys.* (Leipzig), 1916, **49**, 229.

[2]   G. N. Lewis, *J. Am. Chem. Soc.*, 1916, **38**, 762.

[3]   M. Ozima and F.A. Podosek, *Noble Gas Geochemistry*, Cambridge University Press, UK, 2002.

[4]   Bobrow Test Preparation Services, *Cliffs A P Chemistry*, 2007, 15.

[5]   N. Bartlett, *Proc. Chem. Soc.*, 1962, **112**, 218.

[6]   L. Khriachtchev, M. Pettersson, N. Runeberg, J. Lundell and M. Rasanen, *Nature* (London), 2000, **406**, 874.

[7]   L. Khriachtchev, M. Rasanen and R. B. Gerber, *Acc. Chem. Res.*, 2009, **42**, 183.

[8]   L. Khriachtchev, K. Isokoski, A. Cohen, M. Rasanen and R. B. Gerber, *J. Am. Chem. Soc.*, 2008, **130**, 6114.

[9]   T. Jayasekharan and T.K. Ghanty, *J. Chem. Phys.*, 2006, **124**, 164309.

[10]   A. Ghosh, D. Manna and T.K. Ghanty, *J. Chem. Phys.*, 2013, **138**, 194308.

[11]   T. Jayasekharan and T.K. Ghanty, *J. Chem. Phys.*, 2008, **129**, 184302.

[12]   T. Jayasekharan and T.K. Ghanty, *J. Chem. Phys.*, 2012, **136**, 164312.

[13]   M. J. Barlow, B.M. Swinyard, P.J. Owen, J. Cernicharo, H. L. Gomez, R.J. Ivison, O. Krause, T.L. Lim, M. Matsuura, S. Miller, G. Olofsson and E.T. Polehampton, *Science*, 2013, **342**, 1343.

[14]   L. Khriachtchev, S. Tapio, A.V. Domanskaya, M. Rasanen, K. Isokoski and J. Lundell, *J. Chem. Phys.*, 2011, **134**, 124307.

[15]   D. Schroder, H. Schwarz, J. Hrusák and P. Pyykko, *Inorg. Chem.*, 1998, **37**, 624.

[16]   P. Pyykko, *J. Am. Chem. Soc.*, 1995, **117**, 2067.

[17]   S. Seidel and K. Seppelt, *Science*, 2000, **290**, 117.

[18]   J. M. Michaud and M. C. L. Gerry, *J. Am. Chem. Soc.*, 2006, **128**, 7613 and references therein.

[19]   B. Kiran, X. Li, H. –I. Zhai, L. –F. Cui and L. –S. Wang, Angew. *Chem., Int. Ed.*, 2004, **43**, 2125.

[20]   (a) T. K. Ghanty, J. Chem. Phys., 2005, 123, 074323. (b) T. K. Ghanty, *J. Chem. Phys.*, 2006, **124**, 124304.

[21]   A. Shayeghi, R. L. Johnston, D. M. Rayner, R. Schafer and A. Fielicke, Angew. *Chem., Int. Ed.*, 2015, **54**, 10675.

[22]   A. Ghosh and T.K. Ghanty, *J. Phys. Chem. A*, 2016, **120**, 9998.

[23]   T. Vazhappilly and T.K. Ghanty, *Comput. Mater. Sci.*, 2021, **189**, 110264.

[24]   D. Banerjee, C.M. Simon, A.M. Plonka, R.K. Motkuri, J. Liu, X. Chen, B. Smit, J.B. Parise, M. Haranczyk and P.K. Thallapally, *Nat. Commun.*, 2016, **7**, 11831.

[25]   T. Vazhappilly, T.K. Ghanty and B.N. Jagatap, *J. Phys. Chem. C*, 2016, **120**, 10968.

[26]   (a) T. Vazhappilly, T.K. Ghanty and B.N. Jagatap, *J. Nucl. Mater.*, 2017, **490**, 174; (b) T. Vazhappilly and T. K. Ghanty, *Mater. Today Commun.*, 2020, **22**, 100738.

[27]   (a) K. Srinivasu, S. Natarajan and T.K. Ghanty, *J. Phys. Chem. C*, 2019, **123**, 27531; (b) R. Gangwar, D. Pandey, K. Srinivasu, D. Raychaudhuri, A. Chakrabarti, A. Banerjee and T. K. Ghanty, *J. Phys. Chem. C*, 2021, **125**, 1493.

[28]   J. Li, B. E. Bursten, B. Liang and L. Andrews, *Science*, 2002, **295**, 2242.

[29]   B. Liang, L. Andrews, J. Li and B.E. Bursten, *J. Am. Chem. Soc.*, 2002, **124**, 9016.

[30]   J. Li, B. E. Bursten, L. Andrews and C. Marsden, *J. Am. Chem. Soc.*, 2004, **126**, 3424.

[31]   I. Infante, L. Andrews, X. Wang and L. Gagliardi, *Chem. Eur. J.*, 2010, **16**, 12804.

[32]   M. Khatua, S. Pan and P.K. Chattaraj, *J. Chem. Phys.*, 2014, **140**, 164306.

[33]   D. Chakraborty and P.K. Chattaraj, *Chem. Phys. Lett.*, 2015, **621**, 29.

[34]   P. Sekhar, A. Ghosh, M. Joshi and T.K. Ghanty, *J. Phys. Chem. C*, 2017, **121**, 11932.

[35]   M. Rohdenburg, M. Mayer, M. Grellmann, C. Jenne, T. Borrmann, F. Kleemiss, V.A. Azov, K.R. Asmis, S. Grabowsky and J. Warneke, Angew. *Chem., Int. Ed.*, 2017,

56, 7980.

[36] M. Mayer, V. van Lessen, M. Rohdenburg, G. -L. Hou, Z. Yang, R.M. Exner, E. Aprà, V. A. Azov, S. Grabowsky, S. S. Xantheas, *et al.*, *Proc. Natl. Acad. Sci.* U. S. A., 2019, **116**, 8167.

[37] M. Joshi and T.K. Ghanty, *Chem. Commun.*, 2019, **55**, 14379.

[38] M. Joshi and T.K. Ghanty, *Phys. Chem.*, 2020, **22**, 13368.

[39] A. Ghosh, D. Manna and T.K. Ghanty, *J. Phys. Chem. A*, 2015, **119**, 2233.

[40] A. Sirohiwal, D. Manna, A. Ghosh, T. Jayasekharan and T.K. Ghanty, *J. Phys. Chem. A*, 2013, **117**, 10772.

[41] P. Sekhar, A. Ghosh and T.K. Ghanty, *J. Phys. Chem. A*, 2015, **119**, 11601.

[42] A. Ghosh, A. Mallick and T.K. Ghanty, *Phys. Chem.*, 2020, **22**, 14109.

[43] A. Ghosh, S. Dey, D. Manna and T.K. Ghanty, *J. Phys. Chem. A*, 2015, **119**, 5732.

[44] P. Chopra, A. Ghosh, B. Roy and T. K. Ghanty, *Chem. Phys.*, 2017, **494**, 20.

[45] D. Manna, A. Ghosh and T. K. Ghanty, *J. Phys. Chem. A*, 2013, **117**, 14282.

[46] (a) T. Jayasekharan and T.K. Ghanty, *J. Chem. Phys.*, 2007, **127**, 114314; (b) T. Jayasekharan and T. K. Ghanty, *J.*

Chem. Phys., 2008, **128**, 144314.

[47] T. Jayasekharan and T.K. Ghanty, *J. Chem. Phys.*, 2006, **125**, 234106.

[48] J. Lundell, J. Panek and Z. Latajka, Chem. *Phys. Lett.*, 2001, **348**, 147.

[49] T.D. Fridgena and J.M. Parnis, *J. Chem. Phys.*, 1998, **109**, 2155.

[50] J. Lundell, M. Pettersson and M. Räsänen, *Phys. Chem.*, 1999, **1**, 4151.

[51] L. Khriachtchev, M. Pettersson, J. Lundell, H. Tanskanen, T. Kiviniemi, N. Runeberg and M. Räsänen, *J. Am. Chem. Soc.*, 2003, **125**, 1454.

[52] L. Khriachtchev, H. Tanskanen, J. Lundell, M. Pettersson, H. Kiljunen and M. Räsänen, *J. Am. Chem. Soc.*, 2003, **125**, 4696.

[53] L. Operti, R. Rabezzana, F. Turco, S. Borocci, M. Giordani and F. Grandinetti, *Chem. –Eur. J.*, 2011, **17**, 10682.

[54] D. Manna, A. Ghosh and T.K. Ghanty, *Chem. –Eur.. J*, 2015, **21**, 8290.

[55] A. Ghosh, D. Manna and T.K. Ghanty, *Phys. Chem.*, 2016, **18**, 12289.

[56] A. Ghosh, A. Gupta, R. Gupta and T. K. Ghanty, *Phys. Chem.*, 2018, **20**, 20270.

The Separation and Complexation Behavior of Trivalent Actinides and Lanthanides

*Arunasis Bhattacharyya, P.K. Mohapatra

Radiochemistry Division
Bhabha Atomic Research Centre, Mumbai-400 085, India

ABSTRACT

'f' block metal ions show very rich coordination chemistry with large coordination number. The actinides, moreover, show a range of oxidation states resulting in complex behavior in the solution phase. Radiotoxic nature of most of the actinides makes their experimental studies much more challenging and therefore computational chemistry can be a great help for more directed experimental trials. In this present article attempt will be made to cover our contribution to the computational studies of 'f' element complexes in relevance to the mutual separation of trivalent actinides and lanthanides.

Keywords: Actinide, Lanthanide, DFT, Extraction, Separation.

Introduction

Strong electron electron correlation, relativistic effects and spin orbit coupling in the 'f' element complexes, especially for the actinides, throw challenges to the computational chemists who want to deal with the complexes of these metal ions. With enormous development in the computational capability, significant amount of effort is being directed in understanding the complexation of actinides and lanthanides using computational studies. Their chemistry is mainly governed by their oxidation states. Lanthanides show simple chemistry due to their most stable 3+ oxidation state in general. Chemistry of the actinides is, however, much more complex due to the presence of variable oxidation states, especially for the early actinides upto plutonium due to the participation of their '*5f* ' electrons in bonding.[1] Bonding of the actinides at higher oxidation states (penta and hexavalent) involving the 'f' orbitals are therefore quite unique in case of early actinides.[2] Heavier actinides, however, show 3+ as the most stable oxidation state similar to the lanthanides due to stabilization of the '*5f* ' orbitals similar to the '*4f* ' orbitals of the lanthanides. This similar chemistry of the heavier actinides and the lanthanides leads to difficulty in their separation which is quite relevant for the safe management of nuclear waste.[3] In this article, attempt is made to compile our research on the bonding and complexation of trivalent actinides and lanthanides in relevance to their mutual separation.

Computational Methodology

Geometries of all the complexes shown in this article were optimized using def-SV(P) basis sets. In the cases of americium and lanthanides, 60 and 28 electron effective core potential (ECP) along with the corresponding def-SV(P) basis sets for the valence electrons are used. All the geometry optimizations were carried out employing the GGA functional BP86 which is composed of the Becke 1988 exchange functional along with the Perdew 86 correlation functional. The single point energies and electronic structures of the ligands and their complexes were calculated using the hybrid functional B3LYP and the def-TZVP basis set.

Bonding in trivalent actinide and lanthanide complexes

Ligands for Co-extraction of actinides and lanthanides

As we progress along the actinide series, the higher valent oxidation states become less stable and after plutonium, the trivalent is the most stable oxidation state similar to the lanthanide ions. Significant effort of computational chemistry is directed to understand the comparative bonding and complexation of trivalent actinides and lanthanides in relevance to their mutual separation.[4] Since long back, phosphine oxide and diamide based ligands are proposed for the co-extraction of trivalent actinides.[5] Diglycolamide based extractants are reported to be most promising till date for the coextraction of trivalent actinides and lanthanides.[6] There are some literature on the complexation of trivalent actinides and lanthanides with diglycolamide (DGA) based ligands.

Wang *et al.* found that the tetra-octyl diglycolamide (TODGA) is selective for Am^{3+} over Eu^{3+},[7] the experimental observation, however, shows opposite trends. With proper choice of model and incorporation of dispersion correction using DFT-D3 technique, the experimental trends of the extraction of trivalent actinides and lanthanides could nicely be explained.[8]

We also carried out the complexation of Ln^{3+} ions with DGA derivatives with systematically varying the alkyl chain length and branching and the experimentally observed complexation bahaviour of the DGA derivatives was explained successfully employing DFT calculations.[9] Optimized structures of Nd^{3+} complex of TMDGA and the frontier molecular orbitals of the complex are shown in Fig.1 where significant contribution of the metal based '*f* ' orbitals is noticed.
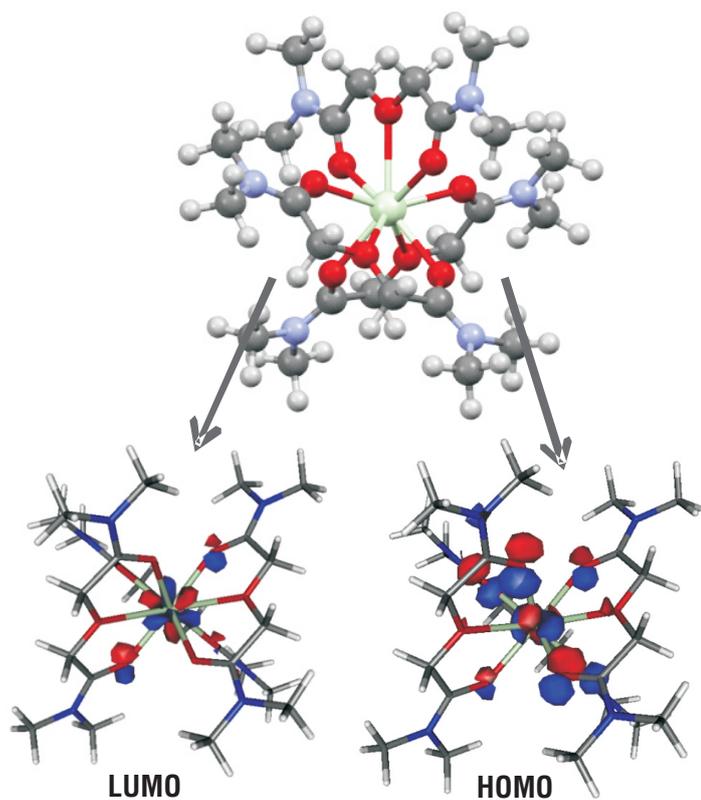
Fig.1: Optimized structure of Nd³⁺ complex of TMDGA and Frontier molecular orbitals of the complex (Nd: Light Green; O: Red; N: Light Purple; C: Grey; H: Light Grey).

Complexes with ligands for separation of actinides and lanthanides

Similar chemistry of the trivalent actinides and lanthanides leads to their separation an extremely challenging task to the chemists and only some soft donor ligands show selectivity towards the trivalent actinides over the lanthanides. A sulphur donor ligand, dithiophosphinic acid (Cyanex 301, Fig. 2) showed very high selectivity towards Am³⁺ over Eu³⁺.[10] It was, therefore, be of interest to understand the difference in bonding in its Am³⁺ and Eu³⁺ complexes. Cao. *et al.* found that the presence of solvent is the major factor contributing to the selectivity of Cyanex-301.[11] We, however, observed experimentally the formation of different extractable species for Am³⁺ and various lanthanides (viz. La³⁺, Eu³⁺ and Lu³⁺) which could be explained on the basis of their relative stabilities of their complexes as compared to their corresponding trinitrato species calculated using DFT based technique. Further, the metal-ligand complexation energy was segregated into electrostatic, Pauli repulsion, and orbital interaction components. Higher covalence in the M-S bond in the dithiophosphinate complexes as compared to the M-O bond in the nitrate complexes was reflected in the higher orbital and lower electrostatic interactions for the complexes with increasing number of dithiophosphinate ligands. Higher affinity of the dithiophosphinate ligands for Am³⁺ over Eu³⁺ was corroborated with higher covalence in

the Am-S bond as compared to the Eu-S bond, which was reflected in shorter bond length in the case of the former and higher ligand to metal charge transfer in Am³⁺-dithiophosphinate complexes. The results were found to be consistent in gas phase density functional theory (DFT) calculations using different GGA functional.[12] Thus, computational studies were able to explain the experimentally observed trends of the dithiophosphinate complexation of the trivalent actinides and lanthanides.

Nitrilo-triacetamide (NTA) derivatives are mixed 'N,O' donor ligands reported to be selective for the trivalent actinides over the lanthanides from the liquid-liquid extraction studies.[13] We, therefore, investigated the complexation behavior of the NTA derivatives with the help of spectroscopic studies and DFT based calculations.[14] Two phase liquid-liquid extraction studies indicated that both the Am³⁺ and Eu³⁺ ions are extracted as the 1:2 complex and in this complex, the only possibility considered was ML_2^{3+} as the two NTA ligands can occupy eight coordination sites of the metal ions and the approach of other ligands is expected to be difficult due to the bulkiness of the two NTA ligands. Moreover, solution phase extended X-ray absorption fine structure spectroscopy (EXAFS) and time resolved fluorescence spectroscopy (TRFS) studies of the Eu³⁺ complex indicated that the central Eu³⁺ ion is eight-coordinated and devoid of any water molecules in the inner coordination sphere. DFT calculations were, therefore, carried out on the ML_2^{3+} type of complexes of both Am³⁺ and Eu³⁺. Selectivity of NTA derivative, as observed from the solvent extraction studies, is nicely reflected in the shorter 'Am–N' bond lengths (2.848 and 2.853 Å) as compared to the 'Eu–N' bond lengths (2.886 and 2.892 Å) in their respective complexes (Fig. 3). This is further supported by the higher Wiberg and Mayer's bond orders of the 'Am–N' bonds as compared to that of the 'Eu–N' bonds. A systematic study was, therefore, carried out on the metal-ligand bond lengths varying ionic sizes of the Ln³⁺ ions along with Am³⁺ and the results are presented in Fig. 4. Ionic radii of the Am³⁺ and Ln³⁺ ions, except Pm³⁺, were taken from the literature for the eight-coordinated metal ions.[15] Nice correlation of 'M–O' bond lengths with the ionic size of Ln³⁺ ions was observed, which
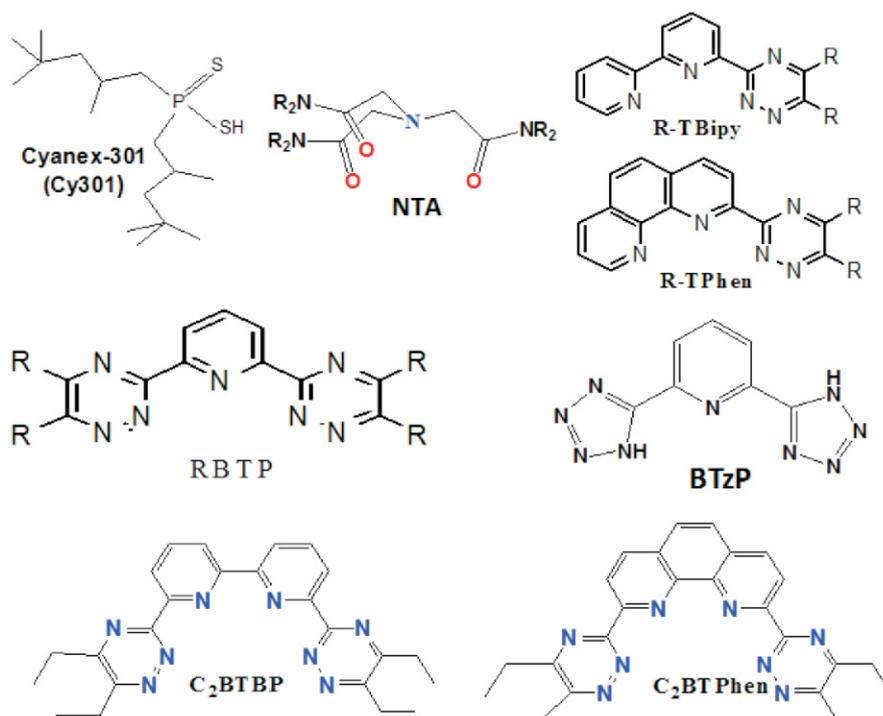
Fig.2: Different soft donor ligands considered for the comparative complexation of trivalent actinides and lanthanides.
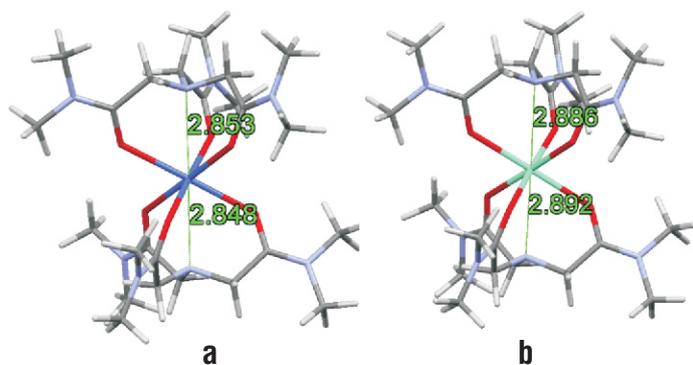
Fig.3: Optimized structures of Am^{3+} and Eu^{3+} with NTA (Am: Purple; Eu: Light Green; O: Red; N: Light Purple; C: Grey; H: Light Grey).
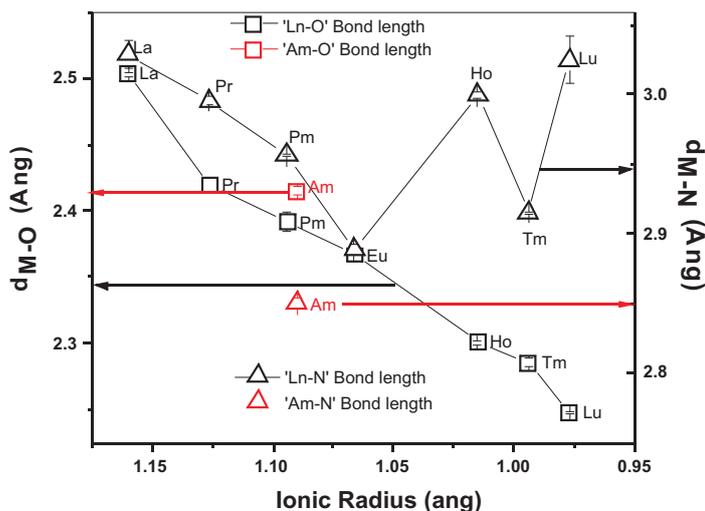
Fig.4: Variation of 'M-O' and 'M-N' bond length along the lanthanide series (Ln^{3+}) and their comparison with Am^{3+}.
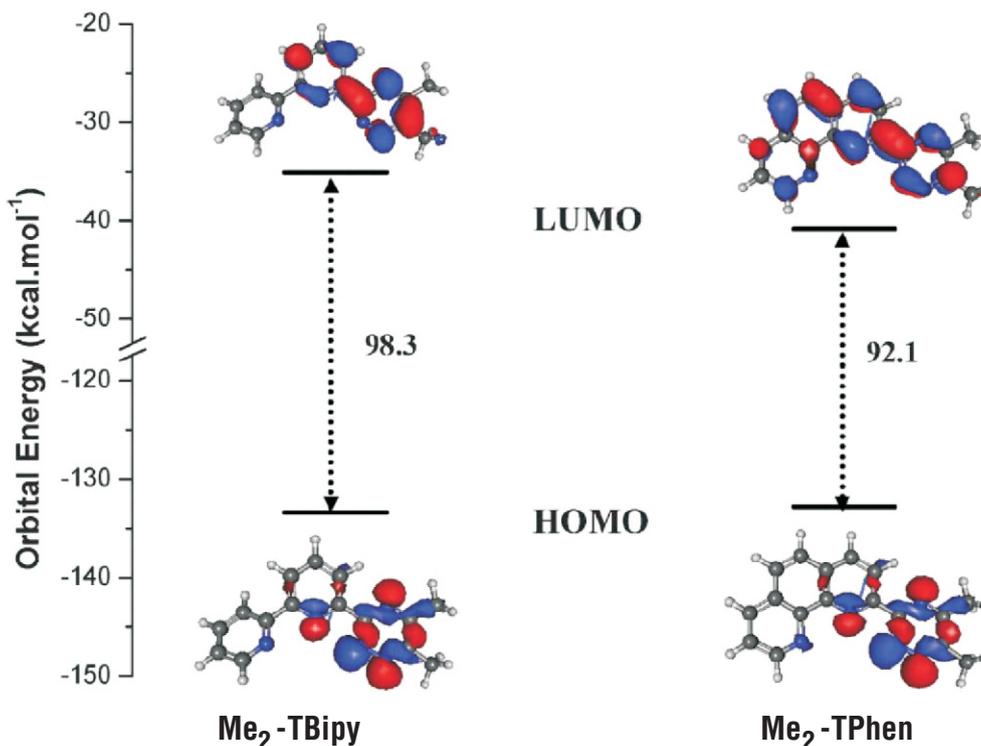
suggests that the 'M–O' bonds are predominantly governed by purely ionic interactions in all the Ln^{3+} complexes. The 'Am–O' bond distance is somewhat higher than that expected from the observed trends of the Ln^{3+} complexes. However, when the 'M–N' bonds were considered, no such correlation was noticed and unlike the 'Am-O' bonds, 'Am–N' bond length was found to be significantly shorter than any of the 'Ln–N' bonds in the series, which is a clear indication of a higher degree of covalence in the 'Am–N' bond which made this ligand selective for Am^{3+} over the Ln^{3+} ions. DFT study, therefore, nicely corroborates with the experimental results. Besides the 'S' donor and mixed 'N,O' donor ligands, 'N'-donor heteropolycyclic ligands found to be promising for the separation of trivalent actinides and lanthanides.

Triazinyl bipyridine (TBipy) derivatives, a class of 'N' donor hetero polycyclic ligand, was reported to show some degree of selectivity for the trivalent actinides.[16] We designed a new ligand, Triazinyl phenanthroline (TPhen) derivative (Fig. 2), having more structural rigidity and evaluated for the separation of trivalent actinides and lanthanides. Improved extraction and separation of Am^{3+} over Eu^{3+} was experimentally observed using TPhen derivative as compared to TBipy derivative. Higher extraction of Am^{3+} with Me$_2$-TPhen was explained on the basis of its lower conformational energy requirement for complexation as compared to Me$_2$-TBipy. The higher selectivity of Me$_2$-TPhen for Am^{3+} over Eu^{3+} as compared to Me$_2$-TBipy, on the other hand, was attributed to the higher softness of Me$_2$-TPhen as compared to Me$_2$-TBipy as a result of the lower HOMO-LUMO gap (Fig. 5). Crystals of La^{3+}-Me$_2$-TPhen complex was prepared and its structure as determined from the single crystal XRD technique is shown in Fig. 6.[17-18]

Bis(1,2,4-triazinyl) pyridine (BTP) derivatives, where two triazinyl rings are present along with the central pyridine ring (Fig. 2), are found to be very promising for the separation of trivalent actinides and lanthanides.[19] We reported remarkable enhancement of selectivity of the methyl derivative of BTP (MeBTP) in room

Fig.5: A Walsh diagram showing the HOMO and LUMO and their energies (kcal.mol^{-1}) for Me$_2$(TBipy) and Me$_2$(TPhen).
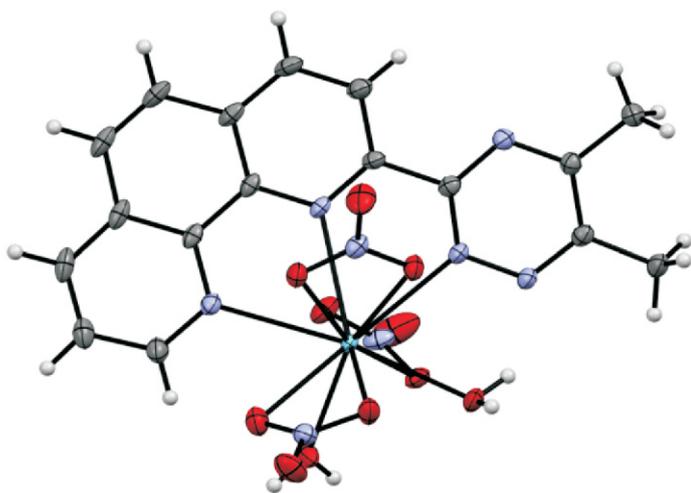
Fig.6: Crystal structure of La³⁺ complex of Me₂-TPhen (La: Light Green; O: Red; N: Light Purple; C: Grey; H: Light Grey).

temperature ionic liquid medium as compared to that in the molecular solvent which was attributed to the formation of different complexes of Am^{3+} and Eu^{3+} in RTIL medium as shown in Fig. 7. Computational studies showed higher overlap between metal and ligand based orbitals for Am^{3+} complex extracted in the RTIL medium as compared to that in the molecular solvent (Figs. 7d and 7e) resulting in increased selectivity of MeBTP for Am^{3+} in RTIL medium.[20]

We observed that with increasing number of 'N' atoms in the lateral rings selectivity for trivalent actinides over lanthanides improved significantly. We, therefore, designed a new ligand, bis-tetrazolyl pyridine (BTzP, Fig. 2), having four 'N' atoms in the lateral tetrazole rings. Two phase liquid-liquid extraction studies using BTzP showed a separation factor value >50. Complexation behavior of BTzP was studied using both experimental and computational studies. Absorption spectroscopic studies of the Am^{3+} complex indicated the presence of two chemically non equivalent Am^{3+} ions
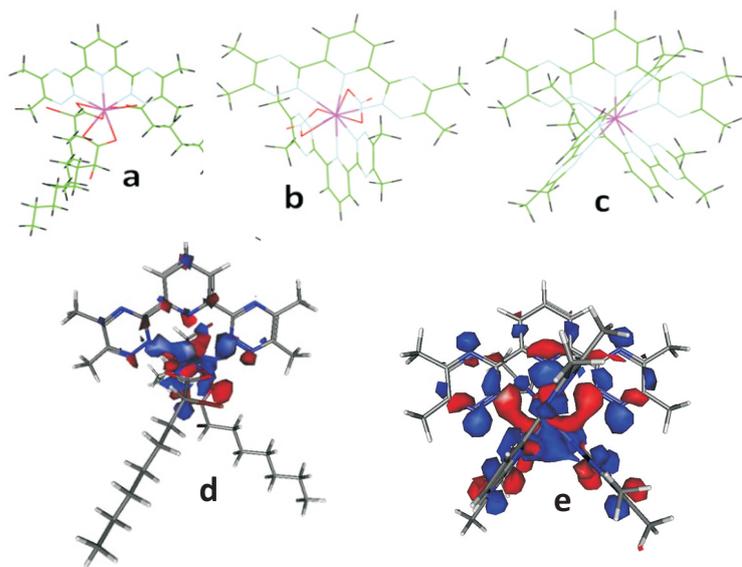
Fig.7: Optimized structures of (a) Am^{3+} and Eu^{3+} complexes of MeBTP observed in molecular diluents in presence of 2-Br-decanoic acid; (b) Eu^{3+} and (c) Am^{3+} complex of MeBTP in C4mim.NTf2 (Am/Eu: Magenta; O: Red; N; Light Blue; C: Green; H: Black); (d) HOMO of the Am^{3+} complex 'a' and (e) HOMO of the Am^{3+} complex 'c'.

in the complex, which was also supported from the time resolved fluorescence study of the Eu^{3+} complex of BTzP with two different Eu^{3+} ions having lifetime values of 479 and 1841 µs. In order to further understand this interesting complexation behavior, solid Nd^{3+} complex of BTzP was prepared and single crystal XRD study indicated formation of ion pair type of complex (Fig. 8a), where in the cationic part, Nd^{3+} ion is surrounded by one binegative BTzP and six water molecules and in the anionic part the Nd^{3+} ion is surrounded by two binegative BTzP units. DFT calculations revealed that in the cationic part, the distances between the metal ion and the coordinating 'N' atoms of the lateral tetrazole rings (M- Nt) are shorter in the case of Am^{3+} complex as compared to that in the Nd^{3+} complex in spite of comparable ionic radii of Am^{3+} and Nd^{3+} for a fixed coordination number. This indicates stronger metal- nitrogen interaction in the cationic part of the Am^{3+} complex, and this is also supported by higher Mayer's bond order in the Am- N_t bonds as compared to the Nd- N_t or Eu- N_t bonds. Similar observation was also noticed in case of the bond between the metal ion and the coordinating 'N' atom of the central pyridine ring (M- Np) in the cationic part. In the anionic part, however, no such increase in the M- N bond strength in the Am^{3+} complex was noticed. The metal- nitrogen bond orders were found to be higher anonymously in the cationic part as compared to that in the anionic part. This could be due to the sharing of the metal-based orbitals with two doubly negative BTzP molecules in the anionic part, whereas in the cationic part the metal orbitals are shared with only one BTzP molecule other than the neutral water molecules. Frontier molecular orbitals (FMOs) were analysed to understand the bonding between the metal ion and the coordinating 'N' atoms of the BTzP units in their complexes. Orbitals that have contributions from both the metal and the ligand (BTzP) have influence in the metal- ligand bonding. The lowest unoccupied molecular orbitals (LUMO) of the complexes of both the metal ions (Am^{3+} and Eu^{3+}) have contributions from the metal ion and the ligand molecules (BTzP) in the cationic as well as anionic parts. In the LUMO of both the cationic and anionic parts of the BTzP complexes of Am^{3+} and Eu^{3+}, σ-bonding interaction is noticed between the metal f-orbitals and sp^2 hybridized orbitals of the tetrazolyl N atoms. This σ-bonding interaction is stronger in the Am^{3+} complex as compared to that in the Eu^{3+} complex as observed from the higher overlap between the metal and ligand orbitals in case of the former (Figs. 8a and 8b). The occupied molecular orbitals (MOs) are mainly dominated by the ligand based orbitals in the cationic part. In the Am^{3+} complex, π-interaction between the f-orbitals of Am^{3+} and p-orbitals of the tetrazolyl N atoms was noticed (singly occupied molecular orbital (SOMO-13), which further strengthened the metal- ligand interactions in the Am^{3+}-BTzP complex. In the cationic part of the Eu^{3+} complex, however, the occupied MOs that have the metal f-orbitals deeply burried (SOMO-30) do not show any bonding interactions between the metal and the ligand.[21]

Till now we discussed the bonding and complexation behavior of tridentate 'N' donor ligands. There are few tetradentate 'N' donor ligands which showed promising selectivity for the trivalent actinides over the lanthanides. Bis-triazinyl bipyridine (BTBP) and phenanthroline (BTPhen) derivatives are the most prominent in this class of ligands. We investigated the complexation of Am^{3+} and different Ln^{3+} ions with BTBP derivatives. Stronger complexation with Am^{3+} ion was noticed from the experimental studies which was supported by the higher bond strength/order in Am–N bonds as compared to the Eu–N bonds in their BTBP complexes from the DFT based calculations. The energetics of the complexation process in the solution phase also supports the observation of favourable Am^{3+}
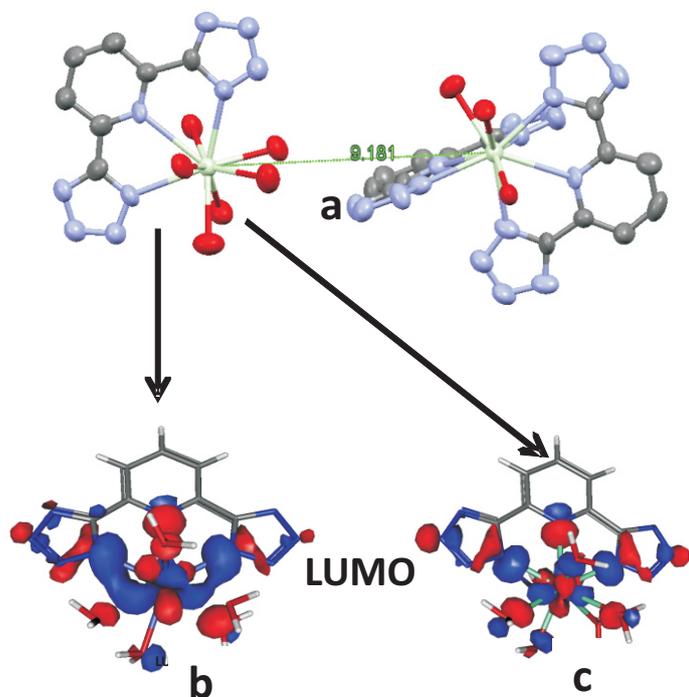
Fig.8: (a) Experimentally observed structure of Nd^{3+} complex of BTzP (Nd: Light Green; O: Red; N: Light Purple; C: Grey); Lowest unoccupied molecular orbital of the (b) Am^{3+} and © Eu^{3+} complexes of BTzP (cationic part).
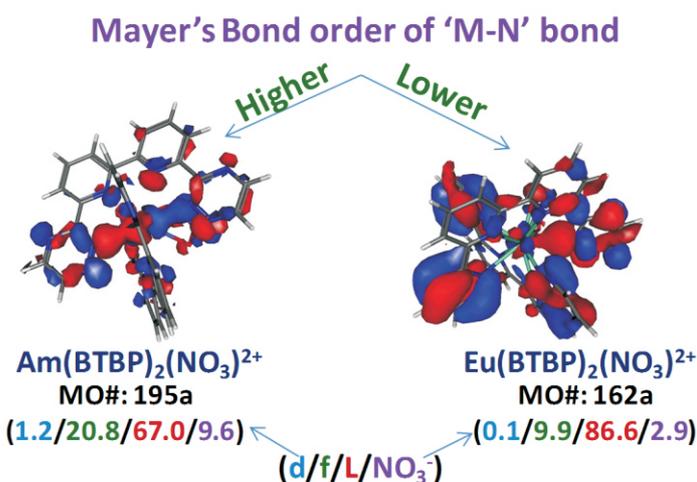
Fig.9: Frontier molecular orbitals (FMOs) of Am^{3+} complexes of BTBP and low lying molecular orbitals of Eu^{3+} complex of BTBP having significant metal ion 'f' orbital contribution and indicating the overlap between metal and ligand orbitals and percentage of Am^{3+} ('f 'or 'd ') / ligand / nitrate orbitals in those FMOs (Used cutoff: 0.013 e/Bohr^3).

complexation with the BTBP derivatives.[22] Contribution of metal based orbitals is observed by analyzing the frontier molecular orbitals of the Am^{3+} complex whereas that was observed for much deep seated molecular orbitals in case of Eu^{3+} complex. The contribution of both the metal 'd' and 'f' based orbitals are higher in the Am^{3+} complex as compared to that in the Eu^{3+} complex (Fig. 9) which resulted into higher bond order between the metal ion and the ligand molecule in the Am^{3+} complex leading to preference of this class of ligands towards the trivalent actinides over the lanthanides.[22]

Computational study in Am^{3+}/Cm^{3+} Separation

Separation of Am^{3+} and Cm^{3+} is even more challenging than the intergroup separation of trivalent actinides and lanthanides. We have systematically studied the separation of Am^{3+} and Cm^{3+} using hydrophilic BTP, BTBP and BTPhen derivatives using two phase liquid-liquid extraction techniques and the comparative extraction bahaviour of Am^{3+} *vis-à-vis* Cm^{3+} was explained with the help of DFT studies. In order to compare the complexation of Am^{3+} and Cm^{3+},the complexation energies (ΔE_{COMP})for the following equilibrium are calculated and listed in Table 1.

$$M (H_2O)_9{}^{3+} + L \rightleftharpoons ML (H_2O)_x + (9-x) H_2O \qquad (1)$$
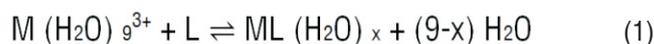
Where M is Am or Cm and L is BTP, BTBP or BTPhen derivatives. As expected the complexation is more favourable in case of the tetradenate ligand BTBP as compared to the tridenate BTP derivative. In case of BTPhen, the complexation is still more favourable as compared to BTBP due to preorganized structure of BTPhen. However, when the complexation of Am^{3+} and Cm^{3+} is compared, all the ligands show preference for Cm^{3+} over Am^{3+} due to the smaller ionic radius of Cm^{3+}. This suggests that the complexation of Am^{3+} and Cm^{3+} with these ligands is mainly governed by the electrostatic interactions.

Experimental trends of the Am^{3+} and Cm^{3+} extraction by TODGA in presence of the hydrophilic BTP, BTBP and BTPhen derivatives in the aqueous phase could be explained after consideration of the complexation of TODGA. For the computational simplicity the methyl derivative (TMDGA) was considered in place of the octyl derivative (TODGA). Considering the complexation energy (ΔE_{TMDGA}) for the following equilibrium, TODGA is selective towards Cm^{3+} over Am^{3+} by 32.0 kJ.mol^{-1} ($\Delta\Delta E_{TMDGA}$). Therefore, even if one considers the competion by TMDGA, BTP remains selective towards Cm^{3+} over Am^{3+} as reflected in the difference between the ($\Delta\Delta E_{Cm-Am}$) and ($\Delta\Delta E_{TMDGA}$) values and, therefore, Am^{3+} is selectively extracted in the organic phase by TODGA. In the case of BTPhen, on the other hand, Cm^{3+} is extracted selectively by TODGA as the selectivity of TMDGA for Cm^{3+} over Am^{3+} is observed to be higher

Table 1 Complexation energies (ΔE_{COMP}) of Am^{3+} / Cm^{3+} complexes (kJ.mol^{-1}).

Ligand	M^{3+}	ΔE_{comp}	$\Delta\Delta E_{Cm-Am}$	$\Delta\Delta E_{Cm-Am}$ - $\Delta\Delta E_{TMDGA}$
BTP	Am^{3+}	-187.4	-52.0	-20.0
	Cm^{3+}	-239.4		
BTBP	Am^{3+}	-256.2	-36.3	-4.3
	Cm^{3+}	-292.5		
BTPhen	Am^{3+}	-275.6	-24.7	7.3
	Cm^{3+}	-300.2		

than that of BTPhen ($\Delta\Delta E_{Cm-Am}$ = 24.7 kJ.mol^{-1}). BTBP, however, shows comparable selectivity as TMDGA from Cm^{3+} over Am^{3+} and therefore, no selectivity is noticed in the solvent extraction study employing the BTBP derivative.[23]

Conclusions

With the advent of advanced codes for the computational studies, understanding the chemistry of the 'f' block elements is improved remarkably. Experimental observations on the complexation of these elements in relevance to their mutual separation could be explained successfully with the help of DFT based calculations. However, more challenges in the computational chemistry still lies in the prior prediction of the complexation and extraction behavior of the ligands thereby reducing the number of experimental trials.

Corresponding Author*

Arunasis Bhattacharyya (arun12@barc.gov.in)

References

[1] G.R. Choppin and M.P. Jensen, *Actinides in Solution: Complexation and Kinetics in Chemistry of Actinides and Transactinide elements*, Eds. L.R. Morss, N.M. Edelstein, J. Fuger, J.J. Katz, 2008, Vol. **4**, 2524.

[2] M.L. Neidig, D.L. Clark, R.L. Martin, *Coord. Chem. Rev.*, 2013, **257**(2), 394.

[3] K.L. Nash, *Solv. Extr. Ion Exch.*,1993, **11**, 729.

[4] N. Kaltsoyannis, *Chem. Soc. Rev.*, 2003, **32**, 9.

[5] J.N. Mathur, M.S. Murali, K.L. Nash, *Solv. Extr. Ion Exch.*, 2001, **19**, 357.

[6] S.A. Ansari, P.N. Pathak, P.K. Mohapatra, V.K. Manchanda, *Chem. Rev.*, 2012, **112**, 1751.

[7] C.Z. Wang, J.H. Lan, Q.Y. Wu, Y.L. Zhao, X.K. Wang, Z.F. Chai, and W.Q. Shi, *Dalton Transactions*, 2014, **43**(23), 8713.

[8] Sk. M. Ali, S. Pahan, A. Bhattacharyya, P.K. Mohapatra, *Phys.Chem.Chem.Phys.*, 2016, **18**, 9816.

[9] Arijit Sengupta, Arunasis Bhattacharyya, Willem Verboom, Sk. Musharaf Ali, and Prasanta K. Mohapatra, *J. Phys. Chem. B*, 2017, **121**, 2640.

[10] Y. Zhu, J. Chen, R. Jiao, *Solvent Extr. Ion Exch.*, 1996, **14**, 6.

[11] X. Cao, D. Heidelberg, J. Ciupka, M. Dolg, *Inorg. Chem*. 2010, **49**, 10307.

[12] A. Bhattacharyya, T.K. Ghanty, P.K. Mohapatra, V.K. Manchanda, *Inorg. Chem.*, 2011, **50**, 3913.

[13] Y. Sasaki, Y. Tsubata, Y. Kitatsuji, Y. Sugo, N. Shirasu and Y. Morita, *Solv. Extr. Ion Exch.*, 2014, **32**, 179.

[14] A. Bhattacharyya, R.J.M. Egberink, P.K. Mohapatra, P.K. Verma, A.K. Yadav, S. Jha, D. Bhattacharyya, J. Huskens, W. Verboom, *Dalton Trans.*, 2017, **46**,16631.

[15] R.D. Shannon, Acta Crystallogr., *Sect. A: Cryst. Phys., Diffr., Theor. Gen. Crystallogr.*, 1976, **32**, 751.

[16] M.J. Hudson, M.G.B. Drew, M.R.S. Foreman, C. Hill, N. Huet, C. Madic and T.G.A. Youngs, *Dalton Trans.*, 2003, 1675

[17] A. Bhattacharyya, T. Gadly, P.K. Mohapatra, S.K. Ghosh, D. Manna, T.K. Ghanty, V.K. Manchanda, *RSC Advances,* 2012, **2**, 7066.

[18] A. Bhattacharyya, T. Gadly, P. Pathak, S.K. Ghosh, M. Mohapatra, T.K. Ghanty, P.K. Mohapatra. *Dalton Trans.*, 2014,**43**,12422.

[19] Z. Kolarik, U. Müllich, F.Gassner, *Solv. Extr. Ion. Exch.*, 1999, **17**, 23.

[20] A. Bhattacharyya, S.A. Ansari, T. Gadly, S.K. Ghosh, M. Mohapatra, P.K. Mohapatra, *Dalton Trans.*, 2015, **44**, 6193.

[21] A. Bhattacharyya, T. Gadly, A.S. Kanekar, S.K. Ghosh, M. Kumar, P.K. Mohapatra, *Inorg. Chem.*, 2018, **57**, 5096.

[22] A. Bhattacharyya, M. Mohapatra, P.K. Mohapatra, T. Gadly, S.K. Ghosh, D. Manna, T.K. Ghanty, N. Rawat, B.S. Tomar, *Eur. J. Inorg. Chem.*, 2017, **820.**

[23] A. Bhattacharyya, S.A. Ansari, K.N. Sundaramurthy, R. Cingaram, Venkatachalapathy B, S.R. Toleti, S. Hariharan and P.K. Mohapatra, *Dalton Trans.* 2021, Accepted Manuscript (doi.org/10.1039/D1DT00307K).

Tritium Barrier Materials from First Principles Density Functional Theory

Anil Boda[1,2] , ***Sk. Musharaf Ali**[1,2], **K.T. Shenoy**[1]

[1]Chemical Engineering Group, Bhabha Atomic Research Centre, Mumbai-400085, India
[2]Homi Bhabha National Institute, Mumbai-400094, India

ABSTRACT

The diffusion, permeation and solubility of hydrogen isotopes in metal is of great technological significance as it helps in controlling the hydrogen induced embrittlement and also in the selection of structural materials for reactors with minimum permeability of tritium. Atomistic understanding of the behavior of D/T with metal is highly desirable to design an efficient barrier material. DFT calculations were performed to investigate the interaction and dynamical behaviors of hydrogen isotopes in pure bcc Fe, Cr and W. The adsorption and dissociation pathways for hydrogen isotopes were predicted on (100) surface of Fe, Cr and W. The activation barrier energy for H atom to diffuse from one interstitial void to nearest interstitial void has been computed using nudge elastic band method. The calculated diffusion coefficients, permeability constants and solubility are found to be higher for H compared to its heavier isotopes D and T. Further, the permeability constants predicted to be lowest for W and thus considered as most suitable plasma facing materials.

Keywords: Fe, W, Cr, DFT, Hydrogen isotopes, diffusion, permeation.

Introduction

The heavier deuterium and tritium isotopes of hydrogen have been proposed as the fuels for the first generation of fusion reactors [4]. Tritium like protium easily permeates metallic substance, particularly, under high temperature and reacts vigorously with oxygen. Further, tritium will readily exchange with hydrogen . This is of particular apprehension since tritium poses a severe hazard to living creatures if it exchanges hydrogen in our biological systems due to its radioactive nature. Therefore, it is very imperative to confine tritium within suitable materials and conditions. Polymeric materials are not considered as a choice because of hydrogen-tritium exchange would considerably modify the properties of the polymers. Therefore, a rule of thumb is not to use polymeric substances and instead, attention must be given to either inorganic or metal substances. However, the challenge in the use of metallic containment is that tritium readily permeates them. Therefore, it is of prime necessary to understand the interaction between hydrogen isotopes and metals from atomistic level. In addition, the hydrogen absorption into the bulk of metals is not only important to phenomena such as metal embrittlement but also for hydrogen purification and hydrogen storage. Commonly, steel is used as containment materials [5,6]. But at high temperatures, hydrogen will diffuse into the steel and may combine with carbon to form cluster of methane at internal voids which at high pressure initiates cracks in the steel and leads to decarburization resulting in to loss of strength and ductility. Steels with 9-12 wt% Cr have received renewed interest in the last years in view of their potential application as structural materials in nuclear reactors and prospective fusion reactors having diffusion coefficients one order of magnitude lower than those of pure Fe metal [7]. The choice of materials for plasma facing components (PFC) in fusion based nuclear power reactor using deuterium-tritium fuel under the highly ambitious project of International Thermo nuclear Experimental Reactor (ITER) is one of the most fascinating and challenging ongoing research activities. The major scientific challenge to achieve the goal is to identify materials which can withstand the extreme heat and particle fluxes from the plasma under incessant neutron bombardment. Large scale computation and experiments are being carried out worldwide on various materials to find out their performance under stringent experimental conditions pertinent to ITER. Further, some metals (mainly steel varieties) are being used as structural material [5,6] or plasma coating substance [8-10] in fusion reactors. Due to its special mechanical and thermal properties, tungsten, W is used in a large number of industrial applications. In view of these properties, W is considered to be the most favored for the highest particle flux due to least erosion and therefore, is anticipated to be used as a diverter plate material in the fusion device of ITER. Additionally, the long time accumulation of high concentration of H can lead to alteration of the material's mechanical and physical properties. Therefore, the knowledge of diffusion behaviour of interstitial H atoms in bulk metals, especially Fe, Cr and W is of utmost necessary which has been studied by a number of authors using density functional theory (DFT) [11-33]. All the calculations infer that the tetrahedral sites in Fe, Cr and W is the most preferable for occupation by interstitial H atoms compared to octahedral sites (o-sites) which is in line with the reported experimental observations [34]. Several computational studies are performed for H diffusion behaviour in Fe and activation energy and pre-factor [11-16] were reported. From computational studies, the reported activation energy was found to be varied from 0.04- 0.09 eV and the values of pre-factor were varied from 10^{-7}– 10^{-8} m²/s. The calculated activation energies for the diffusion of H between two adjacent tetrahedral sites in W were seen to vary widely: 0.20 - 0.38 eV [20, 29-31, 35]. Among these results, activation energy reported by Johnson *et al*. [20] is seen to be agreed well with the experimentally obtained results of Frauenfelder [36, 37], which is the most consistent experimental result to date
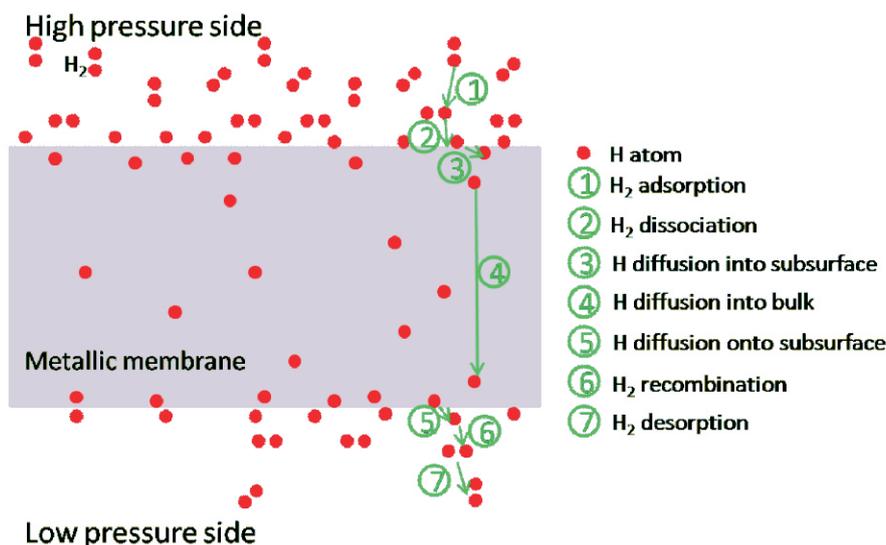
Fig.1: Schematic of Hydrogen isotope permeation through material.

[38]. Although, experimental data on diffusion, permeation and solubility of hydrogen isotopes through tungsten is available for a range of temperature [30, 36, 37, 39-50], no systematic theoretical efforts were put forward to evaluate the permeation and solubility of H isotopes through W. Also, there is a wide variation in the reported experimental data of H isotopes due to challenges associated with permeability measurements [48], particularly for radioactive tritium. Further, the presence of vacancies also play a pivotal role in diffusion behaviour [1, 20, 29, 35]. Hence, the scope of the present article is to fill the existing lacuna by studying the diffusion, permeation and solubility of H isotopes in Fe, Cr and W by DFT calculations.

Computational methods

The generalized gradient approximation (GGA) based Perdew-Burke-Ernzerhof (PBE) density functional [51, 53] using Vienna ab initio Simulation Package [54, 55] was used for all the calculations. The projector augmented wave (PAW) potentials [56, 57] were used to represents the ionic cores. The spin polarization was included for bcc-Fe, Cr and W. The Monkhorst–Pack special k-points [58] was used for integration in the Brillouin zone. During structural relaxation of the supercells, the atomic positions as well as supercell size were relaxed to equilibrium. The forces on all the atoms are kept less than 0.01 eVÅ^{-1}. The phonon calculations are performed using finite displacement method as implemented in the VASP package. The zero point energy (=1/2 $\sum_i h\nu_i$, ν_i is the frequency), ZPE was determined from the H atom frequency by performing phonon calculations by freezing the Fe, Cr and W atoms., Energy cut off and k-point sampling details can be found in the published literature for bcc Fe [1], Cr [2] and W [3] The standard nudged elastic band (NEB) method [59] is performed to find minimum energy paths and transition states for H atom diffusion.

Results and discussion

In a metallic membrane, H permeation occurs in seven steps (Fig.1): (1) adsorption of H_2 molecule at the high pressure side of the membrane, (2) dissociation of H_2 on the membrane surface, (3) penetration of H from surface to membrane bulk, (4) diffusion of H through the membrane bulk, (5) diffusion of H from membrane bulk to the surface on the collector side of the membrane, (6) recombination of H_2 molecule on the membrane surface, and (7) desorption of H_2 from the collector side surface of the membrane.

Validation of computational methodology

The calculated bond dissociation energy and vibrational frequency of H_2, D_2 and T_2 molecules are presented in Table 1. The calculated values were found to be in good match with the experimental values [60, 61].
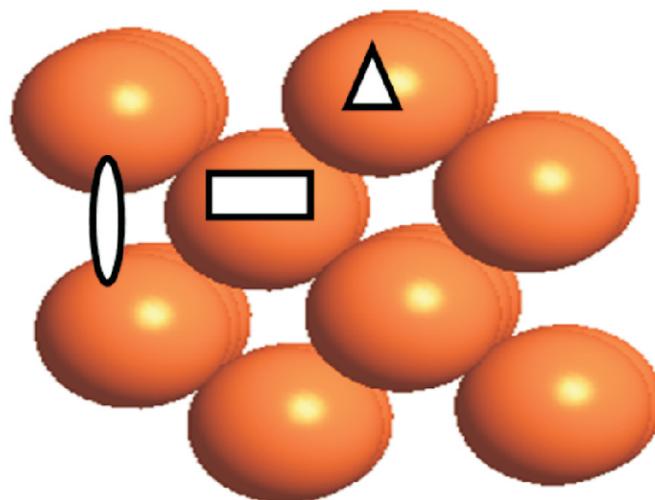
Fig.2: Fe(100) surface: triangle: atop, oval: bridge, rectangle: hollow position.

Table 1. Calculated values of D_e(eV),ν(cm^{-1}) and ZPE (kJ/mol) for isotopes of H_2 molecule.

Molecule	D_e		(ν)		ZPE	
	cal	Exp [61]	cal	Exp [60]	cal	Exp [62]
H_2	4.25	4.48	4258	4161	27.78	26.1
D_2	4.33	4.51	3011	2993	19.49	18.5
T_2	4.36		2458		16.40	

Dissociative adsorption of H_2 isotopes on (100) surface of Fe, Cr and W

A dissociative chemisorption of H_2 isotopes can readily take place on metal surface and the corresponding pathway followed by H_2 isotopes dissociation during this process is not fully understood. In the present calculations, we have considered the bridge positions as starting adsorption sites in which H_2 molecule is placed parallel to the surface. In the calculations, H_2 molecule was sequentially moved towards the surface and the positions of atoms were allowed to relax parallel to the surface plane. It was observed that initially the adsorption of H_2 molecule takes place. Further moving down towards surface leads to dissociation of H_2 molecule in close proximity of the surface. The zero point energy corrected adsorption energies for H_2, D_2 and T_2 with Fe, Cr and W (100) surface are plotted in Fig.3 and variation of H...H distances are presented in Fig. 4. The dissociative adsorption energies of hydrogen isotopes on the (100) surfaces were found to be in the order of E_{ad} (Fe) < E_{ad} (Cr) < E_{ad} (W).

Penetration of H from surface to membrane bulk

After adsorption of H atoms on the surface (S), the next move of H atom will be to migrate to subsurface (T1, T2.. etc), known as absorption. This will continue till it reaches membrane bulk.
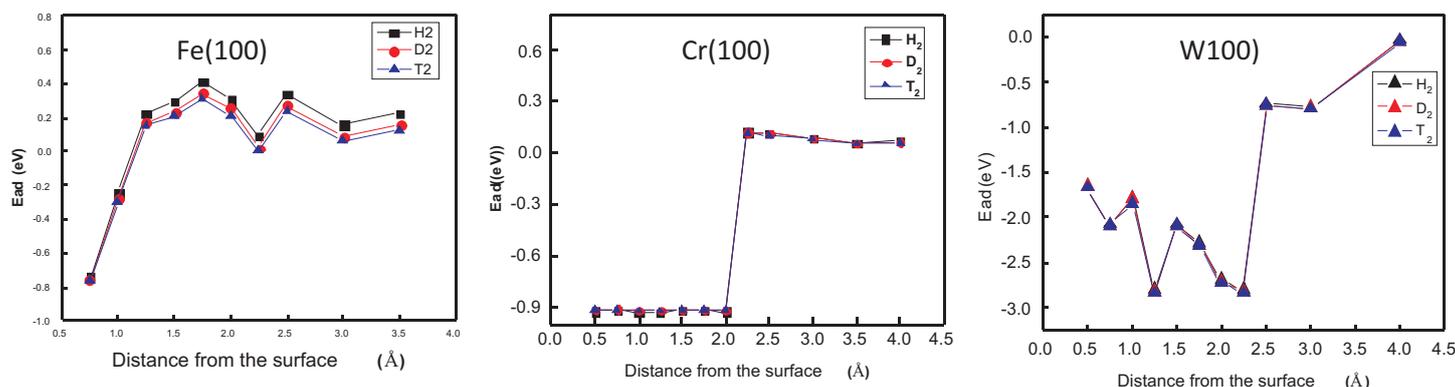
Fig.3: Potential energy surface for dissociative adsorption of H_2 and its isotopic molecules from bridge site to hollow site on (100) surface of Fe, Cr and W as function of the relative distance of H_2 from the surface.
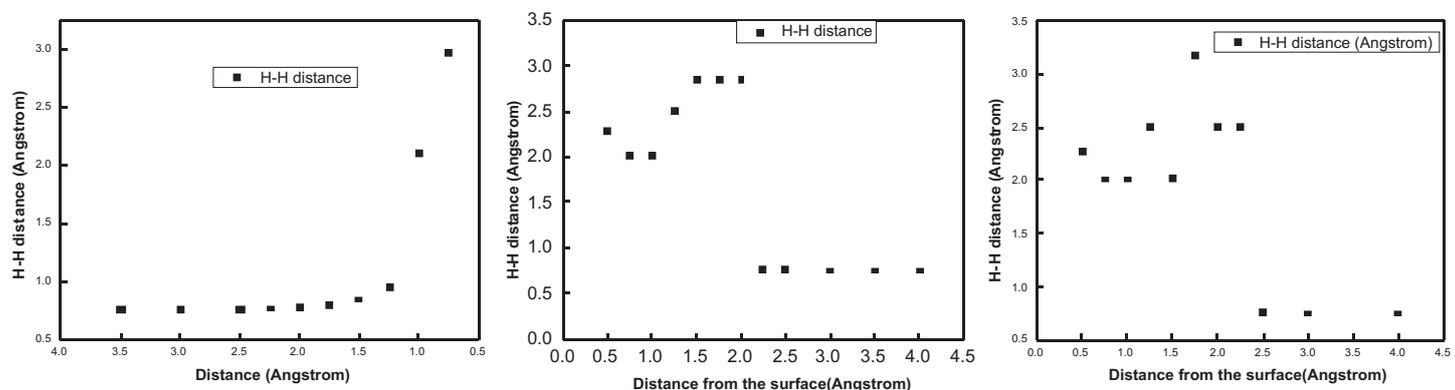
Fig.4: Variations of the H–H bond distances on (100) surface of Fe, Cr and W as function of the relative distance of H_2 molecule from the surface.
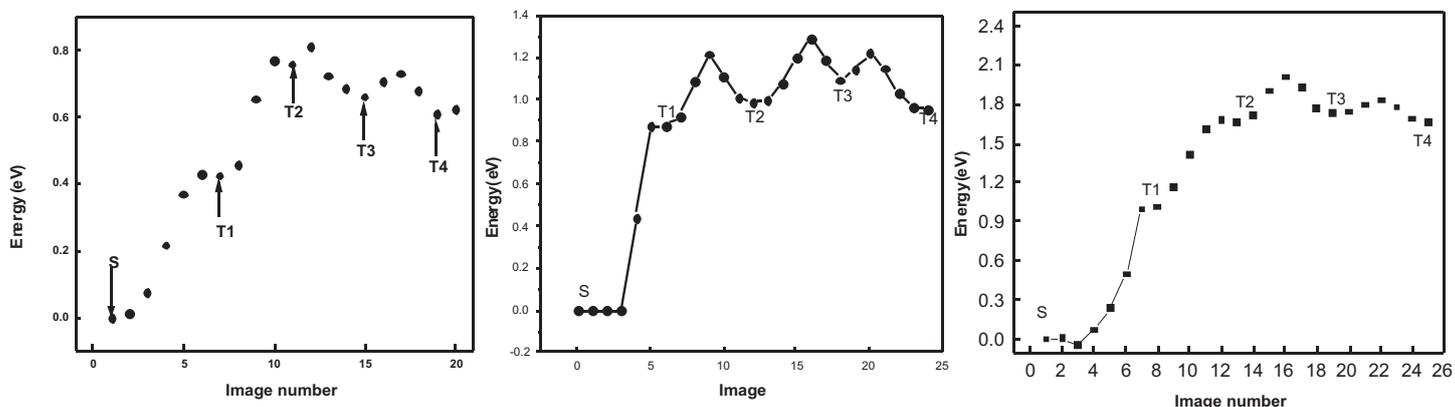
Fig.5: Potential energy surfaces for H diffusion from surface (S) to different sub surface (T1-T4) in Fe, Cr and W(100) surfaces.

NEB calculations were performed for H atom in hollow position(S) on the surface to the tetrahedral site in the various layers of the sub surface (T1, T2, T3 and T4) underneath the surface. Penetration of H from surface to membrane bulk in the case of Fe, Cr and W(100) surfaces were presented in Fig.5. From the calculations it is observed that the penetration H isotopes follows the following trend, $E_{H,D,T}$ (W_{S-T1}) > $E_{H,D,T}$ (Cr_{S-T1}) > $E_{H,D,T}$ (Fe_{S-T1}). Further the absorption energies of H isotopes in bulk Fe, Cr and W are calculated and presented in Table 2. From Table 2 it is observed that the H absorption in bulk W is more endothermic than Cr and Fe.

Diffusion of H through the membrane bulk

The diffusion of H and its isotopes is determined using transition-state theory with harmonic approximation[63] and the random-walk model [64]. The calculated energy barriers for the diffusion of H atom from one T_d site to nearest T_d site in bulk Fe, Cr and W was presented in Fig.6. The activation energy barrier without zero point energy correction was found to be 0.193eV for W [3] which is quite higher compared to pure Fe (0.072 eV) [1] and Cr (0.15eV) [2].

Further, to study the effect of temperature on diffusion, the diffusion constants are evaluated at different temperatures using simple Arrhenius equation. The results are presented in Fig.7. From figure, it is observed that the diffusion coefficients of H, D and T are found to be increased with increase in the temperature in case of Fe, Cr and W. The diffusion coefficients for H in W [3] are lower than for H in Cr [2] and H in Fe[1] and thus might be the reason for considering as plasma facing materials in fusion reactors.

Table 2. Absorption energies (E_{ab}) for hydrogen atoms in bulk Fe, Cr and W.

Bulk	Fe	Cr	W
M_{16}-H_o	0.40 (0.44,0.43,0.42)	0.927 (1.008,0.985,0.972)	1.285 (1.400,1.367,1.350)
M_{16}-H_T	0.20 (0.29,0.26,0.24)	0.718 (0.847,0.810,0.791)	0.909 (1.030, 0.995, 0.977)
M_{54}-H_o	0.43 (0.41,0.42,0.42)	1.040 (1.107,1.088,1.077)	1.156 (1.267, 1.236,1.219)
M_{54}-H_T	0.18 (0.29,0.26,0.23)	0.818 (0.945,0.909,0.890)	0.768 (0.887, 0.853, 0.835)
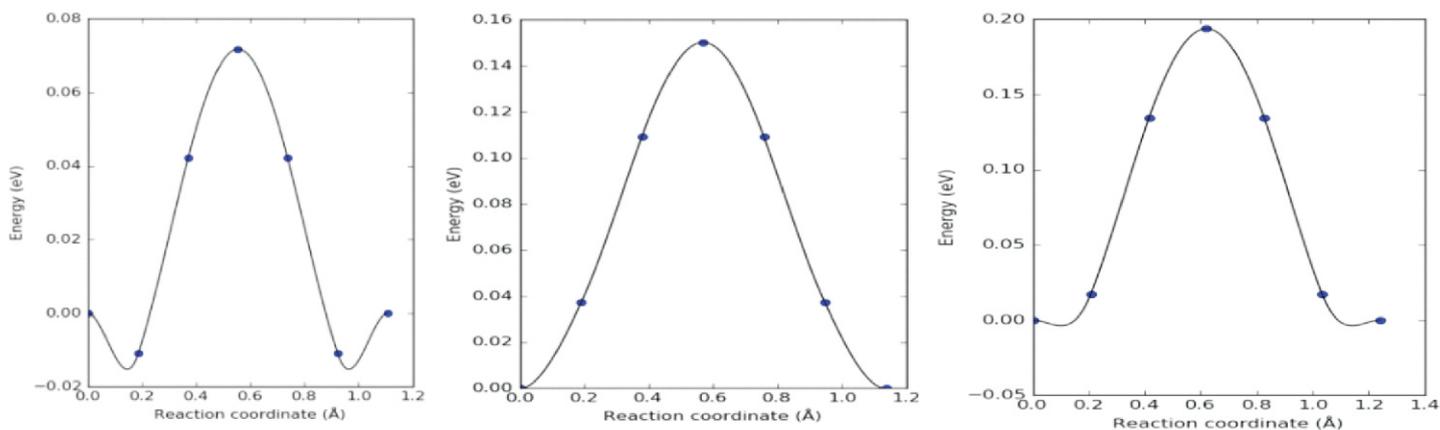
Fig.6: Energy profile for H diffusion from T-T site in bulk Fe , Cr and W.
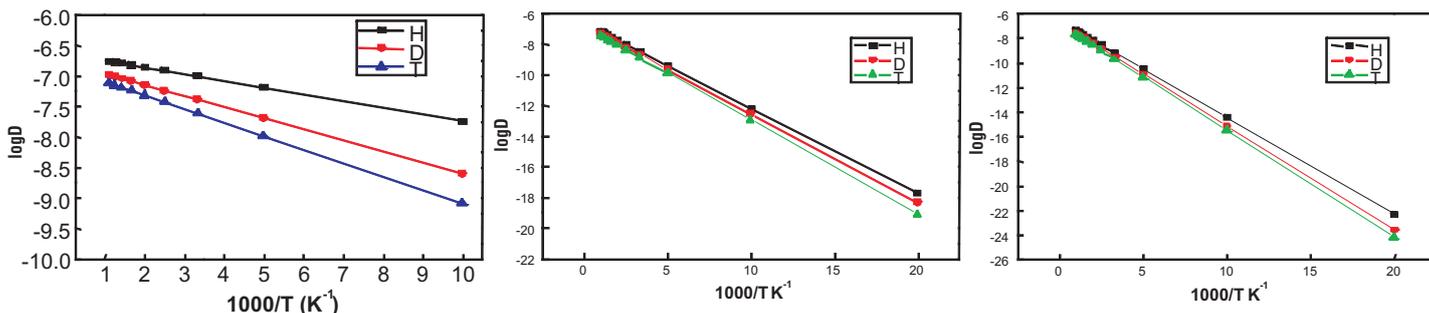
Fig.7: Diffusion coefficients of H, D and T at different temperatures for bulk Fe, Cr and W.
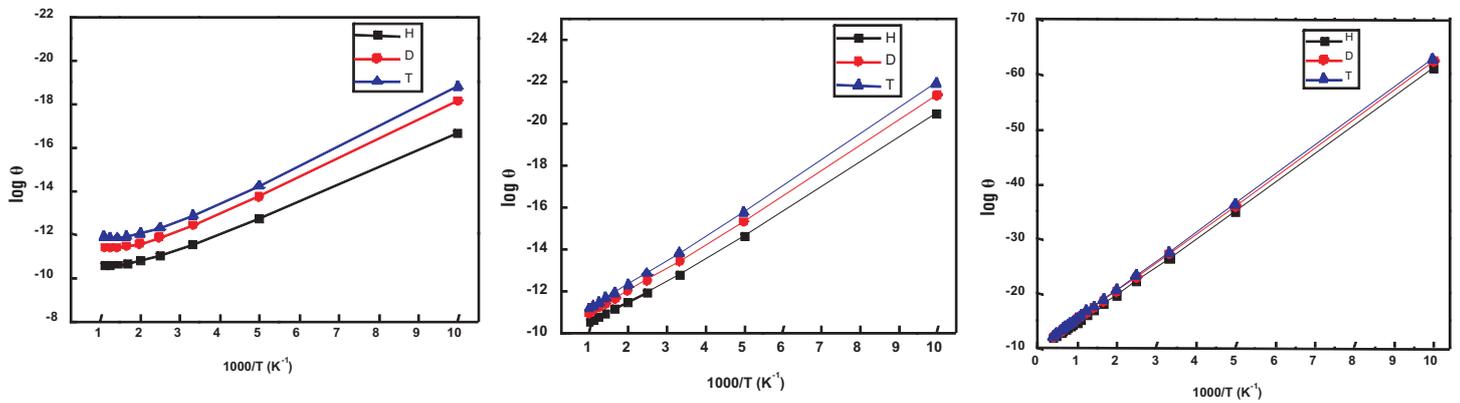
Fig.8: Permeability coefficients of H, D and T at different temperatures for bulk Fe, Cr and W.
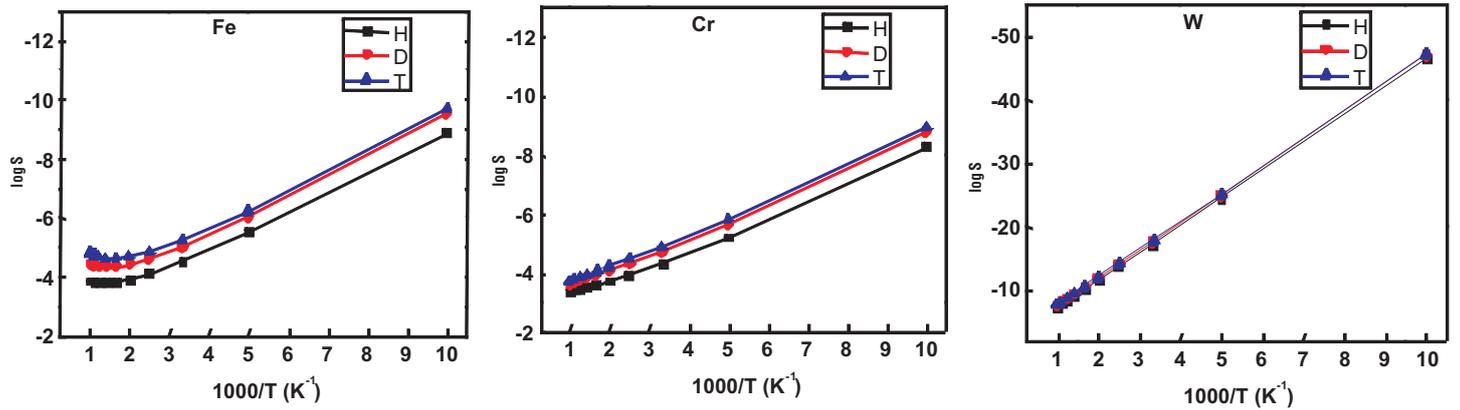
Fig.9: Solubility of H, D and T at different temperatures for bulk Fe, Cr and W.

Permeation and solubility of H_2 isotopes in membrane bulk

The gas permeability (Θ) can be computed using the well known relation [65] as given by the following expression:

$$\Theta = \tfrac{1}{2}\, K_s(T)\, D$$

where $K_s(T)$ is the Sieverts constant represents solubility and D is the diffusion coefficient. The calculated values of Θ for H_2, D_2 and T_2 in Fe, Cr and W at different temperatures are presented in Figure. 8 and respective solubility presented in Figure. 8 and respective solubility S, values are presented in Figure. 9. The permeability coefficients of H_2 is found to be higher compared to its heavier isotopes as expected due to its smaller mass with respect to D and T. Also, the permeation coefficients for H_2 in W [3] are lower than for H_2 in Cr [2] and H_2 in Fe [1]. Further, solubility of H_2 isotopes in Fe, Cr and W followed the similar trend of diffusion and permeation.

Conclusions

DFT calculations were performed to investigate the interaction and dynamical behaviours of hydrogen isotopes in pure bcc Fe, Cr and W. The adsorption and dissociation pathways for hydrogen isotopes were predicted on (100) surface of Fe, Cr and W. The dissociative adsorption energies of hydrogen isotopes on the (100) surfaces were found to be in the order of E_{ad} (Fe) < E_{ad} (Cr) < E_{ad} (W). Further, the penetration of H isotopes follows the trend, $E_{H,D,T}$ (W_{S-T1}) > $E_{H,D,T}$ (Cr_{S-T1}) > $E_{H,D,T}$ (Fe_{S-T1}). The activation energy barrier without zero point energy correction was found to be 0.193 eV for W which is quite higher compared to that for pure Fe (0.072 eV) and Cr (0.150 eV). Thus, the addition of Cr in Fe-Cr alloy helps in reducing permeation of H isotopes. The present observation is in correspondence with the experimentally observed low diffusivity of hydrogen in Fe-Cr steels. The calculated diffusion coefficients, permeability constants and solubility are found to be higher for H compared to its heavier isotopes D and T. The diffusion, permeation and solubility coefficients for H in W are lower than for H in Cr and H in Fe. Further, the calculated diffusion coefficients are shown to be lowest for W and thus might be the basis for considering W as plasma facing materials.

Corresponding Author*

Sk. Musharaf Ali (musharaf@barc.gov.in)

References

[1] A. Boda, S.M. Ali, K.T. Shenoy, S. Mohan, *J. Phys. Chem. C.*, 2019, **123**, 23951-23966.

[2] A. Boda, S. Bajania, S.M. Ali, K.T. Shenoy, S. Mohan, *J. Nucl. Mater*, 2021, **543**, 152538.

[3] A. Boda, M.A. Sk, K.T. Shenoy, S. Mohan, *Int. J. Hydrogen Energy* , 2020, **45**, 29095-29109.

[4] B. Zohuri, Plasma physics and controlled thermonuclear reactions driven fusion energy. Springer, Switzerland, 2016.

[5] L.M. Germeshuizen, P.W.E. Blom, *Int. J. Hydrogen Energy,* 2013, **38**, 10671-10682.

[6] A. Zielinski, S. Sobieszczyk, *Int. J. Hydrogen Energy,* 2011 **36**, 8619-8629.

[7] R.L. Klueh, A.T. Nelson, *J. Nucl. Mater.*, 2007, **371**, 37-52.

[8] V. Daaz, E. Teliz, F. Ruiz, P.S. Martanez, R. Faccio, F. Zinola, *Int. J. Hydrogen Energy,* 2013, **38**, 12811-12816.

[9] C. Joseph-Auguste, H. Cheikhravat, N. Djebaili-Chaumeix, E. Deri, *Int. J. Hydrogen Energy,* 2009, **34**, 5970-5975.

[10] E.S. Solntceva, M.L. Taubin, N.A. Bochkov, V.A. Solntsev, A.A. Yaskolko, *Int. J. Hydrogen Energy,* 2016, **41**, 7206-7212.

[11] E. Hayward, C.-C. Fu, *Physical Review B - Condensed Matter and Materials Physics,* 2013. **87**, 174103.

[12] D.E. Jiang, E.A. Carter, *Physical Review B - Condensed Matter and Materials Physics,* 2004, **70**, 064102-1-064102-9.

[13] J. Sanchez, J. Fullea, C. Andrade, P.L. De Andres, *Physical Review B - Condensed Matter and Materials Physics,* 2008, **78**, 014113.

[14] D.Di Stefano, M. Mrovec, C. Elsasser, *Physical Review B - Condensed Matter and Materials Physics,*2015, **92**, 224301.

[15] D.E. Jiang, E.A. Carter, *Physical Review B - Condensed Matter and Materials Physics,* 2003, **67**, 214103.

[16] J. Sanchez, J. Fullea, C. Andrade, P.L. de Andres, *Physical Review B,* 2008, **78**, 014113.

[17] P. Ferrin, S. Kandoi, A.U. Nilekar, M. Mavrikakis, *Surf. Sci.*, 2012, **606**, 679-689.

[18] C.L. Guerrero, N. Gordillo, R. Iglesias, J.M. Perlado, C. Gonzalez, Modell. Simul. *Mater. Sci. Eng.*, 2016, **24**, 045006.

[19] K. Heinola, T. Ahlgren, *Phys. Rev. B,* 2010, **81**, 073409.

[20] D.F. Johnson, E.A. Carter, *J. Mater. Res.*, 2010, **25**, 315-327.

[21] K. Kwak, M. Chou, N. Troullier, *Phys. Rev. B,* 1996, **53**, 13734-13739.

[22] G.H. Lu, H.B. Zhou, C.S. Becquart, *Nucl. Fusion,* 2014, **54**, 086001.

[23] A. Moitra, K. Solanki, *Comput. Mater. Sci.,* 2011, **50**, 2291-2294.

[24] A. Nojima, K. Yamashita, *Surf. Sci.*, 2007, **601**, 3003-3011.

[25] Z.A. Piazza, M. Ajmalghan, Y. Ferro, R.D. Kolasinski, *Acta Mater,* 2018, **145**, 388-398.

[26] L. Sun, S. Jin, G.H. Lu, L. Wang, *Scripta Mater,* 2016, **122**, 14-17.

[27] L. Sun, Y.-N. Liu, W. Xiao, M. Zhou, *Mater. Today. Comm.,* **17**, 2018, 511-516.

[28] J. Wang, Y. Zhang, H.B. Zhou, S. Jin, G.H. Lu, *J. Nucl. Mater,* 2015 **461**, 230-235.

[29] N. Fernandez, Y. Ferro, D. Kato, *Acta Mater,* 2015, **94**, 307-318.

[30] K. Heinola, T. Ahlgren, *J. Appl. Phys.*, 2010, **107**, 113531.

[31] J. Xu, J. Zhao, *Nuclear Instruments and Methods in Physics Research, Section B: Beam Interactions with Materials and Atoms,* 2009, **267**, 3170-3174.

[32] E.D.V. Gómez, S. Amaya-Roncancio, L.B. Avalle, D.H. Linares, M.C. Gimenez, *Appl. Surf. Sci.*, 2017, **420**, 1-8.

[33] L. Zhang, L. Qiao, T. Bligaard, Y. Su, *Appl. Surf. Sci.* **457** (2018) 280-286.

[34] S.T. Picraux, F.L. Vook, *Phys. Rev. Lett.*, 1974 **33** 1216-1220.

[35] Y.L. Liu, Y. Zhang, G.N. Luo, G.H. Lu, *J. Nucl. Mater,* 2009, **390-391**, 1032-1034.

[36] R. Frauenfelder, *J. Vac. Sci. Technol.*, 1969, **6,** 388-397.

[37] R. Frauenfelder, *J. Chem. Phys.,* 1968, **48**, 3955-3965.

[38] T. Tanabe, *Phys. Scr. T ,* 2014, **159**, 014044.

[39] E.A. Aitken, H.C. Brassfield, P.K. Conn, E.C. Duderstadt, R.E. Fryxell, *Trans. Met. Soc. AIME,* 1967, **239**, 1565.

[40] G. Benamati, E. Serra, C.H. Wu, *J. Nucl. Mater,* 2000, **283-287**, 1033-1037.

[41] D.A. Buchenauer, R.A. Karnesky, Z.Z. Fang, C. Ren, Y. Oya, T. Otsuka, Y. Yamauchi, J.A. Whaley, *Fusion Eng. Des.*, 2016, **109-111**, 104-108.

[42] G.A. Esteban, A. Perujo, L.A. Sedano, K. Douglas, *J. Nucl. Mater,* 2001, **295**, 49-56.

[43] T. Ikeda, T. Otsuka, T. Tanabe, *J. Nucl. Mater*, 2011, **415**, S684-S687.

[44] T. Ikeda, T. Otsuka, T. Tanabe, *Fusion Sci. Technol.*, 2011, **60**, 1463-1466.

[45] H. Nakamura, W. Shu, T. Hayashi, M. Nishi, *J. Nucl. Mater,* 2003, **313-316**, 679-684.

[46] T. Oda, *Fusion Eng. Des.*, 2016 **112**, 102-116.

[47] T. Otsuka, T. Hoshihira, T. Tanabe, *Physica Scripta,* 2009, **TT138**, 14052.

[48] M. Shimada, R.J. Pawelko, *Fusion Eng. Des.*, 2019, **146**, 1988-1992.

[49] A.P. Zakharov, V.M. Sharapov, E.I. Evko, *Soviet Mater. Sci.*,1975, **9**, 149-153.

[50] W.J. Arnoult, R.B. McLellan, *Acta Metall,* 1973, **21**, 1397-1403.

[51] J.P. Perdew, K. Burke, M. Ernzerhof, *Phys. Rev. Lett.*,1996, **77**, 3865-3868.

[52] J.P. Perdew, K. Burke, M. Ernzerhof, *Phys. Rev. Lett.*, **80**, 1998, 891.

[53] J.P. Perdew, J.A. Chevary, S.H. Vosko, K.A. Jackson, M.R. Pederson, D.J. Singh, C. Fiolhais, *Phys. Rev. B,* 1992, **46**, 6671-6687.

[54] G. Kresse, J. Furthmuller, *Phys. Rev. B,* 1996, **54**, 11169-11186.

[55] G. Kresse, J. Hafner, *Phys. Rev. B,* 1993, **47**, 558-561.

[56] P.E. Blöchl, *Phys. Rev. B ,* 1994, **50**,17953-17979.

[57] G. Kresse, *Phys. Rev. B,* 1999, **59**, 1758-1775.

[58] H.J. Monkhorst, J.D. Pack, *Phys. Rev. B*, 1976, **13**, 5188-5192.

[59] H. Jansson, G. Mills, K.W. Jacobsen, Classical and Quantum Dynamics in Condensed Phase Simulations, *WORLD SCIENTIFIC,* 1998, p. 385-404.

[60] B.P. Stoicheff, *Canadian Journal of Physics,* 1957, **35**, 730-741.

[61] D. Sprecher, C. Jungen, W. Ubachs, F. Merkt, Faraday Discussions, 2011, **150**, 51-70.

[62] K.K. Irikura, *Journal of Physical and Chemical Reference Data,* 2007, **36**,389-397.

[63] G.H. Vineyard, *Journal of Physics and Chemistry of Solids,* 1957, **3**, 121-127.

[64] C. Wert, C. Zener, *Physical Review,* 1949, **76**,1169-1175.

[65] B.D. Morreale, M.V. Ciocco, R.M. Enick, B.I. Morsi, B.H. Howard, A.V. Cugini, K.S. Rothenberger, *J. Membr. Sci.*, 2003, **212**, 87-97.

Molecular Dynamics Simulations

Radionuclide-Ligand-Solvent Systems in Fuel Reprocessing

Arya Das[1,3] , ***Sk. Musharaf Ali**[2,3]

[1]Nuclear Recycle Board, Bhabha Atomic Research Centre, Mumbai-400085, India
[2]Chemical Engineering Group, Bhabha Atomic Research Center, Mumbai-400085, India
[3]Homi Bhabha National Institute, Mumbai-400094, India

ABSTRACT

Spent fuel reprocessing is necessary to manage the nuclear fuel volume and also to produce the fresh fuel for fast reactor to maintain the closed fuel cycle. Various ligand-solvent systems are manipulated to achieve the best performance depending on the nature of the waste and type of the equipment. Therefore, one of the most crucial point is the selection of the ligand-solvent systems amongst myriads of ligands and solvents which is experimentally quite tedious and expensive. Molecular dynamics (MD) simulation and Quantum electronic structure calculation (QESC) have been emerged as virtual experimental methods for designing the effective ligand-solvent systems. Extensive calculations demonstrate that tri-iso-amyl phosphate (TiAP) is a viable alternative of tri-n-butyl phosphate (TBP) in the fuel reprocessing.

Keywords: Fuel reprocessing, Uranyl ion, TiAP, Dodecane, QESC, MD simulations.

Introduction

Among the various sources of energy, nuclear energy shares ~15-20% of the total energy consumption worldwide. In view of the growing energy demand, fission-based nuclear power which has proven to be safe and reliable will play a vital role in meeting this need. One aspect of nuclear power that still provides significant technical challenges is the management of continuously increasing spent nuclear fuel in large volumes which necessitates the development of an effective and selective methodology for reuse by separation of actinides. Reprocessing of used nuclear fuel is of practical interest not only to reduce the high-active solid waste and its safe disposal but also to produce the fresh fuel for 2nd generation nuclear reactor.[1] The most commonly practiced extraction process is PUREX (Plutonium Uranium Recovery by Extraction) in which the Uranium and Plutonium are separated from aqueous solution obtained from the dissolution of irradiated fuel in nitric acid. The key extractant in PUREX process is tri-n-butyl phosphate (TBP) which is commonly used with dodecane as diluent. In spite of proven success of TBP as popular ligand; it has some inherent limitations that reduce the efficiency of the extraction process. Third phase formation in the extraction of Pu(IV), degradation due to radiological and chemical effects and the aqueous solubility are the serious issues with TBP. It is desirable to develop an alternate ligand which has the advantages of TBP and mitigates the demerits of TBP.[2] Therefore, a detailed investigation on the structural and thermo-physical properties of pure ligands as well as in binary and biphasic mixture and the related dynamical properties for the metal extraction is of utmost necessary for better understanding of the extraction process.

To avoid various issues in performing experiments, molecular dynamics (MD) simulations and Quantum electronic structure calculations (QESC), which are very useful methods for investigating the microscopic structure and thermophysical properties are conducted. In past, several works have been carried out for the development of a force field which can predict the structural properties with suitable accuracy. For this purpose different atomic partial charges have been used to parameterize the force field in the last few decades. Recently, Cui et al have calculated the structural and thermophysical properties of TBP/dodecane mixture with two sets of force fields.[3]Mu et al stated that a single model cannot predict both the structural and thermo dynamical properties.[4]Cui et al reported that the structure is highly affected by the partial charge on TBP molecule.[5]Recently, Siu et al have refined the parameters of OPLS-AA (All-atom Optimized Potential for Liquid Simulations) force field for long hydrocarbons to reproduce the values of densities and heats of vaporization.[6] Vo et al worked for parameterization of force field based on the experimental density and the heat of vaporization.[7] Leay et al described the pathway of polar molecules from the aqueous phase to the organic phase through filament network.[8] Further, Mu et al have studied shear viscosity of TBP from non-equilibrium MD (NEMD) using periodic shear flow method.[4] Allen et al calculated the viscosity of alkanes from NEMD using parameterized OPLS model.[9] Though the parameterization of force field has been carried out based on density or dipole moment or heat of vaporization to calculate the structural and dynamical properties of ligand and ligand-solvent systems but it is case sensitive.

Further, it is equally important to study the behavior of TiAP/dodecane mixture in contact with aqueous phase in the presence of nitric acid. The calculation of interfacial properties are also required to understand the mass transfer through interface as it is difficult to explore the molecular details using experimental technique. Baaden et al have performed MD simulation focusing on the mixing and de-mixing of aqueous–organic solution and their interfacial distribution, but did not calculate the interfacial tension (IFT) and interface thickness (IFW).[10] Sahu et al have studied uranyl extraction using TBP and reported higher water extraction with

un-dissociated HNO$_3$ compared to dissociated form of acid. The calculation of capillary thickness, total IFW and IFT was untouched. Furthermore, a considerable progress has been observed in the calculation of IFT using MD simulation in recent past.[11] Wen and co-workers revealed the increment of decane–water interfacial tension at low ionic concentration. They also did not focus on the calculation of IFW.[12] Biswas *et al* reported an enhancement of surface tension with the addition of metal salt.[13] Jorge *et al* estimated the total and intrinsic interface width for water–nitrobenzene system by fitting density profile where the proper prescription for calculation of total IFW is lacking and also not been addressed the presence of third component and acidity.[14] Senapati *et al* calculated the IFW and IFT of CCl$_4$/water system based on two different methods and computed the interface width by fitting the density curve but didn't study the effect of third component.[15] Hence, there are lots of ambiguity in the calculation of total and intrinsic interface thickness and no straightforward prescription is still available.

A theoretical and computational investigations on thermo-physical and dynamical behavior of aqueous actinides are essential because of the limitation in conducting the experiments due to radio-toxicity and also precise determination of their variable oxidation states and coordination numbers in aqueous solution. Earlier, several research groups have developed force field to model uranyl ion based on QM and MD simulations. Gulibaud and Wipff presented a theoretical study of uranyl ion in water.[16] Kerisit *et al* carried out simulations of UO$_2^{2+}$ in water using GW and two other force fields to show that not a single model is able to predict the uranium–water oxygen distance or or hydration free energy.[17] Rai *et al* developed a force field using to establish the importance of using many body solvation effects for development of force field.[18] Therefore, concerns regarding the different charge models are really required to understand the hydrated uranyl ion. Further, literature reviews also depicted that the earlier studies on uranyl ion were carried out in water only. So, it is important to perform the studies in presence of nitric acid to reflect the practical experimental conditions.

The objective of the present article is to summarize the modified OPLS-AA force field using Mulliken, Löwdin, NPA (natural population analysis) and ChelpG (a grid based method using electrostatic potential) partial charge by studying the structural, thermo-dynamical and dynamical properties for pure TBP, TiAP and TEP which help in the screening of ligands for the extraction applications. Another objective is to test the calibrated force field in TiAP/dodecane binary mixture as well as in water–TiAP/dodecane biphasic mixture to see whether the force field is able to explain all the structural, thermo-dynamical and dynamical properties. An attempt has also been made for the calculation of total and intrinsic interface thickness for simple as well as complex biphasic mixture to understand the interfacial process. The versatility of force field is the main appeal of the current studies. The forth objective is to find out the effect of partial charges on actinides in water and then to calculate the various structural and dynamical properties of uranyl nitrate in nitric acid medium with wide range of uranyl nitrate as well as acid concentration.

Computational Details

All the MD simulations were performed using GROMACS-4.5[19] package employing usual periodic boundary conditions and OPLS-AA force field. The initial molecular structures and partial charges on the each atom are computed at the B3LYP/TZVP[20] level of theory as implemented in TURBOMOLE[21] and GAMESS[22] packages. During simulation, the long range electrostatic interactions are computed using particle mesh Ewald (PME)[23] method with an order of 6 and with a cutoff distance of 12Å. SPC/E[24] water model is used as it is more efficient compared to other models. The systems are equilibrated for 10ns in NPT ensemble with a time step of 2fs. Pressure of 1 atm is maintained using Berendsen like weak coupling methods and Velocity–rescaling thermostat is used to converge the temperature (T=300K). Additional 10ns production run in NVT ensemble is performed.

Results & Discussion

The ligands considered for study are generally optimized and then used for initial coordinate input in the MD simulation (Fig.1).
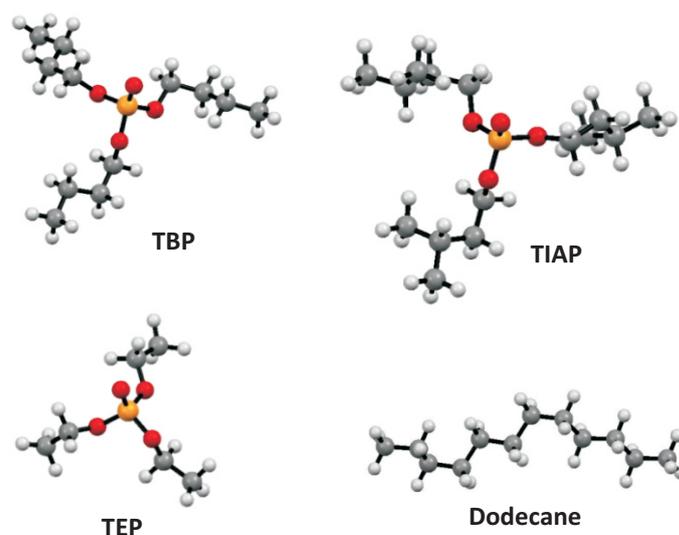
Fig.1: Optimized structures of ligand/solvent (red: O; orange: P; gray: C and white: H).
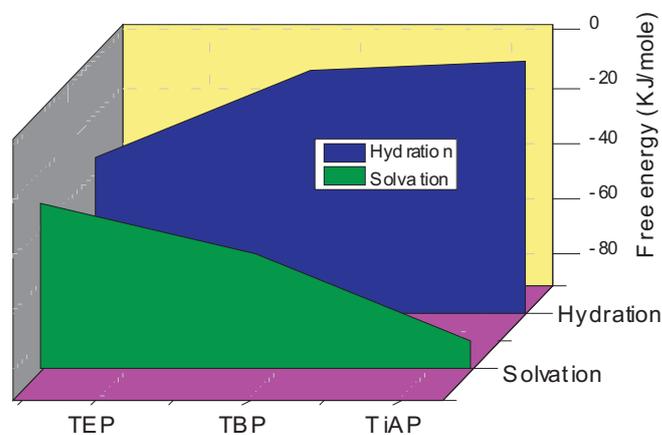
Fig.2: Calculated free energy of hydration and solvation for ligands in water and dodecane.

The calculated mass density, dipole moment and self-diffusivity of pure ligands using Mulliken population analysis are in good agreement with experimental data within 1% deviation indicating the best selection. Structural properties also support this fact. The acceptability of the Mulliken charge embedded force field further confirmed from the computation of $\Delta G_{Hydration}$ and $\Delta G_{Solvation}$ using Thermodynamic Integration (TI)[25] method. The screening of ligand has been carried out based on free energy and partitioning ability. The free energy studies exhibited the higher hydrophobic nature of TiAP compared to others and also higher degree of partitioning of TiAP in organic phase which are very much desirable for biphasic extraction[26] (see Fig. 2).

The larger the difference in hydration and solvation for TiAP, higher the free energy of transfer leading to higher partitioning of solute between two phases. The study also confirmed that TiAP has the higher partitioning ability. The increasing value of partition coefficient of alkyl phosphates with increasing alkyl groups is attributed to increasing hydrophobic alkyl group because the solubility of the tri-alkyl phosphates in water is decreased and increased in dodecane which in turn enhances the partitioning of the solute in dodecane. The heat of vaporization, ΔH_{vap} of the liquid is in fair agreement with the experimental results. Finally the free energy of extraction, ΔG_{ext} of UO_2^{2+} ion in water-dodecane system showed that the TiAP has the higher free energy of extraction than that of TBP which reflects the higher distribution constant of UO_2^{2+} ion with TiAP ($D_{U(VI)}$=29.8) over TBP ($D_{U(VI)}$=24.5) and hence TiAP might be used as an alternative of TBP.[26]

Next, it is desirable to test the Mulliken embedded force field in binary mixture at various mole fraction of TiAP. The calculated densities are in good agreement with the experimental values signifies the accuracy of force field. Also, it correctly predicts the temperature effect on density of pure liquids and binary mixture with a deviation of 0.35-0.80%. The excess volume of mixing which signifies the interactions between the components of mixture was also calculated (Fig.3). The correct trend for excess volume of mixing confirms the accuracy of the force field.[27]

The structural properties reveal two possible orientations of neighbor TiAP molecules like
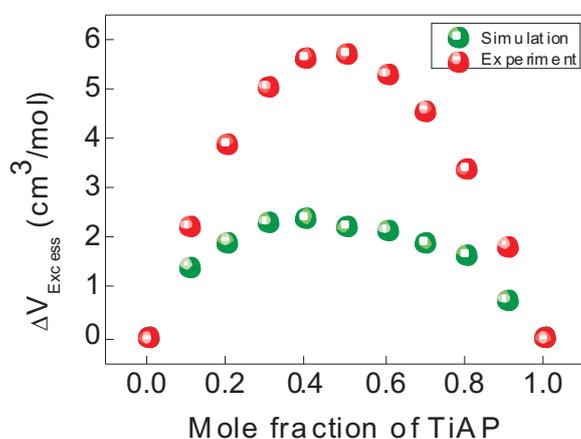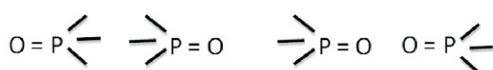
Fig.3: Excess volume of mixing of TiAP-dodecane.
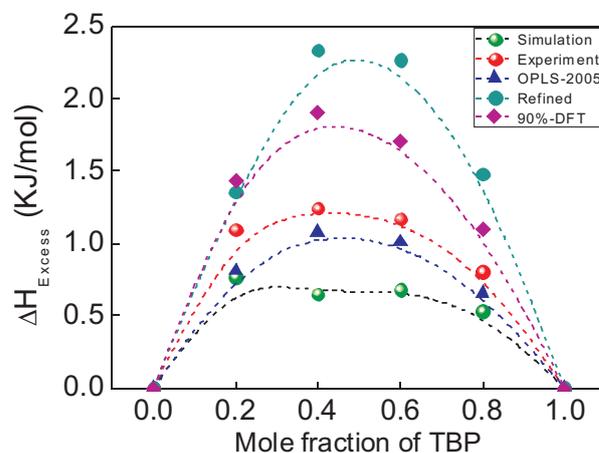
Fig.4: Excess enthalpy of TBP/dodecane mixture.
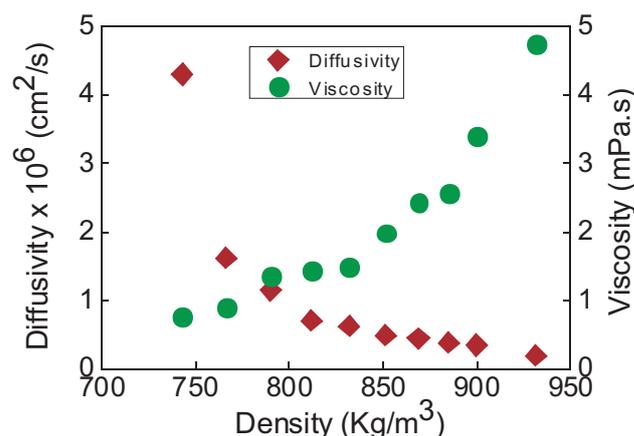
Fig.5: Diffusivity of TiAP and shear viscosity of TiAP-dodecane mixture as a function of density.

First one is from the hydrophobic side of the two different TiAP molecules and it is difficult to approach each other due to the large iso-amyl group and the second is from the phosphoryl group where the dipole–dipole interactions come into picture.[27] The calculation of excess enthalpy of mixing at different mole fraction of TBP predicts correctly the endothermic mixing as it was found experimentally (Fig.4). For TiAP also, ΔH_{Excess} follows the trend and ensures the accuracy of developed force field.

The self-diffusivity (using Einstein's relation[28]) and shear viscosity (using periodic perturbation method from NEMD[29]) have been calculated. The dynamic properties of ligands play an important role in the mobility of the ligand which is a determining factor for the formation of metal–ligand complex. The effect of mole fraction of TiAP on self-diffusivity shows a decreasing trend with increasing mole fraction. The calculated viscosity of TBP is very close to the experimental value with a deviation of 0.25%, indicating a good accuracy of developed force field. For TiAP, it is 4.74 ± 0.03 mPa.s (expt.: -4.27mPa.s). The shear viscosity of TiAP/n-dodecane binary mixture follows an increasing trend with mole fraction of TiAP.[27] The dynamic properties change with mole fraction. So, it is crucial to select the useful composition of TiAP/dodecane mixture to develop efficient extraction system. The low viscosity and high diffusivity are the major criteria for the selection of composition of any ligand–solvent system. The shear viscosity is shown to be an increasing function of mole fraction whereas diffusivity of TiAP is a decreasing function. So, it is important to select an optimum composition which is around 25–30% TiAP where the curves are intersecting each other as shown in Fig.5. This composition exhibits
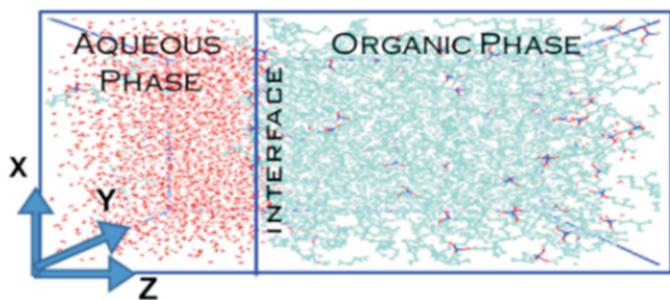
Fig.6: A biphasic (organic: aqueous) simulation box. red-water, blue-TiAP and cyan-dodecane.
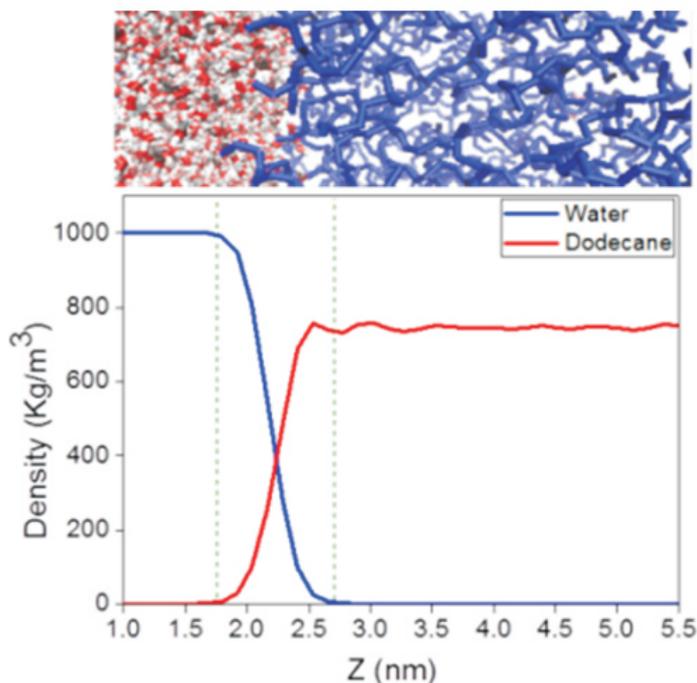
Fig.7: Density profile of water–dodecane system (water: Red/White) and dodecane: Blue).

Fig.8: Snapshot of liquid structure and density profiles for 10%, 20%, 30% and 40% of TiAP in dodecane-water system. Cyan: dodecane, Red & White: water, Red & Grey: phosphoryl group of TiAP.
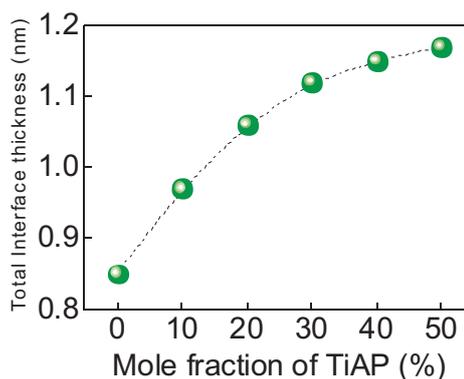
Fig.9: Interface thickness vs. mole fraction of TiAP.

a good value of self-diffusivity of TiAP and a low value of shear viscosity.[27]

MD simulations in TiAP/dodecane mixture demonstrate that the Mulliken embedded force field captures most of the structural, dynamical and thermo-dynamical properties of ligand-solvent system. Therefore, it is also important to test this force field in biphasic mixture.[27] The starting simulation box is prepared by placing the ligand (TiAP) in the organic phase (dodecane) and water containing nitric acid as the aqueous phase as depicted in Fig. 6.

First, the force field is tested for simple water–dodecane system. The computed average bulk density of water and dodecane away from the interface is in quite good agreement with the reported experimental values.[30] A sharp interface is observed as displayed in Fig. 7.

In TiAP/dodecane–water biphasic system, the interface become sharper after 1500ps and TiAP molecules are accumulated at the interface which increases the interface roughness as well as interface area. The accumulation at the interface increases with increasing mole fraction leading to higher interfacial area (Fig. 8).[30]

The interfacial thickness is seen to increase with TiAP in Fig. 9. The interface thickness is affected up to a certain mole fraction of TiAP (here 50%). Above 50%, it remains almost invariant and therefore further increase of TiAP will not help in the mass transfer.[30]

The interaction, E_{int} between water molecules is reduced in the presence of TiAP. The breakage of H-bond among water molecules reduces the surface tension of water which helps to increase the mingling of water and organic phases. Therefore, higher packing of TiAP at the interface accelerates the hydration of TiAP and thus leads to more reduction of the interfacial tension. The O--H bond (1.81Å) in TiAP-H_2O complex (O of P=O and H of water molecule) is found to be quite smaller than O--H bond (2.16Å) in water dimer indicating that the TiAP-H_2O interaction is stronger than that of H_2O-H_2O interaction as reflected in the interaction energy. The E_{int} for TiAP-H_2O interaction (-10.74kcal/mole) is found to be higher than that of H_2O-H_2O interaction (-4.63kcal/mole) at the B3LYP/TZVP level of theory. The O--H bond length in TiAP-H_2O complex (O of P=O and H of water) from MD simulation was found to be 1.55Å

Table 1. Interfacial tension (IFT) and interface thicknesses (IFW) of neutral biphasic system at T=300°K.

TiAP (%)	IFT (mN/m)		IFW (nm)		
	Simulation	Expt [31]	w_c	w_t	w_i
0	49.3± 1.6	52.6	0.202	0.767	0.740
10	28.7± 2.0	35.3	0.261	0.996	0.961
20	27.1± 2.3	25.5	0.268	1.03	0.994
30	24.4± 2.9	20.5	0.283	1.091	1.054
40	23.2± 2.1	18	0.291	1.126	1.088

Fig.10: Total interface thickness as a function of mole fraction. Capillary thickness and interfacial tension vs. mole fraction of TiAP [inset of Fig 10].

whereas it is 1.95Å for water, which might be reasonable due to different physical state of the molecular system in MD and QM.[30]

The interface thickness is changed with acid and it exhibits a decreasing trend. The inverse relation between interfacial tension and interface thickness is established for water–TiAP/dodecane system [inset of Fig. 10]. They are related by capillary wave theory (CWT)[32] as

$$w_c^2 = \frac{k_B T}{2\pi\gamma} \ln\left(\frac{L_{II}}{L_b}\right) \quad (1)$$

here, w_c is the interface thickness due to capillary wave, k_B is Boltzmann constant, L_{II} is the box dimension along x or y direction and L_b represents bulk correlation length in terms of molecular length. The molecular diameter is evaluated from the volume determined by COSMOtherm program. The calculated w_c (water–dodecane) was (0.20nm) very close to reported value of 0.33nm. In the presence of TiAP it is more appropriate to introduce the weighted average of TiAP and dodecane for L_b.[30]

$$L_b = L_{W-T} * x_{TiAP} + L_{W-D} * x_{Dodecane} \quad (2)$$

L_{W-T} and L_{W-D} are the average molecular lengths considering water–TiAP and water–dodecane interface respectively. X_{TiAP} and $X_{dodecane}$ are the mole fraction of TiAP and dodecane. Further, the total interface are the mole fraction of TiAP and dodecane. Further, the total interface thickness (w_t) can be well fitted to an equation as follows:

$$w_t^2 = C \frac{k_B T}{\gamma} \ln\left(\frac{L_{II}}{L_b}\right) \quad (3)$$

$$C = \frac{(\sigma_{Water} + \sigma_{TiAP} + \sigma_{dodecane}}{1.4 \, \sigma_{water}} \quad (4)$$

w_t obtained from the density curve and from the proposed equation (Eqn.3 & Eqn. 4) using the molecular length (L_b) calculated from the weighted average method are in good agreement as shown in Fig.10 as a function of mole fraction of TiAP and acid concentration.[30]

The interface thickness calculated from the density profile is substantially high compared to w_c indicating that w_c is not the sole contributor. Hence, it is inappropriate to propose w_c as the true interface thickness. The contribution from intrinsic thickness (w_i) is obtained as:

$$w_i^2 = w_t^2 - w_c^2 \quad (5)$$

The calculated value of w_i for water-dodecane system using Eqns. 3, 4 and 5, was 0.74nm which is very close to the reported MD simulation value of 0.51nm and thus confirms the approval of the model equation (Eqn.3 & Eqn.4).[30] The calculated w_t, w_c and w_i for various compositions of TiAP and acidity are listed in Table 1. The predictability of the proposed equation for calculation of interface thicknesses (nm) lies within 60–70%.

The preferential orientation of phosphoryl group at the interface has also been evaluated. The interface has quite negligible effect on the orientation of water molecule while the orientation of TiAP molecule has been changed markedly in the presence of interface compared to pure state. From the snapshot it was seen that the phosphoryl oxygen from one TiAP unit is facing the back of the P of P=O of the neighboring TiAP unit (Fig.11).

Further, the stability of the dimer with different orientation was established by computing the dimerization energy by dispersion corrected DFT. The interaction energy for dimer with orientation of O=P-P=O, P=O-P=O and P=O-O=P was found to be -12.98, -14.97 and -10.81 kcal/mole respectively indicating that dimer with orientation of P=O-P=O is the most stable which was also captured
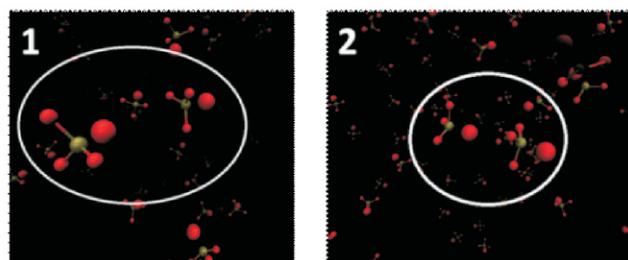
Fig.11: Preferential orientation (P=O-P=O) of phosphoryl group of TiAP molecules.

Table 2. Partial charges on U (qU) and O (qO) of uranyl.

Model	$q_U (e)$	$q_O (e)$
Model - MA(Mulliken)	2.719	-0.3595
Model - GW(Gulibaud and Wipff)	2.500	-0.2500
Model - ML(Mulliken - Liquid)	2.198	-0.0992
Model - MG(Mulliken - Gas)	2.033	-0.0164

Fig.12: Density of uranyl nitrate solution in 3M nitric acid at various concentrations.

in the MD simulation.[30] The simulation studies in biphasic system also reveal that a single force field without parameterization is able to predict structural, dynamical and thermo-dynamical properties in pure, binary and biphasic system. Next, simulations were conducted to find out the limiting feed concentrations in PUREX process. The effects of partial charges on uranyl ion were studied to find out the correct model amongst available force fields (Table 2).

After calculation of structural, dynamical and thermo-dynamical properties for uranyl ion in water system it is observed that the variation in atomic charges does not have much significant effect on the force field except the free energy of hydration where the partial charges have significant effect. Here, GW model was chosen for the uranyl ions due to accurate hydration free energy. The systems considered here are for a wide range of uranyl nitrate concentration from 0.25-5.45 mole/lit in 3M nitric acid.[33] The calculated bulk densities of each system were found to increase with uranyl nitrate concentration The experimental results exhibit an excellent agreement with the densities obtained from MD simulations (Fig. 12).
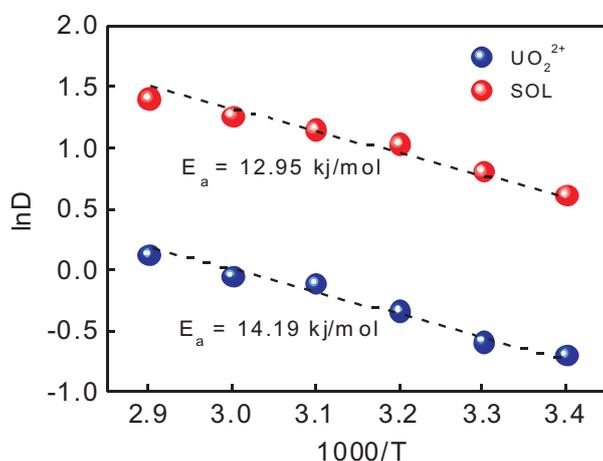
Fig.13: Arrhenius plot of diffusivity against temperature (uranyl nitrate:0.5 moles/lit).

Fig.14: Snap shot of bi- and mono-dentate nitrate ions. Red-O, Blue-N and Pink-U.
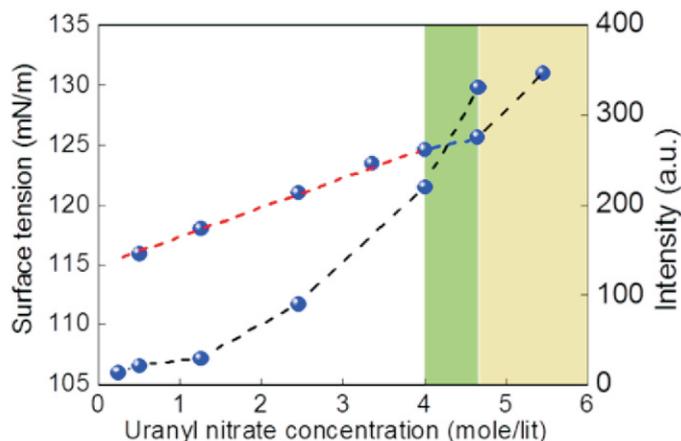
Fig.15: Calculated surface tension of uranyl nitrate solution and experimental intensity using DLS.

The diffusivity of UO_2^{2+} ion and water is decreased with uranyl nitrate concentration due to increased friction. The temperature dependency on self-diffusivity has also been studied using the Arrhenius equation[34] and the dependency is found to be linear as shown in Fig. 13.

The bi-dentate structure is formed at low concentration and mono-dentate at higher uranyl ion concentration. This is because more number of uranyl ions reduce the availability of nitrate ions around UO_2^{2+} and also there a competition between water and nitrate ion to occupy the first solvation shell[33] (Fig. 14).

Surface tension plays an important role in the liquid–liquid extraction and in particular in stripping operation of various interfacial processes. The computed surface tension is increased linearly with concentration of uranyl nitrate up to certain concentration as displayed in Fig.15. The nonlinearity starts appearing at higher concentration of 5.45 mole/liter where a deviation in surface tension is noted from monotonic linear increase. This phenomenon perhaps indicating the super saturation of uranyl nitrate at very high concentration which may drives the formation of crystal. In order to support the simulation findings, dynamic light scattering (DLS) experiment was conducted to explore the behavior of aqueous mixture. The scattering results (Fig. 15) display that homogeneity of solution is maintained up to 4.0 moles/lit and then becomes heterogeneous as the light fails to pass through the solution. The nonlinearity in the intensity curve is appeared at the same location where the nonlinearity in surface tension was observed. Similar deflection in shear viscosity was also observed from 4.5–5.45 mole/lit indicating a possible super saturation phenomena.

Conclusion

The MD simulation studies have been performed in wide range of aqueous and organic mixtures along with pure component to establish the TiAP as a potential ligand and at the same time to develop a single force field which can capture all the properties. The Mulliken charge embedded force field was able to explain all the properties in bulk liquid phase as well as in interface. The present articleconcludes that TiAP might be considered as an alternate of TBP.

Acknowledgements

Corresponding Author*

Sk. Musharaf Ali (musharaf@barc.gov.in)

References

[1]   M. Simpson, and *J.* Law, *Nuclear Fuel Reprocessing. Idaho National Laboratory*, INL/EXT-10-17753,2010.

[2]   S.H. Hassan, J.P. Sukla, *J. Radioanal. Nucl. Chem.*, 2003, **258**, 563 – 573.

[3]   S. Cui, V.F. de Almeida, B. Khomami, *J. Phys. Chem. B,* 2014, **118**, 10750- 10760.

[4]   J. Mu, R. Motokawa, C.D. Williams, K. Akutsu, S. Nishitsuji, and A. Masters, *J. Phy. Chem. B,* 2016, **120**, 5183 – 5193.

[5]   S. Cui, V.F. de Almeida, B.P. Hay, X. Ye, B. Khomami, J. *Phys. Chem. B,* 20, 12, **116**, 305- 313.

[6]   S.W.L. Siu, K. Pluhackova, R.A. Bockmann, *J. Chem. Theory Comput.*, 2012, **8**, 1459- 1470.

[7]   Q.N. Vo, L.X. Dang, M. Nilsson, H.D. Nguyen, *J. Phys. Chem. B*, 2016, **120**, 6985- 6994.

[8]   L. Leay, K. Tucker, A.D. Regno, S.L.M. Schroeder, C.A. Sharrad, A. Masters, *J. Mol. Phys.*, 2014, **112**, 2203–2214.

[9]   W. Allen, and R.L. Rowley, *J. Chem. Phys.*, 1997, **106**, 10273–10281.

[10]   M. Baden, M. Burgard, G. Wipff, *J. Phys. Chem. B,* 2001, **105**, 11131–11141.

[11]   P. Sahu, Sk. M. Ali, K.T. Shenoy, *Chemical product and process modelling* 2017.

[12]   B. Wen, C. Sun, B. Bai, E.Y. Gatapova, O.A. Kabov, *Phys. Chem. Chem. Phys.*, 2017, **19**, 14606–14614.

[13]   R. Biswas, P. Ghosh, T. Banerjee, Sk. M. Ali, K.T. Shenoy, *J. Mol. Liq.* 2017, **241**, 279 – 291.

[14]   M. Jorge, and M.N.D.S. Cordeiro, *J. Phys. Chem. C,* 2007, **111**, 17612 – 17626.

[15]   S. Senapati, and M.L. Berkowitz, *Phys. Rev. Lett.*, 2001, **87**, 176101-1-4.

[16]   P. Guilbaud, and G. Wipff, *J. Mol. Struc.*, 1996, **366**, 55–63.

[17]   S. Kerisit, and C. Liu, *J. Phys. Chem. A,* 2013, **117**, 6421–6432.

[18]   N. Rai, S.P. Tiwari, and E.J. Maginn, *J. Phys. Chem. B,* 2012, **116**, 10885–10897.

[19]   M.P. Allen, D.J. Tildesley, *Computer Simulation of Liquids,* 2017: Clarendon Press, Oxford University.

[20]   A. D. Becke, *Phys. Rev. A,* 1988, **38**, 3098-3100.

[21]   TURBOMOLE V6.6. a development of University of Karlsruhe and Forschungszentrum Karlsruhe GmbH, 1989- 2007, TURBOMOLE GmbH, since 2007.

[22]   M.F. Guest, I.J. Bush, H.J.J. Van Dam, P. Sherwood, J.M.H. Thomas, J.H. Van Lenthe, *Mol. Phys.*, 2007, **103**, 719-747.

[23]   J. Mark, M.J. Abraham, J.E. Gready, *J. Comput. Chem.*, 2011, **32**, 2031 – 2040.

[24]   A.P. Sunda, and A. Venkatnathan, *Mol. Simu.*, 2013, 1 – 6.

[25]   T. Straatsma, H., Berendsen, *J. Chem. Phys.*, 1988, **89**, 5876–5886.

[26]   A. Das, P. Sahu, Sk. M. Ali, *J. Chem. Eng. Data,* 2017, **62**, 2280 – 2295.

[27]   A. Das, and Sk. M. Ali, *J. Chem Phys.*, 2018, **148**, 074502-1-14.

[28]   G. Peskir, *Stoch. Model* s, 2003, **19**, 383–405.

[29]   B. Hess, *J. Chem. Phys.*, 2002, **116**, 209 – 217.

[30]   Das, A. and Ali, Sk. M., *J. Mol. Liq.*, 2019, **277**, 217–232.

[31]   M.L. Singh, S.C.Tripathi, M. Lokhande, P.M. Gandhi, and V. G. Gaikar, J. Chem. Eng. Data, 2014, **59**, 1130 – 1139.

[32]   F. Buff, R. Lovett, F. Stillinger, *Phys. Rev. Lett.*, 1965, **15**, 621 – 623.

[33]   A. Das, Sk. M. Ali, *J. Phys. Chem. B,* 2019, **123**, 4571- 4586.

[34]   C. D'Agostino, R.C. Harris, A.P. Abbott, L.F. Gladden, M.D. Mantle, *Phys. Chem. Chem. Phys.*, 2011, **13**, 21383- 21391.

[35]   R. Walser, A.E. Mark, W.F. van Gunsteren, *Chem. Phys. Lett.*, 1999, **303**, 583–586.

[36]   P. Banerjee, S. Yashonath, B. Bagchi, *J. Chem. Phys.* 2017, **146**, 164502.

[37]   J.P. Hansen, I.R. McDonald, *Theory of Simple Liquids* (Academic Press, NewYork, 1986).

Permeation and Desalination of Salt Water through Nanomembrane

Pooja Sahu[1,2], *Sk. Musharaf Ali[1,2]

[1]Chemical Engineering Division, Bhabha Atomic Research Centre, Mumbai-400085, India
[2]Homi Bhabha National Institute, Mumbai-400094, India

ABSTRACT

The nanoscopic assessment of various molecular events for nanotube and graphene based desalination are carried out by extensive molecular dynamics simulations. The understanding of driving forces associated to the filling of nanotubes with polar and non-polar fluids are explored. The coupling of transport coefficients with the thermodynamic entropy is provided in terms of universal scaling relation, which might be of great scientific and technological importance to the process endured with the phase transition like crystallization, nucleation and glass transition. The trend for water permeability and salt rejection with increasing pressure gradient, pore size and ion concentration are presented. The ultrafast fluidic nature for these membranes is captured from the breakdown of continuum model under nanoscale confinement which is reflected from the layered flow and plug like velocity profiles. The results revealed that the membranes comprising nanotubes of 1.0-1.1nm and graphene with width of h=7Å show a great potential due to higher water permeability than TFC membrane.

Keywords: Seawater, Desalination, Diffusion, Permeation, Graphene nanomembrane, MD simulations.

Introduction

Continuously increasing population, abnormal climate changes and rapid industrialization have intensified the problem of neat and clean potable water[1]. Even though nearly 71% of the earth crust is occupied by water, however, only 3% of this is fresh and suitable for human consumption. Many of the added impurities to these water sources by human beings and industries are non-biodegradable, and so are threatening not only to aquatic life but also if added to food-chain impose risk to human health[2]. One way to tackle this problem and increase the availability of drinking water is by treating the contaminated effluents to eradicate the impurities. Though the traditional methods such as ion exchange[3], chemical precipitation[4], solvent extraction and adsorption process[5] are widely used to remove the impurities from the contaminated water, however, their use at large scale is limited due to high operational cost, low permeate flux and inapplicability to handle effluents with low concentration of metal ions. Nowadays, the most widely adopted commercial desalination techniques are electrodialysis, nanofiltration[6] and reverse osmosis (RO)[7]. In RO method, water is forced through a semi-permeable membrane, that blocks the passage of solutes and only water is allowed to pass through. However, a significant energy input is needed for this process to pressurize the feed water above osmotic pressure so that the useful flux can be obtained. Although ROs are believed to be of greatest practical potential, the water permeability is still not satisfactory. Also, the energy and capital consumption are quite intensive. However, since the energy cost of the RO process depends on the nature of solute to be filtered and the characteristics of membrane being used, the raised issue can be managed by selecting the appropriate membrane for the process[8]. At present, thin-film composites (TFCs) are the most common membranes being used in this process[9]. These are polysulfone or polyethersulfone membranes coated with polyamide layer, which provide them narrow, tortuous but continuous pores. These pores are suitable for flow of water but reject the salt ions. TFC membranes provide high salt rejection efficiency but suffer with the problem of low water permeability. After the implausible studies of Hummer *et al.*[10] for ultrafast water transport through CNT(6,6), a particular interest has been focused on nanotube based membranes[11, 12]. Due to large surface to volume ratio and excellent thermal, chemical and mechanical properties, nanotubes have attracted a broad interest for membrane applications[13, 14]. The experimental studies by Hind *et al.*[15] and Holt *et al.*[16] showed the extraordinary fast water transport through smaller diameter double walled CNT membranes, which was also revalidated by Joseph *et al.*[17] using MD simulations. However, later on, Thomas *et al.*[18] reported much smaller enhancement in water transport through these nanotubes compared to what was reported by Holt *et al.*[16]. Subsequently, the studies by Naguib *et al.*[19] as well as Major *et al.*[20] showed that the increment in flow decreases with increase in nanotube diameter. Also, Su *et al.*[21] reported the exponential relationship between water flux and nanotube length/diameter. To be noted, the filling of nanotubes is surprising as the nanotube like hydrophobic confinement are generally supposed to decrease both the entropy and enthalpy due to breakage of water-water hydrogen bond (HB) network while entering in the nanotube confinement. In spite of unfavourable energies, the water molecules not only spontaneously fill up the nanotube but also contribute to enhanced conduction rate, exceeding the hydrodynamic predictions of Hagen-Poiseuille[10, 16]. The filling and emptying transitions in hydrophobic channels have been explained by many authors using different analytical, quantum, and molecular dynamics calculations[22-24]. However, as far as thermodynamic criteria are concerned, there are contradictory views on whether the spontaneous filling of nanotubes is driven by the entropy or energy transfer. Vaitheeswaran *et al.*[25] reported the

zero entropy of transfer from bulk into a quasi-infinite nanotube channels using statistical mechanical framework. Pascal *et al.*[23] as well as Kumar *et al.*[24] explained that the water entry inside CNTs is favoured by entropy but unfavored by enthalpy. The translational entropy of water transfer inside CNT(6,6) was reported to increase by Pascal *et al.*[23], but was shown to be reduced by Kumar *et al* [24]. Such contradictions require additional studies in order to arrive at a reasonable conclusions. Since the increase in translational entropy of confined water is expected to arise from the tetrahedral liberation of bulk water and therefore might be expected to be unique to water, and so the question, whether enhancement in translational entropy is really unique to water remains open both from the experimental tests and simulation studies. In addition, only scarce studies are available on the structural and transport properties of other polar and nonpolar fluids for nanotube confinement, which need to be explored.

Considering the potential applicability of nanotube membranes, it is important to explore the mechanism involved in ultrafast fluid-transport, and frictionless flow through nanotubes. Also, a precise assessment of nanotubes is necessary before selecting them as a potential candidate for future desalination. However, since the fabrication methodologies of nanotubes are yet to be simplified, the computational studies become main source for directing this field. Also, high-fidelity molecular simulations provide a better understanding of the process from microscopic point of view[26]. In this regard, the molecular dynamics simulations[27] have been used to understand the associated mechanism of fluid transport through nanochannels membranes. Extensive MD simulations using LAMMPS[26] and GROMACS[28] package were conducted. The sp^2 carbon atoms of the CNTs has been modelled as Lennard-Jones particle with size and energy parameters as σ_{cc} =3.4Å and σ_{cc} = 0.36kJ/mol respectively. The long range electrostatic interactions between atoms and molecules were determined using Ewald method[29] and the short range interactions are incorporated with L-J potential. For water SPC potential[30] and for other fluids OPLS force field parameters[31] are used. The thermodynamic parameters in this study have been estimated using very efficient and robust two phase thermodynamic (2PT) method[32,33]. The simulation systems were equilibrated for 50ns, followed by 20ns of production run. Further, the coordinates and velocities were saved after each 4fs for calculation of dynamical parameters and ~500fs for structural one. MD trajectories were visualized by VMD package[34].

Results and discussion

Fluid transport through CNT(6,6)

The internal space wetting of hydrophobic CNT(6,6) with water (@300K) and methane (@136K) results from favourable free energies inside the CNT as shown in Table 1.

Table 1 Entropy, energy, and free energy gain (in unit J/mol-K) for confined water and methane.

CNT (6,6)	ΔS	$T\Delta S$	ΔE	ΔA
Water	17 .63	5.29	3.18	-2.11
Methane	22 .23	2.84	2.75	-0.09

The free energy of confined fluid is primarily favoured by increased translational and rotational entropies but largely by increased rotational entropy (Table 2). Our results explain that, yes, the nano confinement favours the translational entropy of transfer

Table 2. Entropy components (J/mol-K) and density (g/cm^3) of water (H$_2$O) and methane (CH$_4$).

System	S $_{trans}$	S $_{rot}$	S $_{total}$	density
bulk H$_2$O	51.46	14.96	66.42	0.981
bulk CH$_4$	49.55	30.03	79.58	0.427
H$_2$O in CNT	56.12	27.93	84.05	
CH$_4$ in CNT	51.55	48.48	100.43	

from bulk solution to CNT and the gain in translation entropy is not unique to water like H bonding fluid but is also observed for nonpolar methane. As shown in Fig.1, the water molecules inside CNT were found in ordered structure but in zig-zag orientation to form the H bond with their neighbours. Interestingly, the methane molecules inside CNT were also found in ordered structure, irrespective of their inability to form H bond as shown in Fig.1. In fact, the single file arrangement of water and methane in CNT(6,6), leads to higher diffusion than conventional confinement. The results demonstrate that though H-bonding plays an important role in conduction, it is not the only driving factor, as the nonpolar fluids, which do not have any H bond can not only go inside CNT but also flow through it. The associated driving forces for filling and transport of fluid are due to enhanced translational and rotational entropies, which are credited by strong correlation among confined fluid molecules (increased translational entropy) and availability of more free space for rotation of molecules (enhanced rotational entropy)[35].
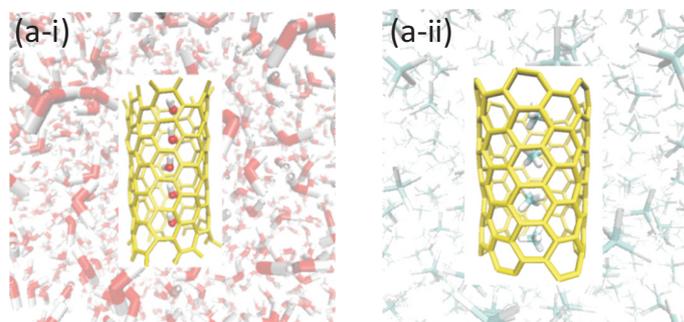
Fig.1: Snapshot of (a-i) water and (a-ii) methane molecules inside CNT(6,6).

Effect of CNT termination and polarization

Here, the effect of nanotube charge and CNT end termination was explored by studying the water structure, dynamics and thermodynamics through unterminated, terminated neutral and terminated-charged CNT(6,6) as shown in Fig.2(a). Hydrogenated pores were obtained by functionalizing edge carbon atoms of CNT with hydrogen atoms of size and energy parameter as σ_{HH} = 2.5 Å, ε_{HH} = 0.1255 kJ/mol. The atomic charges for CNT atoms were determined by performing ab initio quantum[36] calculations at the B3LYP/TZ2P[36] level of theory using ADF package[37]. Fig.2(b) reveals that the magnitude of partial charges at nanotube ends is much greater than the middle region. The dissimilarities in entropic components as reported in Table 3 were found to be correlated with various dynamical and structural parameters.
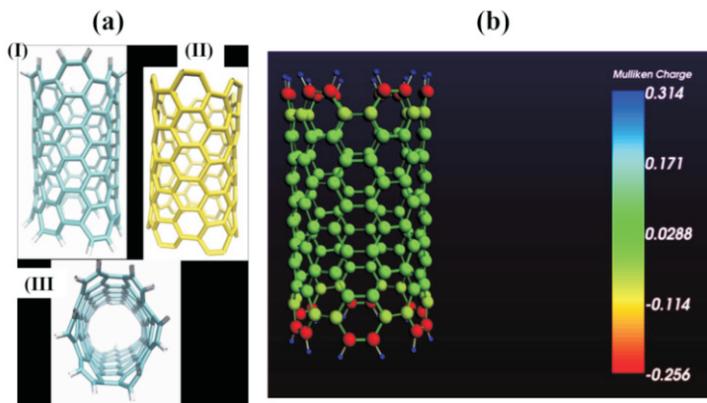
Fig.2: (a) Structure of CNTs: I and II. front view of H terminated and unterminated and III. top view of H terminated CNT (b) Partial charge distribution for H terminated CNT.

Fig.2(b) reveals that the magnitude of partial charges at nanotube ends is much greater than the middle region. The dissimilarities in entropic components as reported in Table 3 were found to be correlated with various dynamical and structural parameters. The rotational entropies are well corroborated with hydrogen bond (HB) correlation functions. Results revealed that the HBs of CNT confined water molecules show long preserving correlation if their rotations inside CNT are restricted by nanotube polarization. A relation between translational diffusivity and configurational entropy for water in bulk to CNTs is framed. The observed effects are too small to be realized in practical applications[38].

Table 3 Entropy components for bulk water and water confined in various CNTs.

System	S_{trans}	S_{rot}	S_{total}
bulk H_2O	51.46 (± 0.25)	14.96 (± 0.06)	66.42
un	56.12 (± 0.20)	27.93 (± 0.01)	84.06
tn	56.97 (± 0.15)	31.45 (± 0.15)	88.42
tc	57.63 (± 0.17)	25.20 (± 0.19)	82.83

Flow transition with nanotube diameter

The flow transition from sub-continuum to continuum regime was captured for water, methanol and methane with increasing nanotube diameter as displayed in Fig.3. The results show that the single file flow of fluid inside CNT is diminished with increase in tube diameter and renewed to layered flow for larger CNTs[39]. Such a transition was further described in terms of diffusion coefficient and density of states (DOS)[39]. The observations from DOS (Fig.4) was in good agreement with the corresponding velocity auto correlation function and diffusion dynamics[40, 41].

Relation between diffusivity and entropy

Furthermore, we established a scaling relation for liquids in bulk and confined states. Since, it is very difficult to estimate the accurate diffusivity of fluids confined in CNT like one dimensional geometry from the experiments, linking them with the experimentally
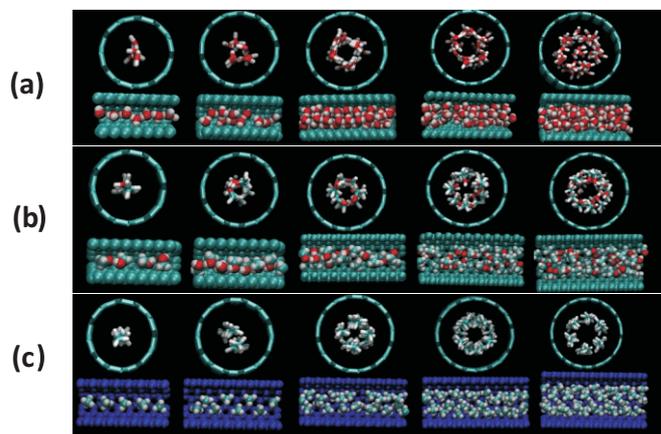
Fig.3: Snapshot of (a) water (b) methanol and (c) liquid methane inside CNT(6,6), CNT(7,7), CNT(8,8), CNT(9,9) and CNT(10,10) respectively.
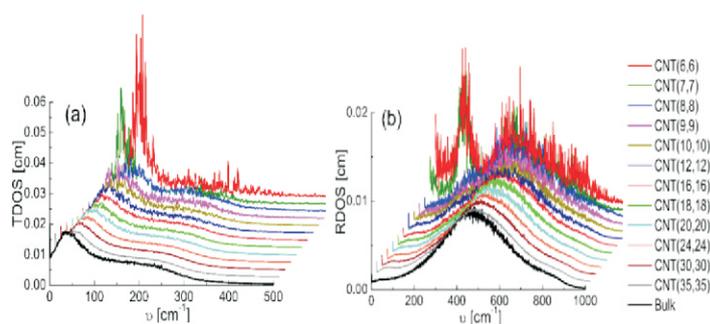
Fig.4: (a) Translational DOS (b) Rotational DOS for water in CNT confinement.

accessible thermodynamic quantities would be a great scientific and technological benefits.

Our results demonstrate persuasively that there exists a universal scaling relation between scaled diffusivity D* and excess entropy S_{ex} for molecular fluids. However, D* for molecular fluids (Dm*) differs from Dzugutov D* by the scaling factor α, which depends on structural correlation and the reduced density of molecular systems as shown by Eqns. 1 to 3.

$$D^* = A\left[\exp\left(B.S_{ex}\right)\right] \tag{1}$$

Where D* is the scaled diffusivity, $D^* = D\Gamma^{-1}\sigma^{-2}$ with σ is the hard sphere diameter and Γ as Enskog collision frequency,

$$\Gamma = 4\sigma^2 g(\sigma)\rho\left(\frac{\pi k_B T}{m}\right)^{1/2} \tag{2}$$

In this expression, m and ρ represent the molecular mass and density of the system respectively. The quantity σ is determined from position of first peak in pair correlation function and g(σ) is the value of pair correlation function at σ. D* for molecular fluids (Dm*) differs from Dzugutov D* by the scaling factor α

$$D_m^* = \alpha.D^*_{Dzugutov} \tag{3}$$
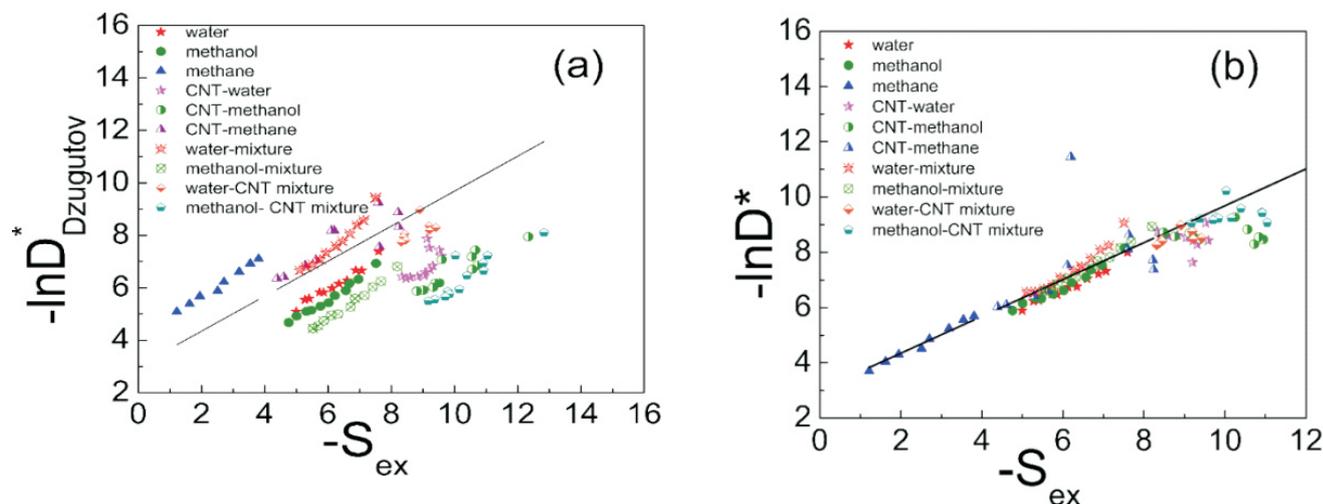
Fig.5: Scaling relation for D* and S_{ex} with (a) Dzugutov equation (b) Modified relation of Dm* and S_{ex}.

Where $\alpha = \left(\lambda . C \left(\dfrac{g(\sigma)}{\rho * \sigma} \right) \right)$. λ and C are constants:

(i) If $\eta < 0.45$; $\lambda = 0.4$ and C = 1 for pure, C = ½ for mixture and C=1/7 for CNT confinement.

(ii) If $\eta > 0.45$; $\lambda = 7.2$ and C = 1 for pure, C = 1/10 for mixture and C= 2/7 for CNT confinement. η is the packing fraction, given by

$$\eta = \frac{\pi}{6} \rho^*$$

Interestingly, the simulation results of liquid argon indicate that α reduces to one for atomic fluids. In other words, the proposed scaling equation represents Dzugutov relation in the limiting conditions where strong intra-molecular interactions can be waved off. The proposed scaling relation (Fig.5) covers the diverse set of hydrogen bonding fluids both in bulk and mixed state. Moreover, it has been shown that the validity of the proposed relation is not limited to the domain of conventional fluids but also can be reasonably used for CNT confinement. The results demonstrate that the connection between self-diffusivity and excess entropy is nearly universal for varieties of molecular liquids, liquid mixtures and liquids under nano-confinement if the structural effects caused by strong intramolecular and intermolecular interactions are taken care by $g(\sigma)$ i.e. confinement by first shell of neighbour atoms and reduced density ρ^* in the scaling factor α.[42] Applicability of the relation for CNT confinement manifest the transferability of proposed scaling equation from cage diffusion to molecular hopping like special diffusion mechanism[42].

Nanoscopic assessment filtration in CNT

Subsequently, the nanoscopic view of desalination through CNT membranes using MD simulations has been explored. The graphene terminated CNTs were used to represent the part of nanotube membrane as shown in Fig.6.

The trend for water permeability and salt rejection with increasing pressure gradient, nanotube diameter and salt concentration was evaluated and results are shown in Fig.7. Results reveal that the membranes comprising nanotubes of 1.0–1.1 nm diameter can be used for efficient water desalination with more than 95% salt rejection. The average permeability of water was estimated to be 10^{-3} moles/cm^2-sec-MPa, two order higher than TFC membranes.

Further, the water flux anomalies in CNT were found to be linked with the hydration characteristics of ions inside CNTs. It was noticed that akin to bulk phases, the mass transport through CNT can be linked with the diffusivity of component species[43]. It was seen that not only the diffusivities of water and ions, but also the
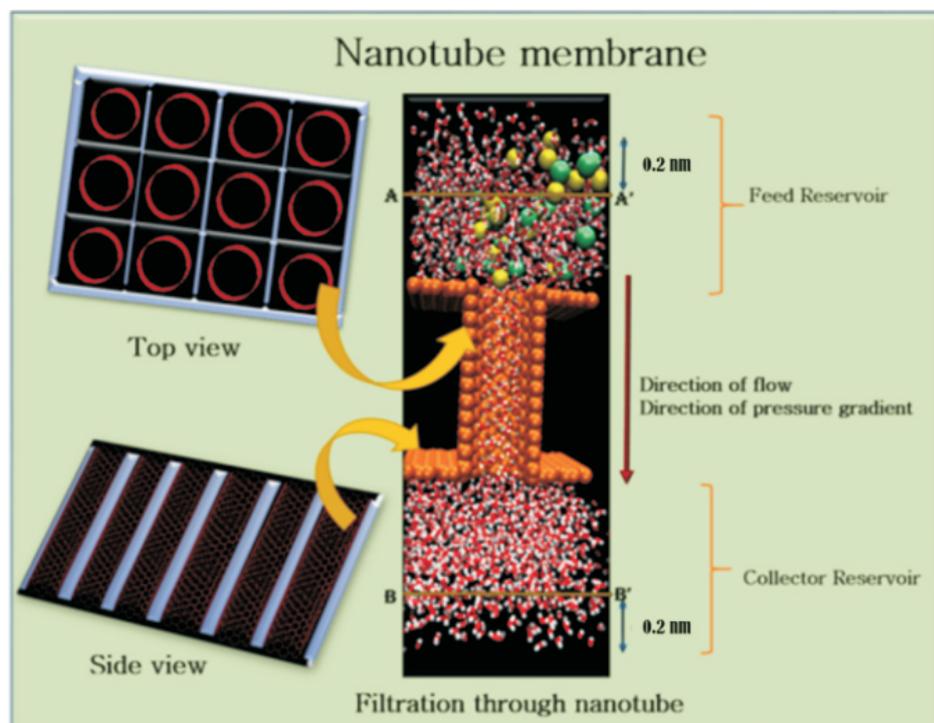
Fig.6: Schematic diagram of CNT membrane (green: Cl⁻, yellow: Na⁺, red and white represents O and H atoms of water, CNT shown by orange).
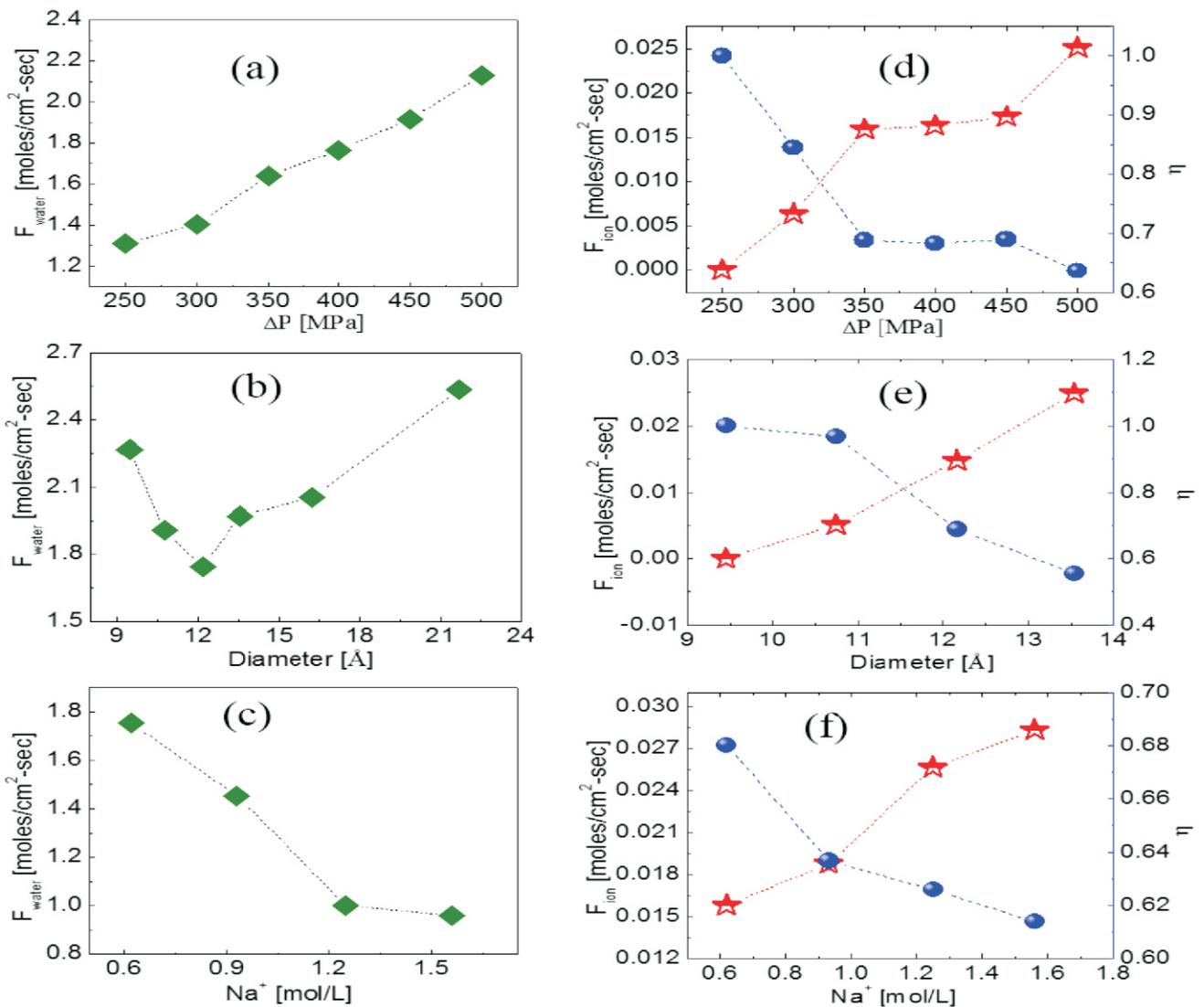
Fig.7: (a, b, c) flux of water F_{water} and (d, e, f) flux of ions F_{ion} (unit moles/cm^2-sec) (left Y-axis) and salt rejection efficiency η (right Y-axis) as an effect of (a, d) pressure gradient (b,e) nanotube diameter and (c, f) feed concentration.

ratio of diffusivity D_{water}/D_{ion} can be linked with the respective water to ion flux ratio and the salt rejection trends[43].

Nanoscopic filtration in graphene

Further, in quest of identifying an inexpensive and easily scalable material with graphene like fluidic properties, the fluid transport through graphene membranes was investigated. The graphene membranes were made by tailoring of graphene sheets as shown in Fig.8. Results showed increasing water flux with increase in pore size, on the other hand, reducing water flux with increase in salt concentration. It was observed that no ion could pass through the membrane for h ≤ 7Å, indicating 100% salt rejection with pores of 5Å-7Å. However, it was reduced to 91.67% for h =8Å and 33.33% for h=9Å (Fig.9). The water permeability through the graphene channel (h=7Å) is two orders of magnitude higher than TFC membrane. The breaking of continuum assumption in graphene nanopores was captured by the appearance of a layered water structure and plug-like velocity profiles[44].

The fluidity under nano confinement of graphene was examined in terms of shear viscosity, friction coefficient and slip length. The calculated viscosity and diffusion coefficient under the graphene pores did not follow the Stokes–Einstein relation, indicating the failure of the hydrodynamic theory. The confined state of water in the graphene pores was also explored via the translational density of states and entropy, which displayed a significant change in the
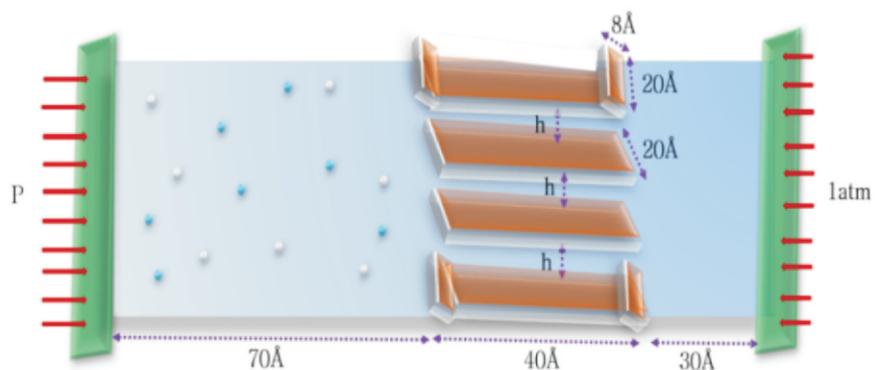
Fig.8: Schematic graphene membrane.
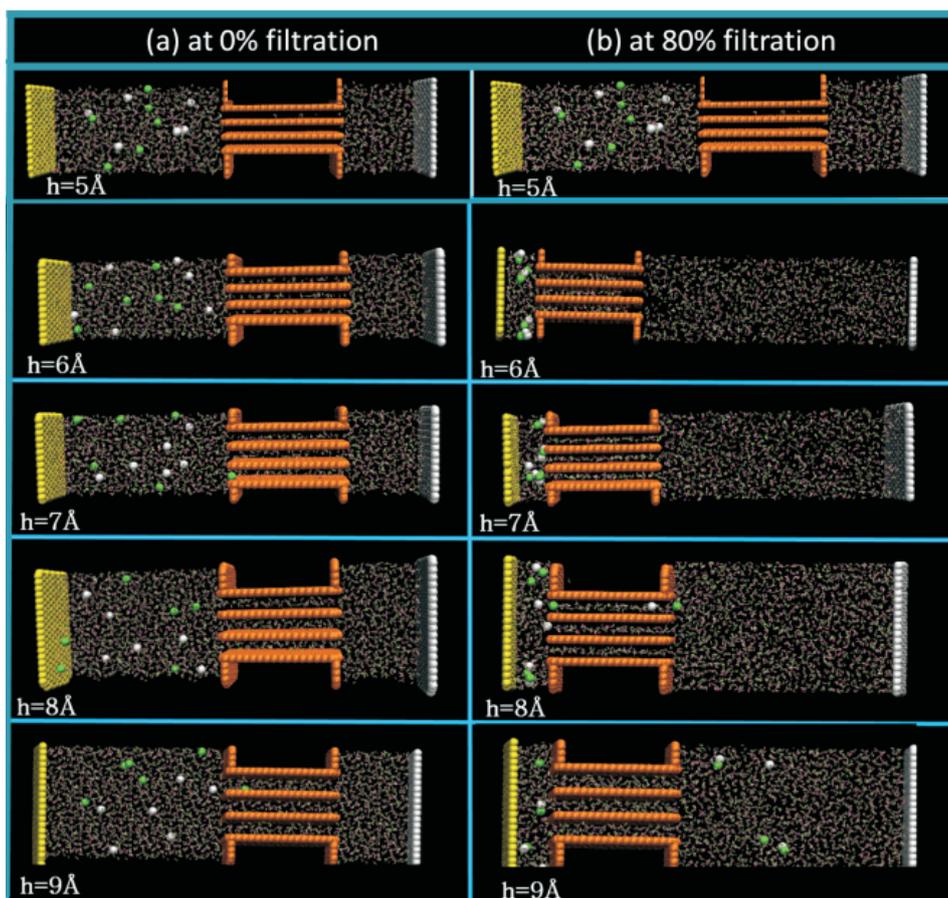
Fig.9: Snapshot for water filtration through graphene membrane with different width h =5-9Å taken at (a) t=0ns and (b) when 80% water has filtered from feed reservoir [C=0.2M, P=150 Mpa].

translational entropy with change in the pore size and applied pressure and thus revealed the interconnectivity of the structure[44].

Conclusions

The results show that the wetting of the internal space of nanotubes with polar and nonpolar fluids results from the favourable free energy of confinement. The free energy of confined fluid is primarily favoured by increased entropy. The MD results suggest that the uneven membrane is beneficial. The proposed new scaling relations can be applied successfully for all the liquids and liquid mixtures in bulk and CNT confinement to capture the quantitative relationship of self-diffusion coefficient and excess entropy. The work concludes that the membranes comprising nanotubes of 1.0–1.1 nm diameter and graphene membranes of width h=7Å show a great potential to be used in RO, as water permeability is much higher than TFC membrane. Overall, the understanding of fluid transport through nanotubes by MD simulations was fruitfully achieved. Linking of mass flux with diffusion and linking of diffusion with the experimentally accessible thermodynamic parameter entropy can be of great importance in various fields of science and technology. Also, the presented microscopic understandings might be helpful in examining the performance of other nano-membranes as well as biological channels.

Acknowledgement

Corresponding Author*

Sk. Musharaf Ali (musharaf@barc.gov.in)

References

[1]   United Nations World Water Assessment Programme, The world water development report, Paris, France: UNESCO, 2014.

[2]   T. Masciangioli and W.X. Zhang, *Environ. Sci. Technol.*, 2003, 102A–108A.

[3]   A. Da browski, D.Z. Hubicki, P. Podkościelny and E. Robens, *Chemosphere*, 2004, **56**, 91-106.

[4]   M.T. Alvarez, C. Crespo and B. Mattiasson, *Chemosphere*, 2007, **66**, 1677- 1683.

[5]   P.A. Brown, S.A. Gill and S.J. Allen, *Water Res 34*, 2000, **16**, 3907–3916.

[6]   M. Whitby, L. Cagnon, M. Thanou and N. Quirke, *Nano Lett.*, 2008, **8**, 2632-2637.

[7]   S.T. Oyama and S.M. Stagg-Williams, Inorganic, polymeric and composite membranes, Elsevier, Amsterdam, The Netherlands, 2011.

[8]   K. Takeuchi, Y. Takizawa, H. Kitazawa, M. Fujii, K. Hosaka, J. Ortiz-Medina, A. Morelos-Gómez, R. Cruz-Silva, M. Fujishige, N. Akuzawa and M. Endo, *Desalination,* 2018, **443**, 165-171.

[9] M. Thomas and B. Corry, *Phil. Trans. R. Soc. A*, 2016, **374**, 20150020-20150020.

[10] G. Hummer, J.C. Rasaiah and J.P. Noworyta, *Nature*, 2001, **414**, 188-190.

[11] Z.E. Hughes, C.J. Shearer, J. Shapter and J.D. Gale, J. *Phys. Chem. C*, 2012, **116**, 24943-24953.

[12] M. Majumder, N. Chopra and B. J. Hinds, *ACS Nano*, 2011, **5**, 3867–3877.

[13] W. Zhang, P. Sherrell, A.I. Minett, J.M. Razal and J. Chen, *Energy Environ. Sci.*, 2010, **3**, 1286-1293.

[14] J. Sengupta, in *Handbook of Nanomaterials for Industrial Applications: Micro and Nano Technologies*, 2018, pp. 172-194.

[15] B.J. Hinds, N. Chopra, T. Rantell, R. Andrews, V. Gavalas and L. G. Bachas, *Science*, 2004, **303**, 62-65.

[16] J.K. Holt, H.G. Park, Y. Wang, M. Stadermann, A.B. Artyukhin, C.P. Grigoropoulos, A. Noy and O. Bakajin, *Science*, 2006, **312**, 1034-1037.

[17] P. Joseph, C. Cottin-Bizonne, J.-M. Benoıt, C. Ybert, C. Journet, P. Tabeling and L. Bocque, *Phys. Rev. Lett.*, 2006, **97**, 156104-156104.

[18] J.A. Thomas and A.J.H. McGaughey, *Nano Lett.*, 2008, **8**, 2788-2793.

[19] N. Naguib, H. Ye, Y. Gogotsi, A.G. Yazicioglu, C.M. Megaridis and M. Yoshimura, *Nano Lett.*, 2004, **4**, 2237-2243.

[20] R.C. Major, J.E. Houston, M.J. McGrath, J.I. Siepmann and X.Y. Zhu, *Phys. Rev. Lett.*, 2006, **96**, 177803-177804.

[21] J. Su and H. Guo, *J. Phys. Chem. B*, 2012, **116**, 5925-5932.

[22] A. Waghe, J.C. Rasaiah and G. Hummer, *J. Chem. Phys.*, 2002, **117**, 10789-10795.

[23] T.A. Pascal, W.A. Goddard and Y. Jung, *Proc. Natl. Acad. Sci. U.S.A.*, 2011, **108**, 11794-11798.

[24] H. Kumar, B. Mukherjee, S.T. Lin, C. Dasgupta, A.K. Sood and P.K. Maiti, *J. Chem. Phys.*, 2011, **134**, 124105-124108.

[25] S. Vaitheeswaran, J.C. Rasaiah and G. Hummer, *J. Chem. Phys.*, 2004, **121**, 7955-7965.

[26] S. Plimpton, *J. Comput. Phys.*, 1995, **117**, 1-19.

[27] D. Frenkel and B. Smit, Understanding molecular simulation: from algorithms to applications, Academic press., Elsevier, United States, 2001.

[28] S. Pronk, R. Schulz, P. Larsson, P. r. Bjelkmar, R. Apostolov, M.R. Shirts, J.C. Smith, P.M. Kasson, D. v. d. Spoel, B. Hess and E. Lindahl, *Bioinformatics*, 2013, **29**, 845-854.

[29] T. Darden, D. York and L. Pedersen, *J. Chem. Phys.*, 1993, **98**, 10089-10092.

[30] H.J.C. Berendsen, J.R. Grigera and T.P. Straatsma, *J. Phys. Chem.*, 1987, **91**, 6269-6271.

[31] W.D. Cornell, P. Cieplak, C.I. Bayly, I.R. Gould, K.M. Merz, J. Ferguson, D.M.,D.C. Spellmeyer, T. Fox, J. W. Caldwell and P.A.A. Kollman, *J. Am. Chem. Soc.* , 1995, **117**, 5179-5197.

[32] S.-T. Lin, M. Blanco and W.A. Goddard, *J. Chem. Phys.*, 2003, **119**, 11792-11805.

[33] S.-T. Lin, P.K. Maiti and W.A. Goddard, *J. Phys. Chem. B*, 2010, **114**, 8191-8198.

[34] W. Humphrey, A. Dalke and K. Schulten, *J. Mol. Graphics*, 1996, **14**, 33-38.

[35] P. Sahu, S.M. Ali and K.T. Shenoy, *J. Chem. Phys.*, 2015, **142**, 074501-074511.

[36] G.Y. Guo and J.C. Lin, *Phys. Rev. B*, 2005, **71**, 165402-165412.

[37] G.t. Velde, F.M. Bickelhaupt, E.J. Baerends, C.F. Guerra, S. J.A.v. Gisbergen, J.G. Snijders and T. Ziegler, *J. Comput. Chem.*, 2001, **22**, 931-967.

[38] P. Sahu and S.M. Ali, *J. Chem. Phys.*, 2015, **143**, 184503-184514.

[39] P. Sahu, S.M. Ali and K.T. Shenoy, *AIP Conf. Proc.*, 2016, **1731**, 110050-110053.

[40] P. Sahu and S. M. Ali, *J. Chem. Eng. Data*, 2017, **62**, 2307-2315.

[41] P. Sahu and S.M. Ali, *Int J Quantum Chem.*, 2017, e25578.

[42] P. Sahu, S.M. Ali and K.T. Shenoy, *J. Phys. Chem. C,* 2017, **121**, 11968- 11974.

[43] P. Sahu, S.M. Ali, K.T. Shenoy and S. Mohan, *Phys. Chem. Chem. Phys.*, 2019, **21**, 8529-8542.

[44] P. Sahu, S.M. Ali, K.T. Shenoy and S. Mohan, *Phys. Chem. Chem. Phys.*, 2019, **21**, 21389–21406.

Thermo-physical and Diffusional Properties of Uranium-Neptunium and Thorium-Neptunium Mixed Oxides

P.S. Ghosh and A.K. Arya*
Glass and Advanced Materials Division
Bhabha Atomic Research Centre, Mumbai-400085, India

ABSTRACT

Burn-up of $(U,Pu)O_2$ mixed oxide (MOX) fuels generate additional long-lived minor actinides (MAs) in the yield range 0.1-1.0%. The Np and other MAs are a major concern for the storage of spent fuels due to their long-term radiotoxicity and heat generation in the spent fuel. The burn-up of ThO_2-based MOX generates $(Th,U,MA)O_2$ and/or $(Th,Pu,MA)O_2$ MOX which may alter the thermal properties of the fuel. Experimental determination of thermo-physical and diffusional properties of these MOX is difficult due to their radio-toxicity. A multi-pronged atomistic simulation approach consisting of (a) first-principles density functional theory for evaluation of ground state stability, complex magnetic interactions, defect formation energies and elastic properties, (b) Monte-Carlo based approach to exactly model disordered alloys and (c) molecular dynamics calculations for evaluation of diffusional and thermal properties of $U_{1-x}Np_xO_2$ and $Th_{1-x}Np_xO_2$ MOX has been employed. The generation of thermo-physical and diffusional properties database of Np-containing MOX will help design and fabrication of new fuels and perform safety analysis.

Keywords: Thermo-physical parameters, Diffusion, MOX fuel, Atomistic simulations, DFT, Monte-Carlo.

Introduction

Neptunium (^{237}Np, half life = 2.14 x 10^6 years), is formed in nuclear fuels as a byproduct, either by α decay of ^{241}Am or by the (n,γ) reaction of ^{235}U followed by β emission. In reactors utilizing $U_{1-x}Pu_xO_2$ mixed oxides (MOX) fuel; NpO_{2-x} is generated predominantly along with other minor actinides (MA's) (with a yield of 0.1-1.0%) and gets accumulated due to its long half-life. Moreover, it is an important nuclide for geological disposal of spent fuel generated from open fuel cycle reactor operation, where the spent fuel is stored for the long term. For reactors operating in a closed fuel-cycle mode, spent fuels are reprocessed chemically to isolate MA's, which are reused for energy production in fast reactors as $U_{1-x-y}Pu_xMA_yO_2$ MOX. As a result, MA's can be transmuted into less radiotoxic and lighter isotopes, which reduce the long-term radiotoxic impact of these materials. The transmutation of MA's in fast reactors can be performed in homogeneous (2-6 wt.% MAs, homogeneously added to fuel) and heterogeneous modes (10-30 wt.% MAs is added to transmutation targets) [1-5]. Additionally, ThO_2 based MOX ($Th_{1-x}U_xO_2$ and $Th_{1-x}Pu_xO_2$) has emerged as an alternate high performance fuel with additional advantages of lower radiotoxic nuclear waste generation and easy management and storage of long-lived highly radioactive nuclides, compared to conventional UO_2 based MOX [1-14]. $Th_{1-x}MA_xO_2$ MOX can be formed in a nuclear reactor from the transmutations of $Th_{1-x}U_xO_2$ and $Th_{1-x}Pu_xO_2$ MOX. Hence, a better understanding of $U_{1-x}Np_xO_2$ and $Th_{1-x}Np_xO_2$ pseudo-binary phase diagrams, including thermodynamic and electronic properties, is highly desirable in order to assess the phase stability of these materials.

Under irradiation, a large number of point defects are produced and many of these point defects recombine instantly during the cascade processes at elevated temperature [15]. In MOX fuels, the production and migration of oxygen vacancies and interstitials are of primary interest because their mobility plays an important role in the micro-structural evolution and the diffusion-controlled formation of defect clusters, bubbles, dislocation loops, and the restructuring of fuels [15-17]. Therefore, it is important to increase our understanding of thermal and diffusional properties of MAO_2, $(U,Pu,MA)O_2$ and $(Th,U,Pu,MA)O_2$ MOXs at high temperatures. This will contribute to better transmutation fuel fabrication and to the prediction of fuel behavior under irradiation and thus leads to improve fuel performance. In this regard, NpO_2 based MOX, is specifically important because of its high yield during the burn-up of fuels. The effect of the addition of MAs in MOX on thermal and diffusional properties has been studied relatively rarely by experimental means because of the radio-toxicity involved in these materials. Even though, the experiments were performed it was limited to specific compositions of MAO_2 and temperature ranges over which the properties were measured. The evaluation of thermal and diffusional properties using atomistic simulations can provide fundamental insights at a level not achievable through experiment alone [7-19]. Present study adopts quantum and classical mechanical based simulation strategies to determine thermodynamical, thermo-physical and diffusional properties of $U_{1-x}Np_xO_2$ and $Th_{1-x}Np_xO_2$ MOX. Firstly, ground state formation enthalpies of $U_{1-x}Np_xO_2$ and $Th_{1-x}Np_xO_2$ MOX accounting for their magnetic configurations are calculated using density functional theory (DFT) based simulations. Further, electronic structures and elastic properties of pure oxides and MOX are calculated. The special quasi-random structures (SQS) approach and *U*-ramping method are used to overcome difficulties related to the modeling of random alloys and to achieve the correct ground state, respectively. Secondly, the thermal expansion, thermal conductivity and diffusion properties of $U_{1-x}Np_xO_2$ and $Th_{1-x}Np_xO_2$ MOX are studied in the 300-2000 K temperature range using static and molecular

dynamical (MD) simulations with classical empirical potentials as a first step towards the investigation of more complex $(U,Pu,Np)O_2$ and $(Th,U,Pu,Np)O_2$ MOX fuels.

2. Computational Methodology

In order to calculate the formation energies and the electronic structures of $U_{1-x}Np_xO_2$ and $Th_{1-x}Np_xO_2$ MOX, *ab initio* total energy calculations are carried out using spin polarised mode of density functional theory (DFT) as implemented in the VASP package. The standard projected augmented wave (PAW) potentials and a plane-wave basis set with a cut off value of 500 eV were used in all cases. The exchange-correlation term was modelled using the generalized gradient approximation (GGA), parameterized by Perdew, Burke and Ernzerhof (PBE). To describe the behaviour of the localised *f* states in Th, U and Np, we included the orbital-dependent Coulomb potential (Hubbard *U*) and the exchange parameter *J*, as formulated by Liechtenstein *et al.* In our calculations *U*=4.5 and *J* =0.5 eV was used as suggested by Kotani *et al.* based on their X-ray photoemission spectroscopic (XPS) analysis of UO_2. The DFT+*U* calculation method for a magnetic system can lead to several metastable configurations for self-consistent-field solutions. The *U*-ramping method was used in this study to determine electron orbital occupation corresponding to the correct ground state of magnetic system as proposed by Mereding *et al.*. In order to determine the true magnetic ground states of UO_2 and NpO_2, the relativistic spin-orbit interactions (SOI) were also considered in our calculations. In order to study phase stability of $U_{1-x}Np_xO_2$ and $Th_{1-x}Np_xO_2$ MOX, 96 atom special quasirandom structures (SQS) were used. A 4×4×4, 8x8x4 and 8×8×8 *k* point mesh were used in all calculations of structural optimization for 96, 24 and 12 atoms cells, respectively [17].

The MD simulations to determine thermal properties were carried out using the Large-scale Atomic Molecular Massively Parallel Simulator (LAMMPS) where the Coulombic interactions were calculated using the Ewald method. The empirical interatomic potential model used in this study combines a pair-wise (Buckingham-Morse type) with a many body interaction term. This particular potential model was developed to reproduce experimental thermo-mechanical properties of actinide oxides AcO_2 with An={Ce, Th, U, Np, Pu, Am, Cm} in a temperature range of 300 K to 3000 K and to reproduce the Cauchy violation in the elastic properties. This potential model was later extended to include potential parameters for the MOX compositions of AcO_2. In the present study, the MD supercell was constructed from 4000 cations and 8000 anions in an array of 10x10x10 unit cells for $U_{1-x}Np_xO_2$ and $Th_{1-x}Np_xO_2$ and their end members. MD runs were performed with a 1 fs time step over the temperature range 300 K to 3000 K at interval of 25 K, with the NPT ensemble at zero external pressure using the Nosé-Hoover thermostat and barostat with a time constant of 0.1 ps and 0.1 ps, respectively. Each simulation of thermodynamical quantities was carried out initially for 40 ps to establish equilibration (at the desired temperature) and then for another 10 ps to obtain average values of the thermodynamic quantities while heating the system. For calculations of thermal conductivity within LAMMPS, the Green-Kubo (GK) formalism was adopted where an estimate of the transport coefficient relies on the integral of an accurate time-correlation of the equilibrium fluctuations of heat flux in the system [16].

The binding energies and migration barriers were calculated using static calculations in a 10x10x10 supercell. The calculations were performed to determine binding energies of configurations where the oxygen vacancy is first (1st NN) or second (2nd NN) nearest neighbor (NN) with respect to the dopant atom. The calculations of migration barrier were performed using the nudged elastic band method as implemented in LAMMPS code in static condition. The migration barriers were calculated for the hopping of oxygen vacancy to a NN site along the <001> direction, which is known to be the lowest barrier migration direction in fluorite-based oxides. In order to determine the diffusion of the oxygen vacancy mean square displacements (MSD) were calculated for 5 ns for a temperature range from 750 K to 2000 K. To capture substantial oxygen diffusion on the limited MD timescale, 1% oxygen vacancies in the supercell was introduced. The charge imbalance in the system was compensated by an equivalent background charge [16].

3. Results and Discussions

a) Formation enthalpies of MOX

The variation of structural and electronic properties of UO_2 and NpO_2 with collinear ferromagnetic (FM), collinear anti-ferromagnetic (AFM) and non-collinear AFM arrangements of the uranium and neptunium magnetic moments are investigated while ramping up the U_{eff} from 0 eV, corresponding to standard density functional theory, upto U_{eff} = 4 eV, the value that correctly reproduces the AFM ground state of bulk UO_2 and NpO_2 (the so-called U_{eff}-ramping method). Analysis of structural and electronic properties of UO_2, NpO_2 and ThO_2 shows that spin-orbit interactions (SOI) had only a small effect on lattice parameters and electronic properties. The effect of FM and collinear AFM ordering is considered in determining the mixing enthalpies (ΔH_{mix}) [17].

Fig.1(a) shows ΔH_{mix} calculated using SQS in FM and ordered AFM configurations (along [001] direction) of $Th_{1-x}Np_xO_2$ MOX as a function of composition (x). The FM-SQS results (circles) are generated using the FM ground state of NpO_2, while AFM results (triangles) are generated using the AFM ground state of NpO_2. The calculated ΔH_{mix} values are positive and nearly symmetric around x = 0.5, suggesting a miscibility-gap phase diagram for fluorite structured random solid solutions, consistent with previous calculations. The ΔH_{mix} of the AFM configuration is higher compared to the FM configuration maximum by 0.19 kJ/mole. A quadratic fit of the ΔH_{mix} (shown as a dashed curve in Fig.1(a)) approximates $Th_{1-x}Np_xO_2$ MOX system as a regular solid solution. The interaction parameter Ω can be obtained from the formula:

$$\Omega = \frac{\Delta H_{mix}}{X(1-x)} \qquad (1)$$

and results are Ω = 2.82 and 3.47 kJ/mole for SQS-FM and AFM configuration, respectively. Our DFT calculated endothermic interaction parameters are lower compared to experimental value of 15.1±2.2 kJ/mol for ThO_2-CeO_2 MOX. Although, a lower value (for $Th_{1-x}Np_xO_2$) is expected compared to $Th_{1-x}Ce_xO_2$ considering lower mismatch of ionic radii for ThO_2-NpO_2 (Th^{+4}=1.19 Å, Np^{+4}=1.12 Å, 8-fold coordination) compared to ThO_2-CeO_2 (Th^{+4}=1.19 Å, Ce^{+4}=1.11 Å, 8-fold coordination). The difference in experimental and theoretical results of ΔH_{mix} can also be attributed to vibrational contribution to ΔH_{mix} and degree of configurational disorder present in the solid solutions. The vibrational contribution is expected to be negligibly small at room temperature. In our calculation random configurational disorder is assumed and thus neglecting any contributions from short-range order (SRO) which may be present in the experimental solid solutions that are equilibrated at high temperature.
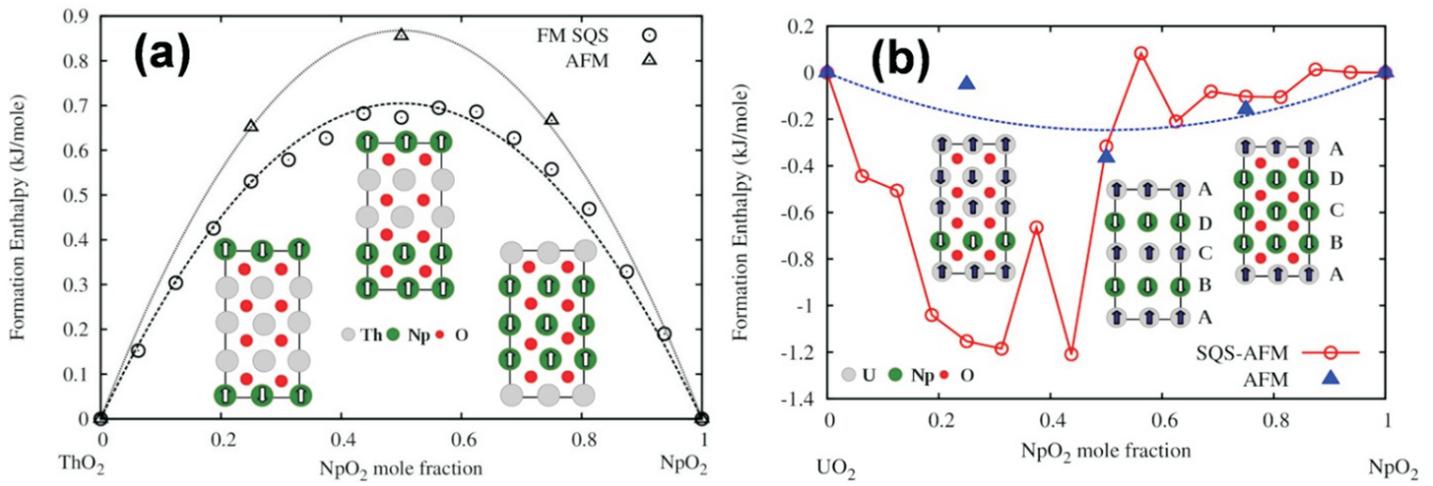
Fig.1: GGA+U calculated formation enthalpies of (a) $Th_{1-x}Np_xO_2$ MOX in FM (open circles) and AFM (open triangles) configurations. Similarly, formation enthalpies of (b) $U_{1-x}Np_xO_2$ MOX in random AFM (open circles) and ordered AFM (solid triangles) along [001] configurations. The magnetic structures of $Th_{1-x}Np_xO_2$/$U_{1-x}Np_xO_2$ (x=0.25, 0.50, 0.75) MOX in AFM configurations is shown with small arrows on atoms.

Fig.1(b) shows formation enthalpies of random AFM solid solutions calculated employing SQS and AFM configurations ordered along [001] direction of $U_{1-x}Np_xO_2$ MOX. The AFM SQS results (circles) are generated using the AFM ground state of UO_2 and NpO_2 with the spins of Np and U atoms distributed in such a fashion that the overall spin is zero or a minimum. Because neptunium and uranium atoms have different local spins, 3 μ_B/Np^{4+} ion and 2 μ_B/U^{4+} ion, the total magnetic moment is not zero for $U_{1-x}Np_xO_2$ MOX in their ordered AFM states (for x 0 and 1). For $U_{0.75}Np_{0.25}O_2$, $U_{0.50}Np_{0.50}O_2$ and $U_{0.25}Np_{0.75}O_2$ MOX, the effective magnetic moments are 1.92 μ_B, 11.84 μ_B and 5.95 μ_B, respectively. The ΔH_{mix} of ordered AFM and SQS AFM configurations are negative or very close to zero. For SQS AFM configurations ΔH_{mix} are negative up to $U_{0.50}Np_{0.50}O_2$ with maximum value of -1.21 kJ/mole at $U_{0.4375}Np_{0.5625}O_2$ while Np-rich $U_{1-x}Np_xO_2$ MOX has ΔH_{mix} values close to zero (< - 0.2 kJ/mol). The ΔH_{mix} versus concentration curve is not smooth showing small jumps at some specific compositions, which may be due to the slightly higher mismatch of correlation functions of generated SQS structures at these compositions with those of their ideal-random alloy counterparts. The fitting of equation (1) to our DFT calculated ΔH_{mix} values for AFM configurations (shown by dashed line in Figure 1(b)) gives Ω = -0.985 kJ/mole. High temperature oxide melt solution calorimetry measured ΔH_{mix} values are zero within experimental error bar for $Th_{1-x}U_xO_2$ and $U_{1-x}Ce_xO_2$ MOX systems. The negative values of Hmix in the U-rich $U_{1-x}Np_xO_2$ MOX is corroborating with the fact that long range AFM ordering is present in single crystal $U_{0.75}Np_{0.25}O_2$ below T_N = 17 K.

b) Thermal Expansion

Fig.2 (a) shows the increase of lattice parameter as a function of temperature for $Th_{1-x}Np_xO_2$ (x= 0, 0.065, 0.125, 0.25, 0.50, 0.75 and 1.00) and $U_{1-x}Np_xO_2$ (x= 0, 0.065, 0.125, 0.3125, 0.50, 0.6875 and 1.0). High temperature XRD data for ThO_2, UO_2 and NpO_2 are also included in the figure. The overall decrease in lattice parameters compares well with experimental data, which follow Vegard's law. This is demonstrated by fitting our MD calculated lattice parameters to a straight line equation: $a(U_{1-x}Np_xO_2)$ = 5.4699 – 0.0359 x, 1 < x < 0, since it matches well with Vegard's law of the form $a(U_{1-x}Np_xO_2)$ = 5.4702 – 0.0364 x, 1 < x < 0, fitted to the experimental lattice parameters of UO_2 and NpO_2 (5.4702 Å and 5.4338Å, respectively). Thermal expansion coefficients (α) (in 300-1300 K range) are

11.12, 11.08, 11.00, 10.85, 10.77, 10.65, 10.35 K^{-1} for x= 0, 0.065, 0.125, 0.3125, 0.50, 0.6875 and 1.0 in $U_{1-x}Np_xO_2$, respectively. These values are in good agreement with experimental values of 10.34, 10.20, 10.18, 10.08 and 10.01 K^{-1} for x= 0.0, 0.1, 0.5, 0.7, and 1.0, respectively. For ThO_2, values for a_{300} and α match previous high-temperature XRD data with only a 2% deviation. Nevertheless, the calculated value of UO_2 and NpO_2 are over predicted by 7.6% and 3.4%, respectively, compared to experimental values. The values of a_{300} for $Th_{1-x}Np_xO_2$ decrease with increasing NpO_2 concentration and the overall decrease in lattice parameters can be represented as: $a(Th_{1-x}Np_xO_2)$ = 5.59538 - 0.162021 x, 1 < x < 0. It matches well with Vegard's law of the form $a(Th_{1-x}Np_xO_2)$ = 5.5967 – 0.0534 x, 1 < x < 0, fitted to the experimental lattice parameters of ThO_2 and NpO_2 (5.5967 Å and 5.4338 Å, respectively). The variation of lattice parameters of $Th_{1-x}Np_xO_2$ and $U_{1-x}Np_xO_2$ MOX with the variation of NpO_2 content, x, is shown in **Fig.2(b)**. Accompanying the increment of temperature, from 300 K to 2000 K, the structural parameters of both $Th_{1-x}Np_xO_2$ and $U_{1-x}Np_xO_2$ decrease linearly with increasing value of x. From comparison of the two figures, we can clearly see that the reduction rate of $Th_{1-x}Np_xO_2$ is greater than $U_{1-x}Np_xO_2$ MOX, which indicates that the NpO_2 has a far greater influence on lattice parameters for $Th_{1-x}Np_xO_2$ than $U_{1-x}Np_xO_2$ MOX at same value of x. This phenomenon can be explained by the differences in ionic size of Th^{4+} (1.19 A), U^{4+} (1.14 A) and Np^{4+} (1.12 Å) in 8-fold coordination. Further, the variation of lattice parameters (in Å) of $Th_{1-x}Np_xO_2$ and $U_{1-x}Np_xO_2$ MOX can be presented as a function of NpO_2 concentration (x, 1.0 x 0.0) and temperature (T, 2000 T 300):

$$a(Th_{1-x}Np_xO_2) = -0.160777(x) + 4.44721*10^{-5}T + 6.87589*10^{-9}T^2 + 5.57487$$

$$a(U_{1-x}Np_xO_2) = -0.0397186(x) + 4.56747*10^{-5}T + 8.35801*10^{-9}T^2 + 5.45702$$

(2)

c) Thermal Conductivity

Fig.2(c) compares calculated thermal conductivity (TC) of $Th_{1-x}Np_xO_2$ (x=0.0, 0.0625 and 0.125) as a function of temperature with experimental values for pure ThO_2 [6-8]. Fig.2(d) compares calculated TC of $U_{1-x}Np_xO_2$(x=0.0, 0.0625, 0.125, 0.5 and 1.0) as a function of temperature, with experimental values for end members UO_2, NpO_2 and $U_{0.5}Np_{0.5}O_2$. The TC values of UO_2 and NpO_2 are quite close across this temperature range. However, classical MD
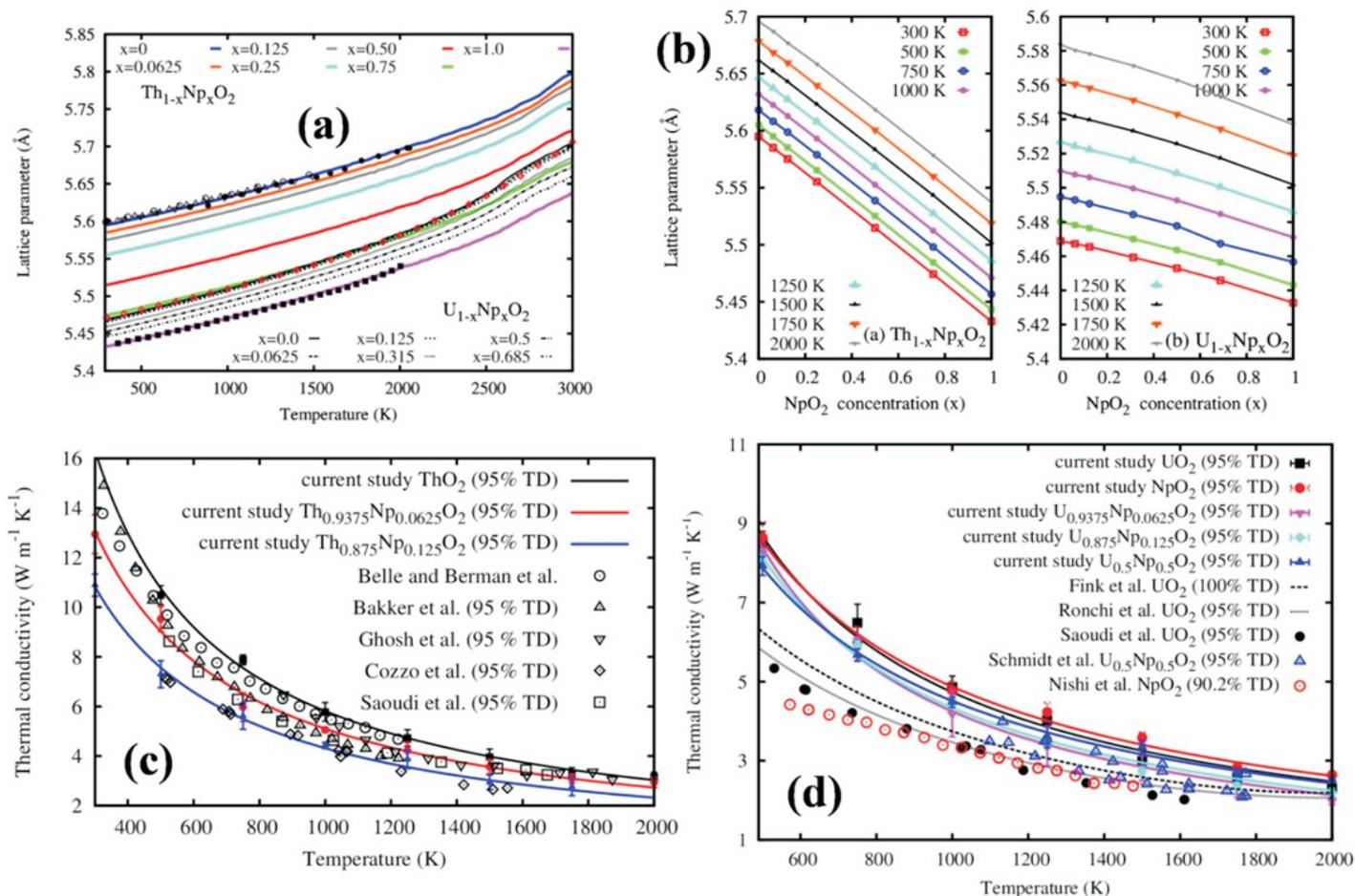
Fig.2: (a) The variation of calculated lattice parameters for $Th_{1-x}Np_xO_2$ (x=0.0, 0.0625, 0.125, 0.25, 0.50, 0.75 and 1.0) and $U_{1-x}Np_xO_2$ (x=0.0, 0.0625, 0.125, 0.3125, 0.5, 0.6875 and 1.0) as a function of temperature up to 3000 K. Lines present calculated values and points present high temperature XRD values of ThO_2, UO_2 and NpO_2. (b) Lattice constants calculated by MD simulations as a function of NpO_2 concentration (x) for $Th_{1-x}Np_xO_2$ and $U_{1-x}Np_xO_2$ solid solution. MD calculated thermal conductivity values (at 95% TD) for (c) $Th_{1-x}NpxO_2$ (x=0.0, 0.0625 and 0.125) and (d) $U_{1-x}Np_xO_2$ (x=0.0, 0.0625, 0.125, 0.5 and 1.0) are shown as a function of temperature. Experimental values of ThO_2, UO_2, NpO_2, and $(Np0.5U0.5)O_2$ MOX are compared with the calculated values.

calculated TC values of both UO_2 and NpO_2 are grossly overestimated at lower temperature (< 1000 K) compared to experimental values. In order to improve the accuracy of the thermal-conductivity predictions for UO_2, MD results need be corrected for the spin-phonon-scattering mechanism by adding the corresponding relaxation time derived from existing experimental data as shown by Liu *et al.*.

Fig.2(d) also indicates a small reduction in TC values for $U_{1-x}Np_xO_2$, even at low temperatures, due to reduction in the phonon mean free path coming from scattering associated with a non-uniform cation sublattice. The degradation of the UO_2 thermal conductivity due to Np substitutional defects is relatively small compared to the addition of Np in ThO_2. The calculated TC values of $(Np_{0.5}U_{0.5})O_2$ are lower than those of pure UO_2 and NpO_2 due to higher impurity-phonon scattering at low temperatures (<750 K). The calculated TC values of $(Np_{0.5}U_{0.5})O_2$ also match the experiment well throughout the temperature range with maximum deviation of 15%. This is consistent with the experimental observation that the TC of NpO_2 with 95%TD was close to that of $(Np_{0.5}U_{0.5})O_2$ above 1098 K. At higher temperatures (above 750 K), the TC values are almost independent of the NpO_2 concentration and the TC values for UO_2, NpO_2 and $(U,Np)O_2$ MOX almost superimpose at high temperatures [16].

Table 1. A comparison of constants A and B of the equations $1/k$= A+BT for $Th_{1-x}Np_xO_2$ (x=0.0, 0.0625 and 0.125) and $U_{1-x}Np_xO_2$ (x=0.0, 0.0625, 0.125, 0.5 and 1.0) derived from MD simulations and from experimental measurements. The C_{PQ} values are also shown in the table.

	A($\times 10^{-2}$)mKW^{-1}	B($\times 10^{-4}$)mW^{-1}
ThO$_2$		
MD, this study	1.282	1.466
Experiment [7]	4.200	2.250
Experiment [6]	1.000	2.300
Experiment [8]	3.170	1.699
(Th$_{0.9375}$Np$_{0.0625}$)O$_2$ MD, this study	2.356	1.581
(Th$_{0.875}$Np$_{0.125}$)O$_2$ MD, this study	3.034	1.543
UO$_2$		
MD, this study	1.896	1.923
Experiment [6]	6.548	2.353
Experiment [6]	6.240	2.399
(Th$_{0.9375}$Np$_{0.0625}$)O$_2$ MD, this study	2.981	2.32
(Th$_{0.875}$Np$_{0.125}$)O$_2$ MD, this study	3.045	2.16
(U$_{0.5}$Np$_{0.5}$)O$_2$ MD, this study	3.213	1.89
NpO$_2$		
MD, this study	2.861	1.770
Experiment (573-1473K)[29]	9.447	1.797
C_{Th-Np}= 4.198x10^{-1}		
C_{U-Np}=6.674 x 10^{-3}		

The calculated TC values of MOX are fitted to the relation of phonon conduction as proposed by Adachi et al.:

$$k = 1/[x W_{PO_2} + (1-x) W_{QO_2} + x(1-x) C_{PQ}], \quad (3)$$

where x = fractional concentration of lattice defects in $P_x Q_{1-x} O_2$, and $W_{PO_2} = A_{PO_2} + B_{PO_2} T$ and $W_{QO_2} = A_{QO_2} + B_{QO_2} T$ are thermal resistivity of end-members. If $x = 0$ or $x = 1$, the above equation becomes

$$k = 1/(A + BT) \quad (4)$$

The 'A' and 'B' represent defect-phonon scattering and phonon-phonon scattering contributions, respectively. The C_{PQ} arises due to the random distribution of P and Q atoms on a given sublattice. The influence of substituted impurities on the TC is attributed to an increase in parameter 'A' which is temperature independent. This results from interactions of phonons with lattice imperfections, impurities, isotopic, or other mass differences as well as defects such as grain boundaries and dislocations in the sample. Parameter 'B' can be considered a constant and the second term, namely $B.T$, represents the intrinsic lattice thermal resistivity caused by phonon-phonon scattering. With increasing temperature this term becomes dominant. One pair of A and B constants can be obtained for each solid solution composition by polynomial fitting of the thermal resistivity versus temperature data (Table 1). Moreover, MD calculated values are also fitted to above equation to determine the parameter C_{PQ} also shown in Table 1.

d) Oxygen Diffusion

The NEB calculated oxygen vacancy migration energies (E_m) for ThO$_2$, UO$_2$ and NpO$_2$ are reported in Table 2. The E_m of ThO$_2$ is highest and E_m's of UO$_2$ and NpO$_2$ differ by only 0.018 eV. Grovers et al. [34] calculated the E_m of UO$_2$ using nineteen different interatomic potentials and found that E_m's lie between 0.3 and 0.5 eV. The NEB calculated e_m of 0.40 eV, obtained from the current potential, is in good agreement with those calculated earlier using different potentials as shown in the Table 2. Behera et al. calculated E_m for ThO$_2$ using eight different interatomic potentials and found that E_m's lie between 0.52 and 0.79 eV. Our NEB calculated E_m of 0.54 eV is within this range. Finally, Aidhy et al. calculated E_m for UO$_2$, ThO$_2$ and NpO$_2$ and found very similar values, as shown in Table 2.

Table 2 also reports the energy gained or lost when an oxygen vacancy occupies a site close to a single dopant in an otherwise dopant free supercell. The binding energy of the oxygen vacancy to the dopant atom, and is defined as $E_b = E(NN) - E(infinite)$, where $E(NN)$, is the energies of the supercell in which the oxygen vacancy occupies a near neighbor (1st NN) and second near neighbor (2nd NN) site with respect to the dopant atom and $E(infinite)$ is the energy of the supercell with only a dopant or only an oxygen vacancy is infinitely separated. These configurations are then used to identify the migration activation energies for an oxygen ion moving to the vacant site adjacent to the dopant cation. The presence of the dopant results in either small increase or decrease in activation energy depending on the ionic radius of the cations (Table 2).

In order to determine oxygen diffusivity in Th$_{1-x}$Np$_x$O$_2$ and U$_{1-x}$Np$_x$O$_2$ MOX, we compare the mean square deviations (MSD) of pure ThO$_2$, UO$_2$, NpO$_2$ and Th$_{1-x}$Np$_x$O$_2$, U$_{1-x}$Np$_x$O$_2$ MOX at five intermediate compositions calculated at 750 K, as shown in Fig.3 (a) and (b). We find that NpO$_2$ has a higher MSD slope than ThO$_2$, which can be attributed to the higher E_m of ThO$_2$ compared to any other oxide studied here (Table 2). Fig.3(a) also shows that the MSD slope

of Th$_{0.125}$Np$_{0.875}$O$_2$ and Th$_{0.25}$Np$_{0.75}$O$_2$ is almost equal to that of pure ThO$_2$ implying an almost equal rate of oxygen diffusion in all cases. Table 2 shows migration and binding energies of an oxygen vacancy adjacent to Th^{4+} in NpO$_2$ and Np^{4+} in ThO$_2$. The binding energy (E_b) is negative in the case of Th^{4+} present as a dopant in NpO$_2$ signifying that the oxygen vacancy does not favor the 1st NN position with respect to the Th^{4+} dopant ion in NpO$_2$. Conversely, E_b is positive in the case of Np^{4+} present as dopant in ThO$_2$. The migration barrier for oxygen increases from 0.419 eV in defect free NpO$_2$ to 0.470 eV in the presence of single Th^{4+} at 1st NN to 0.583 eV when there are two Th^{4+} cations at 1st and 2nd NN site. This is consistent with the decrease in oxygen diffusion in NpO$_2$ as a function of ThO$_2$ concentration as shown in the MSD curve. The oxygen migration barrier decreases from 0.537 eV in defect free ThO$_2$ to 0.413 eV in the presence of a single Np^{4+} at 1st NN and 0.250 eV when Np^{4+} cations are present at 1st and 2nd NN sites. The lower migration barrier with increasing NpO$_2$ concentration is a consequence of the smaller ionic radius of Np^{4+} (0.98 Å) compared to Th^{4+} (1.05 Å) thereby providing more open space for oxygen ions to migrate. At a high concentration of NpO$_2$ (i.e. Np$_{0.25}$Th$_{0.75}$O$_2$) the lower oxygen diffusivity in ThO$_2$ is compensated by the higher oxygen diffusivity in NpO$_2$, resulting in a MSD slope almost identical to that of ThO$_2$. Aidya et al. calculated oxygen diffusivity in (Th,Ce)O$_2$ and (Th,U)O$_2$ MOX and found that with increasing Ce or U concentration in ThO2, oxygen diffusivity decreases due to the oxygen vacancy binding with Ce or U. Conversely, with increasing Th concentration in CeO$_2$ or UO$_2$ oxygen diffusivity decreases due to the increasing migration barrier, this is in agreement with our results.

Table 2: Oxygen vacancy migration energies (E_m) calculated using static nudged elastic band (NEB) technique and binding energies (E_b) in ThO$_2$ when Np is present as a dopant (and vice versa) and in UO$_2$ when Np is present as a dopant (and vice versa). The calculated E_m values for pure oxides (ThO$_2$, UO$_2$ and NpO$_2$) are also compared with previous ab-initio and MD calculated values. Further, E_m is predicted from Arrhenius plot (diffusivity versus 1/temperature plot) by calculating mean square deviations (MSD) at different temperatures (from 750 to 2000 K in the interval of 250 K). 1st NN and 2nd NN refers to the near neighbour positions of the oxygen vacancy with respect to the dopant cation, 1st & 2nd implies two dopant ions in adjacent cation sites. The values of binding energies (E_b) shown in parenthesis are calculated using DFT calculation.

System	E_m(eV) MD (this study) From Static NEB	E_m(eV) MD (this study) From MSD	E_m(eV) Ab-initio (previous study)	E_m(eV) MD (previous study)
UO$_2$	0.401	0.393	0.67-1.34	0.3-0.5, 0.391
ThO$_2$	0.537	0.525	1.97-2.16	0.52-0.79, 0.530
NpO$_2$	0.419	0.423	-	0.42

System	Binding Energy(E_b) in eV 1st NN 2nd NN		Migration Energy(E_m) in eV 1st NN 1st & 2nd NN	
ThO$_2$:Np	0.284(0.368)	0.000	0.413	0.250
NpO$_2$:Th	-0.236(-0.984)	0.020	0.470	0.583
UO$_2$:Np	0.111(0.468)	0.000	0.371	0.360
NpO$_2$:U	-0.160(-0.066)	0.000	0.518	0.521

Fig.3(b) compares the MSDs of UO$_2$, NpO$_2$ and U$_{1-x}$Np$_x$O$_2$ MOX compositions. The slope of the MSD curve for U$_{0.875}$Np$_{0.125}$O$_2$ lies between those of UO$_2$ and NpO$_2$. The higher MSD slope for UO$_2$ can be attributed to the lower E_m in UO$_2$ as compared to that in NpO$_2$
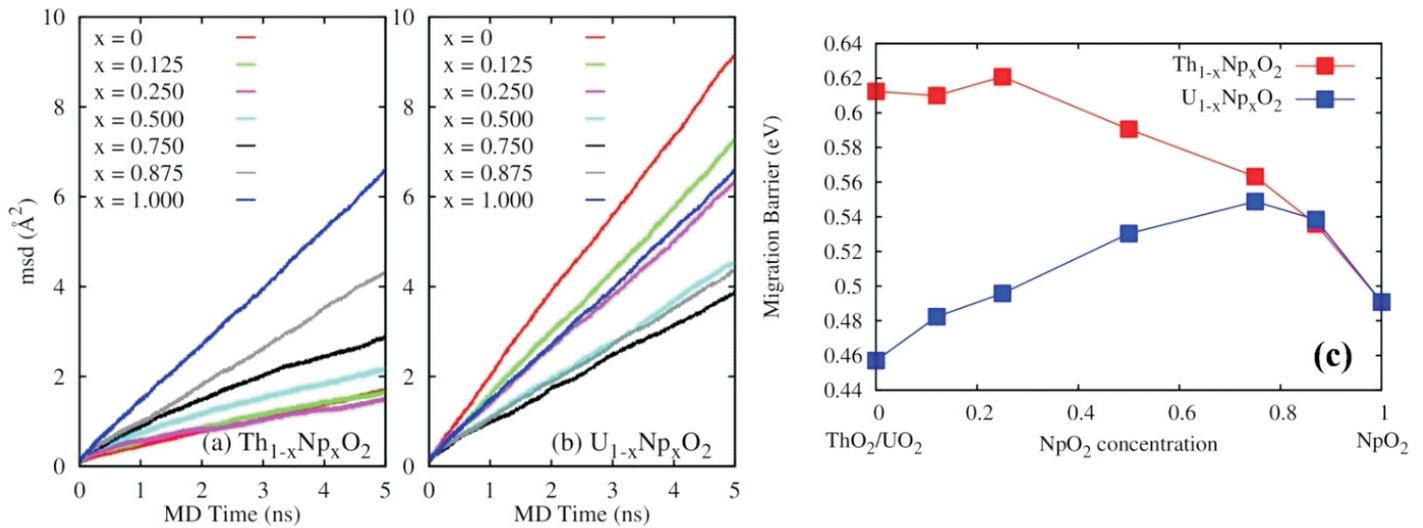
Fig.3: Mean square displacement (MSD) of oxygen as a function of MD simulation time in (a) $Th_{1-x}Np_xO_2$ and (b) $U_{1-x}Np_xO_2$ MOX calculated at 750 K. (c) The migration barriers (E_m) of oxygen vacancy in $Th_{1-x}Np_xO_2$ and $U_{1-x}Np_xO_2$ MOX as a function of NpO_2 concentration evaluated from MD calculated oxygen diffusivity as a function of temperature (Arrhenius plot).

(Table 2). With further increase of Np concentration, the slope of the MSD curve for $U_{0.75}Np_{0.25}O_2$ is almost equal to that of NpO_2. The slope of the MSD curves for other $U_{1-x}Np_xO_2$ MOX compositions are less than that of NpO_2. The migration barrier for the oxygen vacancy decreases from 0.401 eV in UO_2 to 0.371 eV in the presence of a single Np^{4+} ion at 1st NN to 0.360 eV in the presence of two Np^{4+} ions at 1st and 2nd NN. The lower migration barrier with increasing NpO_2 concentration is a consequence of the smaller ionic radius of Np^{4+} (0.98 Å) compared to U^{4+} (1.00 Å) thereby providing more open space for oxygen ions to migrate as discussed for $(Th,Np)O_2$ MOX. Moreover, the binding energy of the oxygen vacancy in UO_2 in the presence of Np as 1st NN is positive implying the oxygen vacancy prefers to stay as the 1st NN to the Np^{4+} dopant ion in UO_2. This leads to the continuous decrease of the MSD slope in $U_{1-x}Np_xO_2$ MOX going from UO_2 to NpO_2. The binding energy of the oxygen vacancy in NpO_2 in the presence of U^{4+} as 1st NN is negative. Also the migration barrier of oxygen via a vacancy mechanism increases from 0.419 eV in NpO_2 to 0.518 eV in the presence of single U^{4+} ion at 1st NN to 0.521 eV with U^{4+} present at 1st and 2nd NN sites. This is consistent with the MSD slope reducing with increasing UO_2 concentration.

In order to further assess oxygen diffusion properties of MOX the MSDs were calculated for 5 ns using a 10x10x10 supercell (containing 12000 atoms) for a temperature range from 750 K to 2000 K (in 250 K interval). Overall features of MSD curve describe at 750 K is valid for MSD curve at higher temperatures but spread in MSD value at the end of 5 ns reduces drastically at higher temperature. The rate of reduction is higher for $U_{1-x}Np_xO_2$ compared to $Th_{1-x}Np_xO_2$ MOX. The MSD is related with oxygen diffusivity (D) by the relation MSD = 6Dt, where t is the MD time and in this case t = 5 ns. By assuming Arrhenius relationship the D is related to the migration energy (E_m) as

$$D = D_0 \exp(E_m/k_B T) \qquad (5)$$

where D_0 is the pre-exponential term, k_B and T is Boltzman constant and temperature, respectively. From the logarithmic plot of D as a function of $1/T$, E_m is determined over the NpO_2 concentration in MOX and those values are shown in Figure 3(c). The E_m values of the oxides derived from the Arrhenius plot are also shown in Table 2 and those values are matching within 2.5% of E_m values determined

from static NEB calculations. Moreover the sequence of the E_m values of the oxides is consistent with that determined from NEB calculations. Fig.3(c) shows slight increase of E_m with increase of NpO_2 concentration for $Th_{1-x}Np_xO_2$ MOX up to x=0.25 followed by continuous decrease up to x=1.0. On the contrary, the E_m increases continuously with increasing NpO_2 concentration up to x=0.75 followed by decreasing trend up to x=1.0. Fig.3(c) clearly shows nonlinear variation of the E_m with NpO_2 concentration and maxima lies around x=0.25 and 0.75 for $Th_{1-x}NpO_2$ and $U_{1-x}NpO_2$ MOX, respectively.

Conclusions

Main conclusions of the present study are as follows:

a) The calculated ΔH_{mix} of $Th_{1-x}Np_xO_2$ MOX were positive compared to the end members and nearly symmetric around x=0.5 and ΔH_{mix} of AFM configuration is higher compared to FM configuration maximum by 0.19 kJ/mole. The ΔH_{mix} of $U_{1-x}Np_xO_2$ MOX were negative up to $U_{0.50}Np_{0.50}O_2$ with maximum value of -1.21 kJ/mole at $U_{0.4375}Np_{0.5625}O_2$ whereas Np-rich $(U,Np)O_2$ MOX compositions exhibited ΔH_{mix} close to zero. Value of ΔH_{mix} for $(Th,Np)O_2$ are consistent with a simple miscibility-gap phase diagram while those for $(U,Np)O_2$ suggest a more complex behaviour. Nevertheless, lattice parameters variation with compositions till follows a Vegard's law relationship.

b) The calculated lattice parameter versus temperature curves of UO_2, NpO_2 and $U_{0.875}Np_{0.125}O_2$ match well within 1% of high temperature XRD values. At higher compositions of NpO_2, our MD calculated values are over prediction of high temperature XRD values (within 2%) throughout the temperature range. Linear thermal expansion coefficients (LTEC) of $Th_{1-x}Np_xO_2$ increase with NpO_2 concentration; while LTEC of $U_{1-x}Np_xO_2$ decreases with NpO_2 concentration.

c) The degradation of thermal conductivity in $U_{1-x}Np_xO_2$ is far less significant compared to that in $Th_{1-x}Np_xO_2$. This is governed by the fact that Np has very similar ionic radius and atomic mass as that of U than Th and defect-phonon scattering is less in $U_{1-x}Np_xO_2$. Therefore, generation of 6.25 atom% of Np (as minor actinide) degrades the thermal-conductivity of ThO_2-base MOX fuel by 24.0-12.5 % in the 750-1000 K temperature range. Conversely, mixing of

Np with UO_2-based MOX fuel up to by 50 atom% degrades the thermal-conductivity only by 13-2.3% in the 750-1000 K temperature range.

d) The oxygen diffusivities in $Th_{1-x}Np_xO_2$ and $U_{1-x}Np_xO_2$ MOX are calculated and are found to be higher in UO_2 and NpO_2 compared to that in ThO_2 due to lower oxygen migration barriers. With the addition of Th^{4+} to NpO_2, the diffusivity decreases due to the increase in the migration barriers introduced by a larger ionic radius of Th^{4+} compared to Np^{4+}. However, addition of Np^{4+} to ThO_2 decreases oxygen diffusion due to oxygen vacancy binding with Np^{4+}, even though the migration barriers decrease due to the smaller size of Np^{4+} than the host Th^{4+}. Similar observation can be made in $U_{1-x}Np_xO_2$. Our MD calculated binding energies follow the trend in isolated oxygen Frenkel pair defect energies (O-FP$_{isolated}$) of individual actinide oxides. Moreover, our MD calculated oxygen vacancy binding energy is consistent with the DFT calculated binding energies.

e) A database of thermal expansion, thermal conductivity and oxygen diffusion parameters has been developed which can be used to design new generation fuels.

Corresponding Author*

A.K. Arya (aarya@barc.gov.in)

References

[1] Actinide and fission product partitioning and transmutation, Status and assessment Report, NEA, OECD, 1999.

[2] V. Anastasov, M. Betti, F. Boisson, F. Depisch, F. Houlbreque, R. Jeffree, I. Khamis, S. Lattemann, J. Miquel, S. Nisan, Status of minor actinide fuel development, IAEA nuclear energy series, 2009.

[3] R. Konings, J. Kloosterman, *Progress in Nuclear Energy,* 2001, **38**, 3, 331-334.

[4] P. Dey, M. Giroux, A. Khaperskaya, J. Laidler, A. Machiels, M. Masson, F. Storrer, G. Uchiyama, Spent fuel reprocessing options, IAEA-TECDOC-1587.

[5] V. Smirnov, V. Sobolev, J. Somers, R. Srivenkatesan, A. Stanculescu, V. Subbotin, A. Surenkov, T. Suzuki, M. Szieberth, S. Taczanowski, Advanced reactor technology options for utilization and transmutation of actinides in spent nuclear fuel, IAEA-TECDOC-1626.

[6] International Atomic Energy Agency, Thorium fuel cycle-potential benefits and challenges, IAEA-TECDOC-1450, IAEA, Vienna, 2005.

[7] P.S. Ghosh, P.S. Somayajulu, A. Arya, G.K. Dey and B.K. Dutta, *J. Alloys Compd.*, 2015, **638,** 172-181.

[8] P.S. Ghosh, P.S. Somayajulu, R. Krishnan, N. Pathak, A. Arya and G. K. Dey, *J. Alloys Compd.*, 2015, **650,** 165-177.

[9] P.S. Ghosh, N. Kuganathan, C.O.T. Galvin, A. Arya, G.K. Dey, B.K. Dutta and R.W. Grimes, *J. Nucl. Mater.*, 2016, **476,** 112-122.

[10] P.S. Ghosh, A. Arya, N. Kuganathan, G.K. Dey and R.W. Grimes, *Physical Chemistry Chemical Physics,* 2016, **18,** 31494-31504.

[11] P.S. Somayajulu, P.S. Ghosh, A. Arya, K.V. Vrinda Devi, D. B. Sathe, J. Banerjee, K. B. Khan, G.K. Dey and B.K. Dutta, *J. Alloys Compd.*, 2016, **664,** 291-303.

[12] P.S. Somayajulu, P.S. Ghosh, J. Banerjee, K.L.N.C. Babu, K.M. Danny, B.P. Mandal, T. Mahata, P. Sengupta, S.K. Sali and A. Arya, *J. Nucl. Mater.*, 2015, **467,** 644-659.

[13] P.S. Ghosh and A. Arya, *Physical Chemistry Chemical Physics ,* 2020, **22,** 6406-6417.

[14] P.S. Ghosh and A. Arya, *Physical Chemistry Chemical Physics,* 2019, **21,** 16818-16829.

[15] N. Kuganathan, P.S. Ghosh, A. Arya and R.W. Grimes, *Journal of Nuclear Materials.* 2018, **507,** 288-296.

[16] P.S. Ghosh, A. Arya, N. Kuganathan and R.W. Grimes, *Journal of Nuclear Materials*, 2019, **521,** 89-98.

[17] P.S. Ghosh, A. Arya, N. Kuganathan and R.W. Grimes, *Physical Chemistry Chemical Physics*, 2018, **20,** 18707-18717.

[18] N. Kuganathan, P.S. Ghosh, C.O.T. Galvin, A.K. Arya, B.K. Dutta, G.K. Dey, R.W. *Grimes, Journal of Nuclear Materials*, 2017, **485,** 47-55.

[19] N. Kuganathan, P.S. Ghosh, C.O.T. Galvin, A.K. Arya, G.K. Dey, R.W. Grimes, *Journal of Nuclear Materials*, 2017, **495,** 192-201.

Effective approaches towards exploring problems ranging from Molecules to Materials

Niharendu Choudhury*

Theoretical Chemistry Section, Chemistry Division

Bhabha Atomic Research Centre, Mumbai-400085, India

ABSTRACT

A brief account of the works carried out in this group in recent years is presented here. A range of fundamental as well as applied problems in Chemistry and related disciplines has been addressed by developing suitable theories, state of the art computer simulation techniques and performing large scale computations. Specifically, the theoretical and computational investigations encompassing broad areas of nuclear materials, waste management, energy and bio-molecular systems have direct relevance to the thrust areas of research in DAE. Research related to exotic chemical/physical problems through development of novel computational techniques have also been discussed. The whole gamut of work described here includes design of new materials with tailor made properties and explaining observed phenomena with electronic and/or atomic scale resolutions through the applications of first principle quantum mechanical methods as well as classical statistical mechanical theories and simulations.

Keywords: Multi scale-modeling, Nanomaterials, Hydrogen storage, Biomacromolecules, Ligand design.

Introduction

With the advent of newer theoretical processes and high performance supercomputing machines along with the availability of many state of the art program suits, applications of theoretical methods in solving complex chemical, physical and biological problems have been an integral part of the modern day research. Any scientific problem can be treated theoretically if the correct lengthscale for tackling the problem can be identified. In that perspective, various lengthscales starting from the most fundamental quantum mechanical domain to atomistic to meso scale to ultimately continuum domain with an underlying hierarchical thread intertwining the domains in the order mentioned above exist. Among all, quantum domain, being the fundamental of all, is governed by the laws of quantum mechanics, whereas all other domains are either based on laws of statistical mechanics or relied on hydrodynamic principles. A true multiscale modelling [1-2] of any material rests on the successful flow of information from the lowest to the higher lengthscales. In the present article, we shall confine ourselves to the problems belonging to the first three domains, namely, quantum, atomistic and meso scale domains.

In what follows, we have described various computational codes used in Sec. 2, various results on Nuclear Materials and Fuel Cycles in Sec. 3.1, Energy and Environment in Sec. 3.2, Soft Condensed Matter in Sec. 3.3, Bio-Inspired Research in Sec. 3.4 and Development of Theoretical Methodologies and Computer Codes in Sec. 3.5. Finally we offer concluding remarks in Sec. 4.

2. Methodology

In dealing with these topics, ab-initio electronic structure calculations for atoms, molecules, clusters and solids, and classical mechanics based molecular dynamics simulations at the atomistic and coarse-grained levels have been extensively used. Standard codes like VASP, GAMESS, ORKA, MOLPRO and many programs developed in-house have been employed for the topics requiring quantum mechanical framework. On the other hand, larger system sizes have been tackled through the uses of classical molecular dynamics (MD) and coarse-grained MD simulations. Standard codes like GROMACS and many in-house developed MD programs along with many analysis codes have been extensively used in many of these cases.

3. Results and Discussions

3.1 Nuclear Materials and Fuel Cycles

In this sub-section, the recent findings on nuclear materials using computational techniques are described.

A. Understanding radiation damages in nuclear structural materials

Ferritic and austenitic steels are the most important structural materials used in industries, in particular, in the nuclear industry. These steels are used mainly for making reactor pressure vessels (RPV) in nuclear reactors, where high temperature and neutron irrradiation can degrade the material properties, and thus limit the lifetime of the reactor's structural components. Steels are alloys of Fe, C and many other small and large solute atoms (SAs) like Ni, Cu, Cr etc. It has been found that the Cu precipitation is one of the primary reasons for the embrittlement of irradiated RPV steels. We have investigated here using first principle electronic structure calculation, in conjugation with the experimental investigation conducted in Material Science Division, BARC about the origin of Cu clustering in steels. The electronic level understanding of such Cu cluster formation reveals [3,4] that Cu-Cu interaction is attractive in nature and the extent of attractiveness increases in presence of the vacancy (V), which is amply generated at high temperatures and
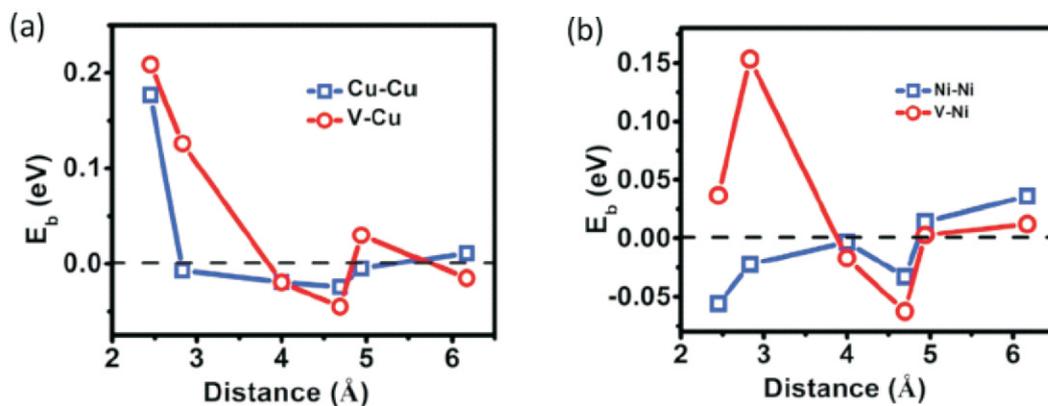
Fig.1: Binding energies of SA–SA and V–SA pairs as a function of the distance in bcc-Fe for (a) Cu–Cu and V–Cu, (b) Ni–Ni and V-Ni.
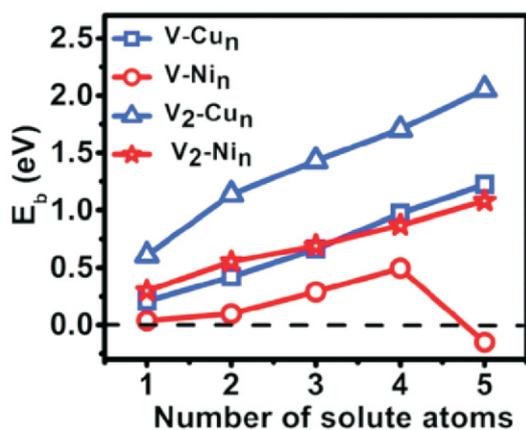
Fig.2: Binding energies of V–Xn and V2–Xn clusters (V stands for vacancy).

irradiation. In Fig.1(a) and (b) we show how SA-SA (SA=Cu, Ni) interaction changes as a function of distance between them. It is to note that the Cu-Cu, V-Cu and V-Ni interactions are attractive (positive energy stands for attraction). The interaction energy of the vacancy-SA clusters shown in Fig.2 demonstrate attractiveness among the SAs increases with number of solute atoms and a vacancy or a di vacancy can bind 5 or more Cu atoms in the Fe matrix. Origin of such interaction was further analysed to reveal a compensatory nature of electronic and distortion energies [4]. It is interesting to explore the different factors that control the nature of the interactions amongst different entities. Components of the total interaction energy, which is split into two major components, namely the electronic effect and the distortion effect are shown in Fig.3. The electronic factor primarily includes the effect of electron redistribution, and the distortion effect is related to the strain induced or relieved upon replacement of Fe atoms by solute atoms. It is observed (Fig.3) that the nature of the two components are very much configuration dependent and the two component energies are compensatory in nature i,e. if one is favourable then another is opposing a particular configuration.

B. Fuel reprocessing

Liquid-Liquid Interface: An important issue at the back end of the fuel cycle is the separation of actinides and lanthanides. Computational design of new ligands and various host molecules based on their interactions with the ions has now become an integral part of the advanced research in this field. Of the fission

products, partitioning minor actinides (MAs) such as americium and curium from the bulk are often difficult. We have found that supramolecular host molecules are better candidates for the trivalent separation of Eu and Am due to the favourable host-guest interactions.[5] Of the several hosts, cucurbituril (CB-[n]) hosts are classic cationic binders due to favourable ion-dipole interactions. Our electronic structure calculations show that presence of counter-ions such as nitrate enhances the binding affinities of Am cations as shown in Fig.4.

Solid-liquid Interface: Liquid-liquid extraction have been utilized for many years in the nuclear industry for the reprocessing of the spent fuels [6-7]. Many difficulties associated with the conventional liquid-liquid extraction process such as excessive use of organic solvents, difficulties in separating different phases etc. can be nicely overcome if a heterogeneous solid-liquid interface based method is used. Due to tailor made adsorption properties, the functionalized carbon nanotube (CNT) based membrane separation method will be a very useful alternative to the conventional solvent extraction processes. In order to design a better separation process, thorough knowledge about the structure and dynamics of actinyl ions in water is essential. In a series of investigations using MD simulations, we have investigated structural and dynamical aspects of uranyl ions in water at different temperatures and concentrations of uranyl ions [8,9] and at supercritical conditions [10,11] relevant to supercritical extraction. We have further investigated the adsorption behaviour of the uranyl ions in different functionalized CNTs [12,13]. Detailed analyses demonstrate that the mode of adsorption in –COO–
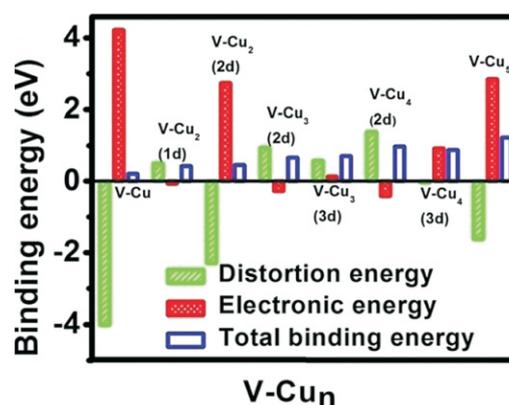
Fig.3: Decomposition of total binding energy of V–Cun complexes into the distortion and electronic binding energies (where V stands for vacancy).
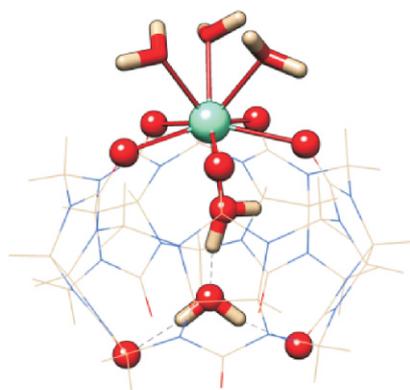
Fig.4: Optimized structure of Am-CB [5].
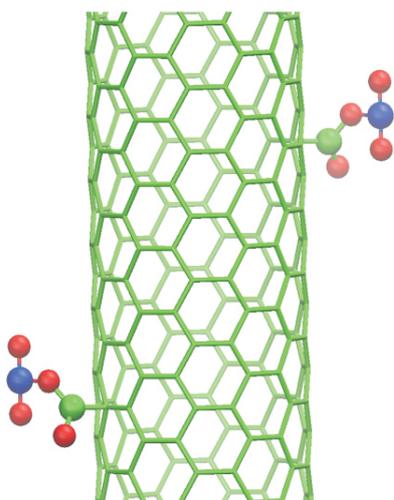
Fig.5: Carboxylate functionalized CNT.

Fig.6: Adsorption of uranyl ions per unit CNT.

Fig.7: The Ng atoms are adsorbed on the pores of M-MOF-74.

functionalized CNT (Fig.5) is different from bare and –OH/-COOH functionalized CNTs. Calculated adsorption isotherm (Fig.6) for uranyl ion adsorption shows that the carboxylate ion functionalized CNT has the maximum adsorption capacity.

On the other hand, entrapment of radioactive noble gases, Xe and Kr, needs special attention in the context of nuclear fuel reprocessing and nuclear reactor accidents. The generally employed cryogenic distillation process for the separation of noble gases is not cost effective. In recent years, use of porous materials is being actively discussed for adsorption and separation of noble gases. Metal-organic frameworks (MOFs) are considered superior in such applications owing to their high uptake capacity, and superior selectivity. Computational modelling of MOFs through tailoring their properties for noble gas mitigation helps us to identify the suitable candidates. For this purpose, we have investigated the binding of Xe and Kr in M-MOF-74 (Fig.7) employing first principle based electronic structure calculations. Our study [14] has shown that, Xe binds stronger than Kr and adsorption energy changes with the nature of the central metal atom in the MOF. We have also explored the MFM-300 (M) based MOFs for separation and storage of Xe and Kr [15].

Effect of fission products on fuel: For safe and efficient operation of nuclear reactors, gauging the effects of fission products (FPs) on the properties of the host fuel is extremely essential. For this purpose, knowledge of thermo-physical properties of UO_2 fuel in presence of the lanthanide (Ln) FPs is essential. Using DFT with Hubbard-U corrections various properties have been evaluated. The mechanical property viz. bulk modulus of Ln doped UO_2 is found to be directly related to the Ln doping concentration. The thermo-physical properties like heat capacity and coefficient of thermal expansion are also evaluated based on quasi-harmonic approximation to the phonon frequencies. The properties obtained from our *first principle* calculations show a good agreement (Fig.8) with the available experimental and theoretical results [16, 17].

Generating data base for advanced nuclear fuels: Designing advanced fuel materials such as accident tolerant fuels and the management of nuclear waste generated as a result of reactor operations are the two major challenges. Fuel materials like U_3Si_2, UAl_3 and U_2Mo have been projected as advanced fuels for nuclear reactors. Using ab-initio electronic structure calculations within the framework of density functional theory (DFT), various important thermophysical properties of these materials as well as various properties related to heat transport phenomena, such as, thermal conductivity, heat capacity, and thermal expansion coefficient have been calculated and these results will help in developing a database for such materials [18,19].

Energy and Environment

Increasing worldwide energy demands and rapidly depleting fossil fuel resources along with the environmental concerns signify the importance of sustainable and renewable energy options. Hydrogen is considered to be one of the best possible alternative energy carriers. However, to develop an efficient hydrogen energy system, two main hurdles are (a) cost effective generation of hydrogen from renewable resources like water through water splitting and (b) storage of hydrogen by developing efficient hydrogen storage materials and designing more efficient fuel cells to convert the chemical energy to electrical energy. Listed below are some of our efforts in those directions.
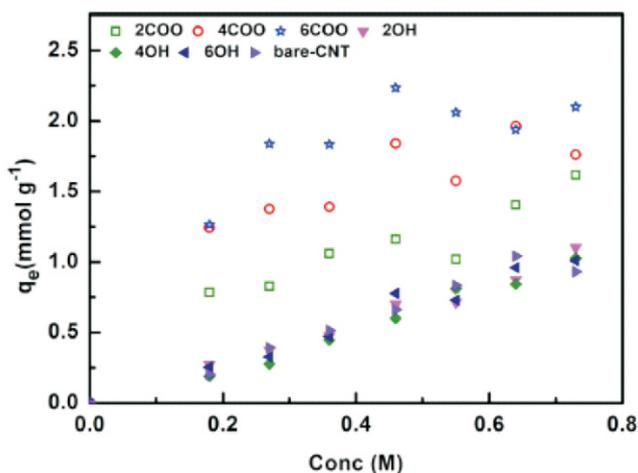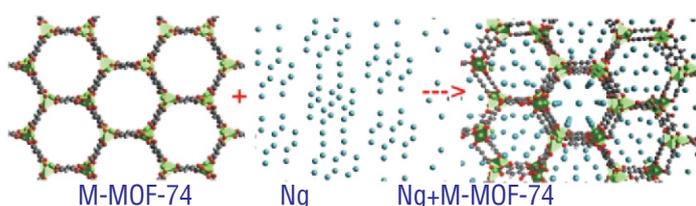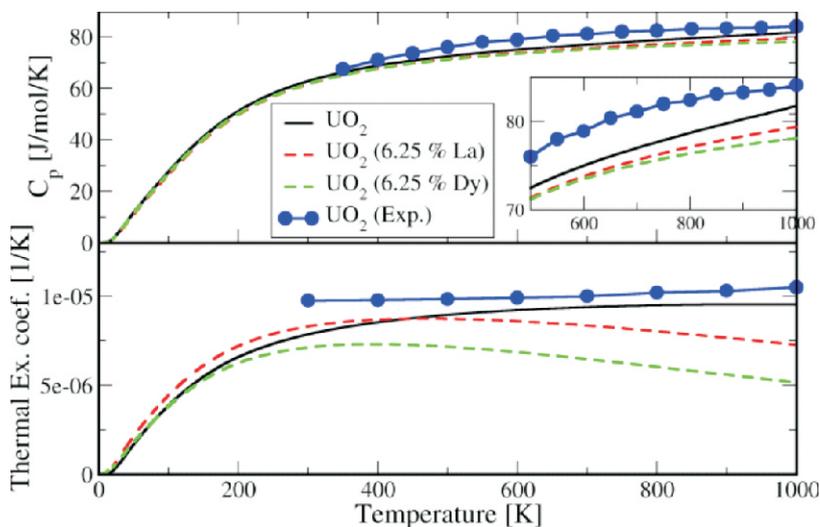
Fig.8: The effect of Ln fission product concentration on thermal properties of UO_2.

Water splitting: Photocatalytic water splitting reaction using the abundant solar energy and semiconductor materials is an ideal way to generate hydrogen. Large number of semiconductor materials such as TiO_2, ZnO, $SrTiO_3$, $NaTaO_3$, ZnS, CdS, $CdSe$, etc., have been studiedfor photocatalytic water splitting. Using the periodic density functional theory calculations, we explored [20-21] various oxide based photocatalysts like $SrTiO_3$, $KNbO_3$ and $NaTaO_3$ for their activity towards solar water splitting. Using DFT, we could explain the underlying reasons for the experimentally observed improved photocatalytic activity of Zr doped $KNbO_3$ towards the water splitting reaction [20]. Using DFT, we have explored the poly s-triazine based graphitic carbon nitride as possible photocatalyst for water splitting for the first time[21] and we could propose the hybrid carbon nitride, $g-C_3N_3/g-C_3N_4$ to be a better catalyst, the fact which has been experimentally proved very recently [21].

Hydrogen Storage: Hydrogen storage at ambient conditions is another major bottleneck for hydrogen-based energy systems. We demonstrated varieties of light metal decorated materials, like cyclic carbon molecular systems, fullerenes, boron hydrides, two-dimensional (2D) carbon materials, metal organic frameworks (MOFs) and porous carbon materials for their hydrogen adsorption characteristics based on some of the elegant chemical concepts such as the electrostatic interactions, curvature of carbon nanomaterials and aromatic nature of molecule-based materials, etc. [22-23]. Based on this knowledge, we have put forward [23] the single-walled carbon nano horns as one of the potential candidates for hydrogen storage on the basis of 'intra-curvature'. We have also investigated magnesium clusters for the purpose of hydrogen storage and our results [24] obtained from *ab-initio* molecular dynamic simulation have shown that a complete dehydrogenation from these Mg nanoclusters occurs at ~100^0C, a significant improvement over bulk MgH_2 (~300^0C).

3.3 Soft Condensed Matter

There are many exotic structural and dynamical phenomena involving macroscopic many-body systems and these problems should be tackled by using force-field based atomistic and coarse-grained simulations. Below are the depictions of many such topics in which theoretical and computation chemistry have played a major role to understand and unravel many apparently puzzling phenomena and observations.

Patterned C_{60} Solvation Shell: Accurate description of solvation structure of a hydrophobic nanomaterial is of immense importance to understand protein folding, molecular recognition, drug binding, and many related phenomena. Moreover, spontaneous pattern formation through self-organization of solvent molecules around a nanoscopic solute is fascinating and useful in making template-directed nanostructures of desired morphologies. Here, we show through coarse-grained MD simulation that the patterned solvation layer (Fig. 9) with the imprints of the hydrophobic surface atoms of the C_{60} can be obtained from a completely different mechanism
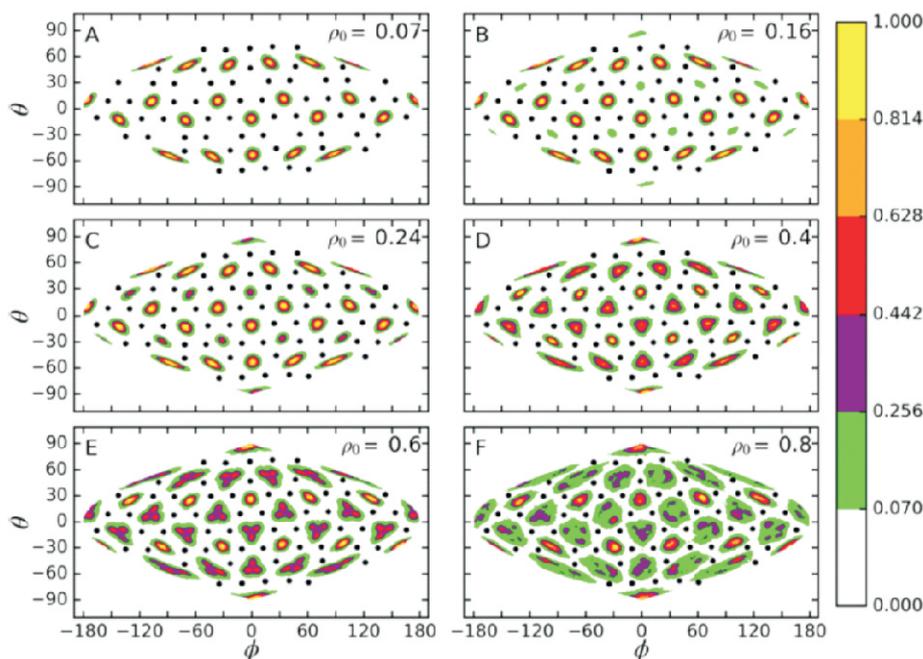
Fig.9: Pattern formation by the surrounding solvents of the C_{60} fullerene at different densities (ρ_0). Black dots are the positions of the C atoms of C_{60}. Pattern shows hexagonal faces have higher solvent densities as compared to pentagonal faces.
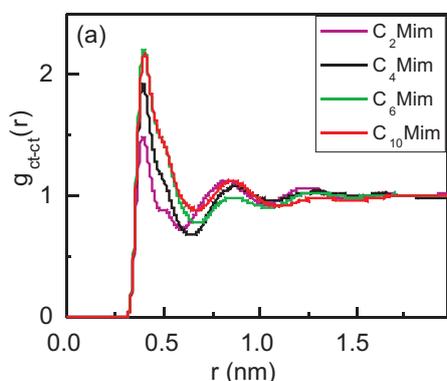
Fig.10: Radial distribution function, g(r) of the terminal carbon atom of the alkyl chain of the RTIL solvent around the same of another RTIL molecule.

arising from a spherically symmetric, short-ranged interaction having two characteristic lengthscales. The nature of the pattern can be modified by adjusting solvent density or pressure. The solute-solvent dispersion interaction is the key to such pattern formation adjacent to the solute surface. In Fig.9, we have shown the pattern of solvent molecules surrounding the C_{60} [25-26] at different bulk densities of the solvent. It is to note that the pattern changes with solvent density or pressure.

Domain Formation in RTIL: Results of our molecular dynamic simulations reveal that self-organization of the room temperature ionic liquid (RTIL) solvent molecules, which creates non-ionic and ionic pockets in RTIL, becomes more significant as the alkyl chain length of the RTIL increases. Apart from observing the self–organisation by structural analysis of the simulated system, preferential solvation of polar and non-polar molecules in the RTIL clearly demonstrates that the polar and non-polar domains are created in the RTIL [27]. With increasing tail length of the RTIL (see Fig.10), alkyl-alkyl (ct-ct) RDF peak increases as a result of nonpolar domain formation by the alkyl chains of the RTIL. The RDFs (Fig.11) (a)-(d) of the nonpolar pyrene (Py) molecules indicates that Py is solvated by the nonpolar chain of the RTIL and charged solute Methyl Viologen (MV^{2+}) is surrounded by the counterions BF_4^-. Therefore the preferential solvation of the Py and MV^{2+} indirectly
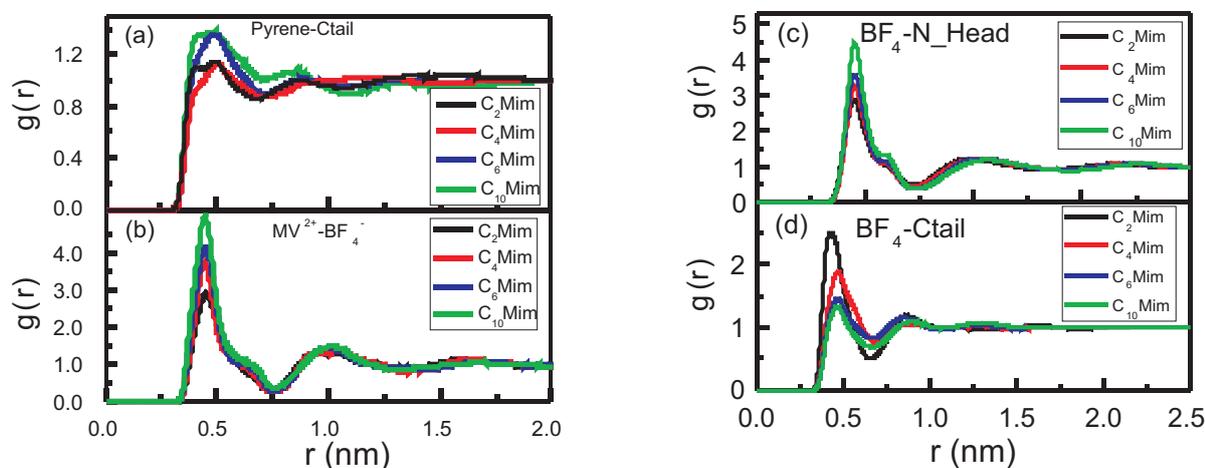
corroborates that there is microdomain formation in the RTIL. These simulation results are in consonance with the experimental results [27].

3.4 Bio-Inspired Research

Many of our activities are directed towards understanding the behaviour of water [28] and aqueous solutions [29-32] containing small biological molecules and their action towards bio macromolecules like proteins. Apart from that, large molecular simulations have been used to understand protein drug interaction and structure of viral capsid, which will help in designing new drugs.

TBA & TMAO Hydration and Action: Despite structural similarity and common amphiphilic nature of the two organic molecules, tert-butyl-alcohol (TBA) and trimethylamine-N-oxide (TMAO), their action toward protein structure and stability and their behaviour in aqueous solutions are strikingly different. In the aqueous solution, TBA forms aggregates at a very moderate concentration, whereas TMAO does not. In spite of a large number of experimental as well as simulation studies, many intriguing issues about the behaviour of these two aqueous solutions are either not properly addressed or not addressed at all. We have used extensive MD simulations and novel analyses to address many such issues and also the nature of their interaction with the protein moiety [29]. The Root-mean-square deviation (RMSD) of the Trp-cage mini protein as shown in Fig.12 clearly demonstrates that the TBA helps in denaturation and TMAO tries to keep the folded configuration intact.

Further, TBA molecules interact and get accumulated around the backbone, whereas TMAO prefers to stay away from the backbone (Fig.13). Further analysis (Fig.14) shows accumulation of TBA around the backbone is through hydrophilic OH group. This study also clarifies many points on the behaviour of the aqueous solution. It explains that the anomalous change in the peak height of the RDF as a function of TBA concentration is not really due to anomalous aggregation as predicted in a previous study [30]. The small pre-peak in the TBA-TBA RDF is demonstrated to be exclusively due to inter TBA H-bond formation. One of the most striking observation in the present study is the presence of heterogeneity even in a very dilute (X_{TBA}=0.04) TBA solution. However, TMAO solution is found to be homogeneous [29].

Fig.11: Radial distribution functions of the (a) tail carbon atom of the alkyl chain around the Py molecule and (b) BF_4^- anion around MV^{2+} ion (c)N-atoms of the head group of the cation of the RTIL around the BF_4^- anions (d) tail carbon atom of the alkyl chain of RTIL around the BF_4^--anions.
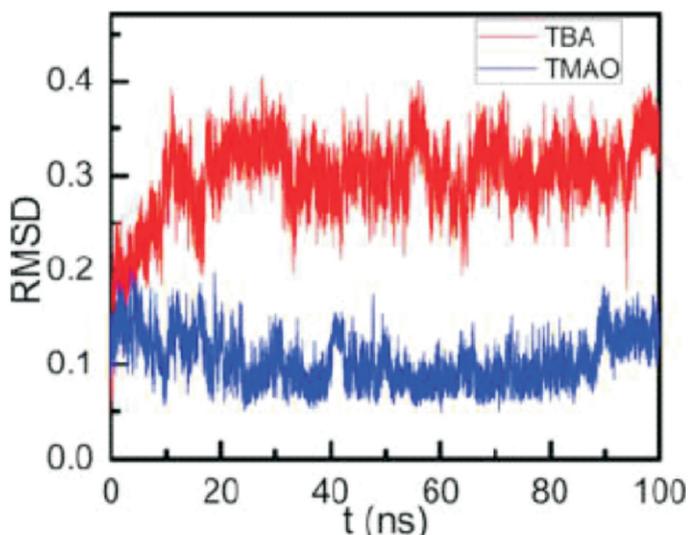
Fig.12: RMSD of the backbone of the Trp-cage miniprotein with respect to initial PDB structure as a function of time in aqueous solutions of TBA (red lines) and TMAO (blue lines).

Fig.13: RDF of the central C atoms of TBA (red line) and the central N atoms of TMAO (blue line) around the backbone sites of the Trp-cage miniprotein.

Fig.14: (a) RDF of hydrophilic atoms of TBA and of the TMAO and (b) RDF of the hydrophobic methyl groups of TBA (red line) and TMAO (blue line) around the backbone sites of the Trp-cage miniprotein.

Fig.15: Distribution of water- water (upper panel in each figure) and water- urea (lower panel in each figure) hydrogen bonds at different urea concentrations.

Is Urea Chaotropic?

In another study, using MD simulations we have resolved [31] a long standing questing question: Is urea chaotropic? Through careful analysis, we are able to show that if we account for the fact that urea can also be a neighbour in a concentrated solution of urea, the urea really does not break the water structure, it just replaces one or more water neighbours of a central water molecule. It is shown that in a dilute urea solution (see left panel of Fig.15), most of the water molecules are four hydrogen bonded, but in a concentrated solution (see right panel), most of them are three H-bonded. On the other hand, population of water-urea H-bonds is increased at higher concentrations (see the right panel).

Guanidinium ion and Protein Denaturation: Like TBA, TMAO and urea, guanidinium chloride (GdmCl) is also a biologically important molecule and acts as a protein denaturant. There are reports that Gdm moieties forms aggregate in solution. Using MD simulation, we have investigated [32] the intricacies of aggregate formation and its mode of action on protein to get idea about the mechanism of denaturation. The Parallel stacking of the two Gdm+ moieties in
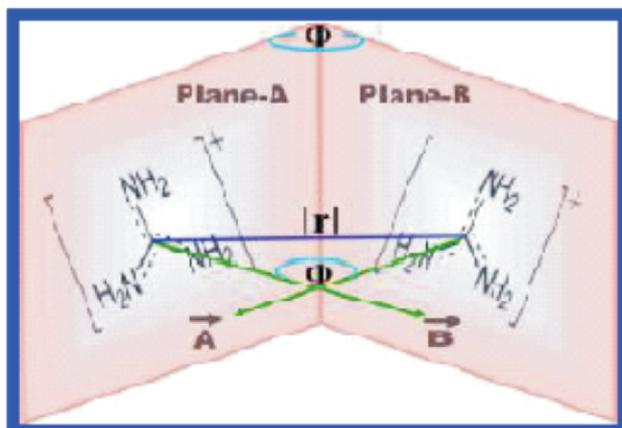
Fig.16: Schematic representation of two molecular planes of guanidinium ions inclined at an angle Φ.
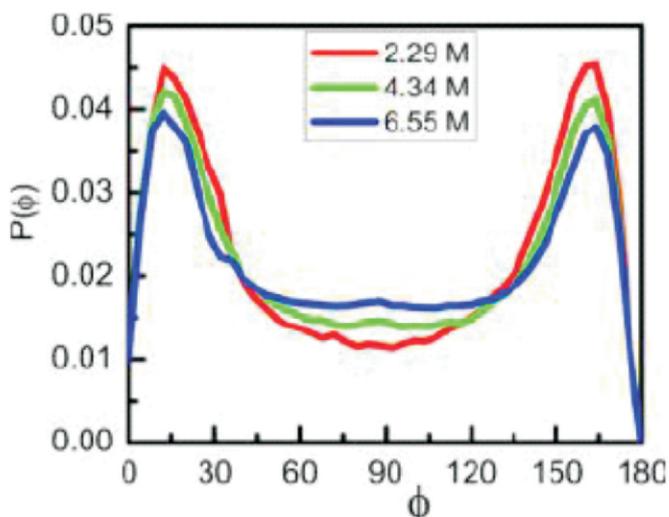
Fig.17: Distributions P(Φ) of the angles Φ between two guanidinium molecular planes.
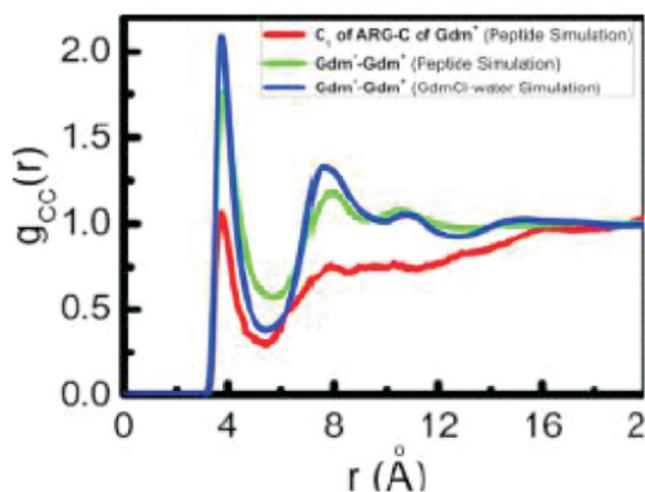
Fig.18: RDF of the Gdm$^+$ moiety around ARG side chain of the protein, Gdm$^+$ around Gdm$^+$ in the protein- GdmCl- water, and GdmCl- water without protein) systems.
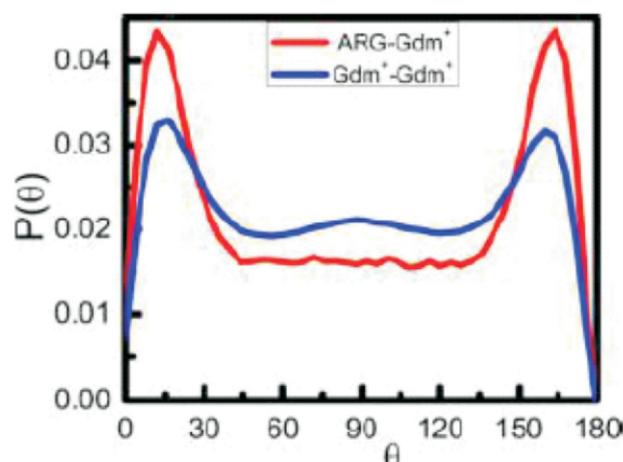
Fig.19: Distributions P(θ) of the angles between Gdm$^+$ moiety and the molecular plane of the ARG side chain of the protein.

concentrated GdmCl binary solution (Figs.16&17) has been observed. The larger peak height of the ARG-Gdm RDF (Fig.18) as compared to other carbon atoms of the protein indicates accumulation of Gdm$^+$ ions around the arginine side chain. Further analysis showed (Fig.19) that the Gdm moiety stacks around structurally similar ARG side chain of the protein [32]. Therefore, parallel staking of the Gdm$^+$ and ARG moieties is the mode by which Gdm$^+$ attacks the protein backbone.

Protein-Drug Interaction: In an effort to understand how a drug molecule accomplish its task interacting with protein molecules, several large-scale computations were performed and compared the efficacy of existing oxime drug molecules towards recovery of free nerve enzyme, acetylcholinesterase from the organophosporous (chemical warfare) intoxications. Present group is instrumental in developing fluorinated drugs for the reactivation of inactivated acetylcholinesterase in both periphery and central nervous system [33]. The effect of heavy water on thermo-stabilization of liquid pharmaceuticals and the inclusion of kinetic isotope effect (Fig.20) are accomplished by carrying out replica exchange MD simulations [34]. Viruses are the simplest

biological systems, essentially composed of a protein shell or capsid that encloses the genetic material. Structural changes in a capsid due to thermal fluctuations play a major role in the deliverance sequel of the confined material and therefore its characterization is essential for providing fresh insights into antiviral/nanomaterial strategies. We have therefore, calculated the heat induced changes in the properties of an empty minute virus of mice particle using large-scale (3.0 million atoms) MD simulations in a year time. The findings have implications in the development of therapeutic inhibitors of viral shells.

Development of Theoretical Methodologies and Computer Codes: Low-Energy Free-Electron Induced Chemistry is a new paradigm in chemical reaction. Negative ion resonance states play a crucial role [35] in low-energy free-electron-induced biomolecular modifications and in the free-electron controlled molecular reactions [36]. The electronic structure and the reaction mechanism of negative ion resonance states are only poorly understood. In fact, one of the most important challenges to current electronic structure theory is the computation of negative ion resonance states. As a major step towards this direction, we have
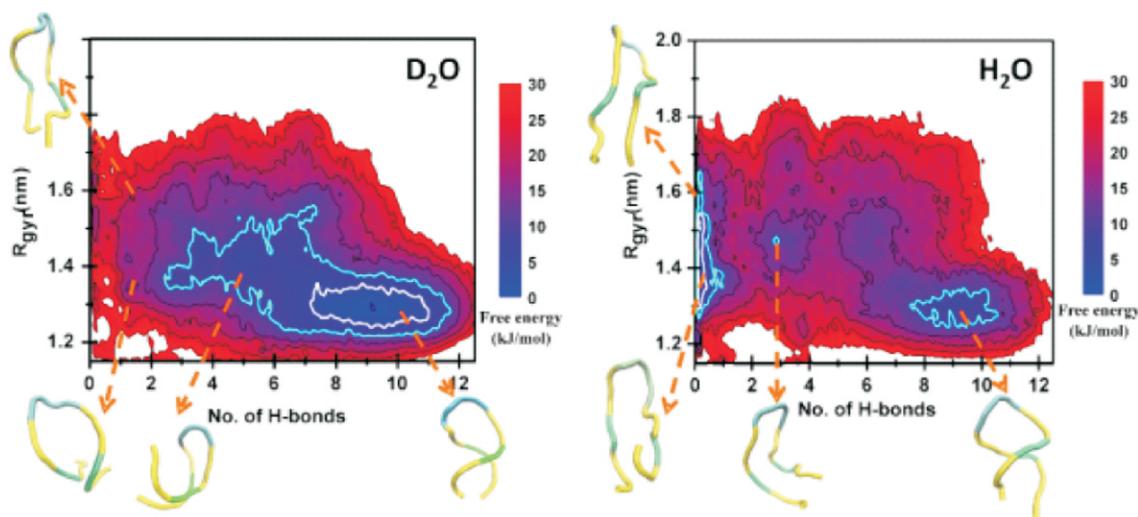
Fig.20: Free-energy surface of polio viral RNA hairpin at 300 K in D_2O and in H_2O.

developed and implemented new state-of-the-art ab initio quantum chemical methods which offer the most accurate computation of negative ion resonances. We have demonstrated [35-36] that the chemical reactions can be initiated, controlled and catalyzed through negative ion resonance states.

Implementations of New Features in DIRAC Code: We describe the theoretical studies [37-38] of symmetry violating properties which are relevant for the search of electron electric dipole moment (EDM) and to probe physics beyond the standard model (SM) of particle physics. In explaining matter-antimatter asymmetry of the universe, there must be CP violation (where C and P mean charge conjugation and parity invariance, respectively). The main emphasis of our research lies in searching for CP violation in atomic and molecular systems. Observation of permanent EDM and magnetic quadrupole moment (MQM) [37] of a system is a signature of simultaneous violation of CP according to the CPT theorem. We are involved in developing highly accurate wave function based relativistic methods for computing the accurate value of CP-odd molecular parameters. In this context, the group has developed many new codes/modules which are integrated with the DIRAC program package and interfaced DIRAC code [39] with many in-house developed advanced computer codes.

Concluding Remarks

In this article, a brief account of varieties of topics requiring quantum to mesoscopic frameworks as carried out in this group has been presented. It shows the usefulness and applicability of modern theoretical and computational chemical physics in solving complex chemical problems. With the advent of newer formalisms and methods, theoretical and computational chemistry will become an indispensible tool for every research group in the world. Amalgamation of state of the art computing technique like machine learning with the existing theoretical and computational tools will bring new era in this field. An application of such machine learning technique in hydrogen storage problem is in progress in our group [40].

Corresponding Author*

Niharendu Choudhury (nihcho@barc.gov.in)

References

[1] J.C. Schön, M. Jansen, *Angew. Chem. Int. Ed.*, 1996, **35**, 1286.

[2] M. Praprotnik, L. Delle Site, K. Kremer, *Annu. Rev. Phys. Chem.*,2008, **59**, 545-571; Peter, C.;Kremer, K.,*Soft Matter*, 2009, **5**, 4357-4366. DOI: 10.1039/b912027k.

[3] S. Ahlawat, K. Srinivasu, A. Biswas, N. Choudhury, *Comput. Mater.Sci.*, 2019, **170**, 109167.

[4]   S. Ahlawat, K. Srinivasu, A. Biswas, N. Choudhury, *Phys. Chem. Chem. Phys.*, 2021, **23**, 8689-8704.

[5] B. Sadhu, M. Sundararajan, T. Bandyopadhyay, *Inorg. Chem.*, 2016, **55**, 598.

[6] X. Ye, S. Cui, V. de Almeida, B. Khomami, *J. Phys. Chem. B*, 2009, **113**, 9852-9862.

[7] G.R. Choppin, M.K. Khankhasayev, Chemical Separation Technologies and Related Methods of Nuclear Waste Management: Applications, Problems, and Research Needs, First Edition. Vol. **320**, Springer, New York, 1999.

[8] M. Chopra, N. Choudhury, *J. Phys. Chem. B,* 2014, **118**, 14373-14381.

[9] M. Chopra, N. Choudhury, *Phys. Chem. Chem. Phys.*, 2015, **17**, 27840-27850.

[10] M. Chopra, N. Choudhury, *J. Mol. Liq.*, 2016, **224**, 599-606.

[11] M. Chopra, N. Choudhury, *Chem. Phys.*, 2017, **495**, 48-58.

[12] M. Chopra, N. Choudhury, *J. Phys. Chem. C,* 2013, **117**, 18398-18405.

[13] M. Chopra, N. Choudhury, *J. Mol. Liq.*, 2019, **294**, 111569.

[14] T. Vazhappilly, T.K. Ghanty, B.N. Jagatap, *J. Phys. Chem. C,* 2016, **120**, 10968.

[15] S. Kancharlapalli, S. Natarajan, T.K. Ghanty, *J. Phys. Chem. C,* 2019, 123, 27531-27541.

[16] Vazhappilly, T.; Pathak, A. K., *J. Nucl. Mat.*, 2019, **519**, 128.

[17] Vazhappilly, T.; Pathak, A. K., *Comput. Mater.Sci.*, 2020, **185**, 109933.

[18] K. Srinivasu, B. Modak, T.K. Ghanty, *J. Nucl. Mater.*, 2018, **510**, 360-365.

[19] B. Modak, K. Ghoshal, K. Srinivasu, T.K. Ghanty, *J. Phys. Chem. Solids* 2020, **136**, 109179.

[20] K. Srinivasu, S.K Ghosh, *J. Mater. Chem. A,* 2015, **3**, 23011-23016.

[21] B. Modak, P. Modak, S.K. Ghosh, *Phys. Chem. Chem. Phys.*, 2018, **20**, 20078.

[22] K. Srinivasu, S.K. Ghosh, *J. Phys. Chem. C,* 2012, **116**, 25184-25189.

[23] P. Banrjee, R. Thapa, A. Rajkamal, K.R.S. Chandrakumar, G.P. Das, *Int. J. Hydrogen. Ene.*, 2019, **44**, 23196-23209.

[24] P. Banerjee, K.R.S. Chandrakumar, G.P. Das, *Chem. Phys.*, 2016, **469-470**, 123-131.

[25] S. Pantawane, D. Bandyopadhyay, N. Choudhury, *ACS Omega,* 2018, **3**, 1060- 1068.

[26] S. Pant, T. Gera, N. Choudhury, *J. Chem. Phys.* 2013, **139**, 244505.

[27] B. Manna, D. Bandyopadhyay, N. Choudhury, D.K. Palit, *J. Photochem. and Photobio. A: Chemistry,* 2018, **356**, 81-91.

[28] D. Bandyopadhyay, S. Mohan, S.K. Ghosh, N. Choudhury, *J. Phys. Chem. B,* 2013, **117**, 8831.

[29] D. Bandyopadhyay, Y. Kamble, N. Choudhury, *J. Phys. Chem. B,* 2018, **122**, 8220-8232.

[30] S. Banerjee, J. Furtado, B. Bagchi, *J. Chem. Phys.*, 2014, **140**, 194502.

[31] D. Bandyopadhyay, S. Mohan, S.K. Ghosh, N. Choudhury, *J. Phys. Chem. B,* 2014, **118**, 11757.

[32] D. Bandyopadhyay, K. Bhanja, S. Mohan, S.K. Ghosh, N. Choudhury, *J. Phys. Chem. B,* 2015, **119**, 11262-11274.

[33] A.K. Pathak, T. Bandyopadhyay, *J. Phys. Chem. B,* 2018, **122**, 3876-3888.

[34] A. K. Pathak, T. Bandyopadhyay, *J. Chem. Phys.*, 2017, **146**, 165104.

[35] D. Davis, Y. Sajeev. *Chem. Comm.*, 2020, **56**, 14625-14628.

[36.] Y. Sajeev, *Mol. Phys.*, 2019, **117**, 2162-2166.

[37] T. Fleig, M.K. Nayak, M.G. Kozlov, *Phys. Rev. A,* 2016, **93**, 012505.

[38] S. Sasmal, H. Pathak, M.K. Nayak, N. Vaval, S. Pal, *Phys. Rev. A,* 2016, **93**, 062506.

[39] DIRAC, a relativistic ab initio electronic structure program, DIRAC19 (2019), written by A.S.P. Gomes *et al.* (available at http://dx.doi.org/10.5281/zenodo.3572669, see also http://www.diracprogram.org).

[40] K. Srinivasu, A. Gopalan, M. Haranczyk, R.Q. Snurr, *J. Chem. Theory Comput.*, 2021, **17**, 3052-3064.

Multi-component Amorphous Glasses: Effect of Glass Compositions

Pooja Sahu[1,2], *Sk. Musharaf Ali[1,2], K.T. Shenoy[1], A. Arvind[3], G. Sugilal[3], C.P. Kaushik[3]

[1]Chemical Engineering Division, Bhabha Atomic Research Centre, Mumbai-400085, India
[2]Homi Bhabha National Institute, Mumbai-400094, India
[3]Nuclear Recycle Group, Bhabha Atomic Research Centre, Mumbai-400085, India

ABSTRACT

Selection of suitable glass composition for vitrification of high-level radioactive waste (HLWs) is one of the major challenges in nuclear waste reprocessing. Atomic and molecular level understanding can help in preliminary screening and thus reduce the dependency to some extent on tedious experimental procedures. In that context, extensive molecular dynamics (MD) have been carried out, which provides microscopic understanding of the glass structure and phenomena associated with the change in glass compositions. A detailed view of local structure and medium range connectivity has been explored. Results showed a good match of evaluated macroscopic glass parameters: density (ρ), glass transition temperature (T_g) and thermal expansion coefficient (TEC) with the experiments. The presented results might be of great scientific use for future glasses in various applications including nuclear waste immobilization.

Keywords: Sodium Borosilicate Glass, Molecular Dynamics Simulation, Glass Transition Temperature, Bridging Oxygen, Structure Factor, Diffusion, Chemical Durability.

Introduction

Glass is an amorphous solid with a wide spectrum of applications in electronic display and devices, cover glasses and other valuable domestic/laboratory wares[1]. The popularity of borosilicate glasses in nuclear waste immobilization[2,3] arises due to a combination of useful material properties including high chemical durability, resistance to crystallization/devitrification and the ability to accommodate a wide diversity of cations within its structure. In addition, borosilicate glasses can be produced in large quantities in remotely handled plant environments owing to the maturity of glass production technology. Each individual component of glass plays a significant role in deciding the glass property and strength[4]. Even a minor change in composition might lead to a substantial difference in glass properties. Basic understanding about the macroscopic properties of the glasses is pursued after the microscopic structure at the atomic/molecular level. Earlier Boron-11 NMR has been widely applied to study the structure of borosilicate glasses[5-7]. Besides NMR, high temperature Raman scattering spectroscopy has also been used by Osipov et al.[8] to examine the stability of amorphous nature in glass and melts. A

significant contribution has been made by Yang et al.[9] in identifying the structure and dissolution properties of boro-phospho-silicate glasses using Solid-State NMR as well as molecular dynamics (MD) Simulations[10,11]. Constituents such as silica and boric oxide are the major network formers. In addition to the role of network formers, the physical properties of vitrified glass are also known to have clear dependence on the nature and quantity of the added alkali modifiers. In particular, the dependence on the nature of alkali modifiers originates from structural variation. Though numerous experimental as well as simulation studies report the dependence of glass properties on the nature and quantity of the added alkali modifiers, however, studies by Stevensson et al.[12] showed that the effects introduced by the nature of alkali oxides are negligible. Such disagreements drive the further research on the glass structure and properties with varied compositions. Though severe structural changes in B-bearing glasses has been observed with variation in composition, temperature or pressure, however, despite of popularity, the long long-lasting challenges of microscopic structural evidence are yet to be explored for these glasses. In contradiction to 'Loewenstein avoidance rule', Yu et al.[13] showed the abundant presence of BO_4-BO_4 motifs in alkali/alkaline-earth borosilicate glasses. The relative propensity of finding P-O-Q (where P /and/or Q = Si, B3, and B4; where B3 and B4 respectively represent the BO_3 trigonal structural units and BO_4- tetrahedral structural units of boron) links was observed to be composition dependent. Surprisingly, for few composition of glasses, especially with B4 fraction higher than 0.6, relative propensity of B4-O-B4 linking was higher than B3-O-B3, which contracts the general thought of 'B[4] avoidance rule' as predicted by many theories[14,15], hereby, demand for furthermore studies. Besides the experimental and MD studies, numerous efforts were made by many theoretical models established by Phillips et al.[16], Williams and Scott et al.[17], Soga et al.[18], and Bridge et al.[19] in this direction. However, most of these models consider only first neighbour influence and therefore are restricted to find the structural changes within certain limits only.

Considering all this, the present study is dedicated to understand the short-range order and medium range connectivity of borosilicate glasses. The correlations between microscopic structure and macroscopic glass properties such as glass transition temperature, thermal expansion coefficient and mechanical integrity has been established. In addition, the diffusion dynamics of component species has been determined, which can be utilized to demonstrate the long-term leaching ability and radiation stability of these glasses. The MD results provide the reasoning for the relative

order of observed macroscopic properties from microscopic point of view. A detailed view of local structure and medium range connectivity has been explored.

Computational methods

The present simulations were conducted with LAMMPS package[20]. The interaction between atoms was simulated using the combination of Buckingham potential (for short-range interactions and Coulomb potential (for long-range interactions, expression, together known as Van Beest, Kramer, Van Santen (BKS) potential model[21].

$$U_{vdw} = \sum_{i=1}^{N}\sum_{j>i}^{N} A_{ij}e^{-r_{ij}/\rho_{ij}} - \frac{C_{ij}}{r_{ij}^6} \qquad (1)$$

$$U_{coul} = \frac{q_i q_j}{4\pi\varepsilon r_{ij}} \qquad (2)$$

The parameters ρ_{ij}, A_{ij} and C_{ij} control the narrowness of potential model. The separation between the ith and j^{th} atom, having partial charge q_i and q_i respectively is represented by r_{ij} and ε is the permittivity. The forcefield parameters of simulated glasses can be found in our previous papers[22, 23].

Particle-Particle-Particle Mesh (PPPM) method[24] was employed to account for the long-range interactions. The partial charge on the atoms were taken to be composition dependent[25]. All systems were initially heated at 5000 K using the canonical (NVT) ensemble for 10 ns in order to remove the memory effects. This was followed by NVT quenching at a rate of 0.4 K/ps. The systems were furthermore equilibrated for 20 ns dynamics using the isothermal- isobaric ensemble (NPT)[26] at 300 K and P = 1 atm. Further, the production runs were performed for 30 ns, and the generated data was utilized for the analysis of structural and dynamical properties of simulated glass, with methods as discussed in our previous articles[22, 23].

Results and discussion

Pure Glass Matrix of SiO₂ and B₂O₃

First, the pure glass matrix of major network formers: SiO_2 and B_2O_3 were simulated, images shown in Fig.1(a). The density was measured to be 2.38 g/cm^3 for SiO_2 and 1.82 g/cm^3 for B_2O_3, which is close to respective experimental densities. The radial distribution function (RDF) showed the peak positions at 1.62 Å, 2.58 Å and 3.17 Å respectively for Si-O, O-O and Si-Si in SiO_2 and at 1.35 Å, 2.37Å and 2.57 Å corresponding to B-O, O-O and B-B in B_2O_3.

The coordination number, and bond/angle distributions are shown in Fig.1(b, c). In sequence, the structure factor in Fig.1(d) was estimated in order to determine the intermediate range order in these glasses. SiO_2 showed the first peak at ~2.15-2.25 Å^{-1} and then a second peak at around 5.45 Å^{-1}, while, B_2O_3 showed first peak at 2.4-2.45 Å^{-1} and a negative dip at 3.0 Å^{-1}. The first sharp diffraction peak (FSDP) was noted at 1.2-1.3 Å^{-1} for two connected SiO_4 tetrahedrals and at 1.45-1.65 Å^{-1} for two connected trigonal boron (BO_3) units.

Furthermore, the characteristic vibration spectrum VDOS of SiO_2 shows a flat peak at 200-600 cm^{-1}, and another peak in between ~1050-1070 cm^{-1} concerning intra-tetrahedral excitations. VDOS spectrum of B_2O_3 shows four characteristic peaks at 130 cm^{-1}, 670

(a)
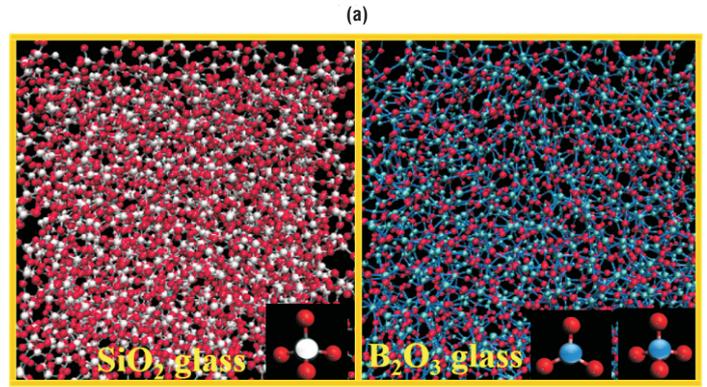
Fig.1(a): Snapshot for structure of amorphous SiO_2 and amorphous B_2O_3 (Color code: Si: white, O: red, B: blue) Inset images shows SiO_4 tetrahedra, BO_3 planer structure and BO_4- tetrahedral unit.
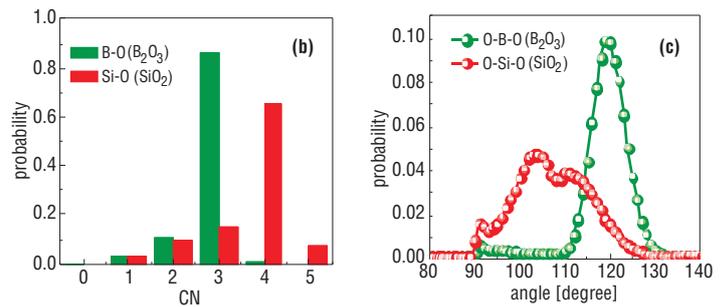
Fig.1(b): coordination distribution profile and **(c)** angle distribution profile for SiO_2 and B_2O_3 glass.
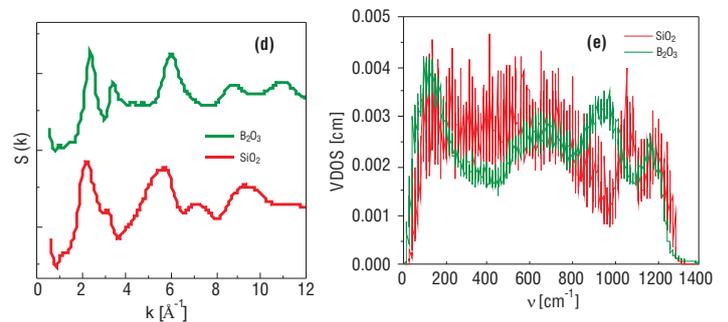
Fig.1(d): Total structure factor and **(e)** vibration density of state (VDOS) for SiO_2 and B_2O_3.

cm^{-1}, 960 cm^{-1} and 1180 cm^{-1} (Fig.1(e)). The first two peaks are related to vibration of B atoms[27], while higher peaks represent the vibration of oxygen atoms connected to trigonal coordinated boron. Essentially, the selected potential parameters well reproduce the experimental VDOS and earlier reported data[27,28].

Binary borosilicate glass

The structural models of borosilicate glass were prepared using different composition of SiO_2 and B_2O_3 in the matrix. The results in Fig.2(a) show that the density of glass was increased from 1.75 g/cm^3 to 2.14 g/cm^3, while increase in SiO_2 concentration from 10% to 70%. Also, it was noticed from Fig.2(b) that the increase in silica content leads to increased conversion of planer BO_3 (B3) units into BO_4- (B4) tetrahedrals. In particular, the network connection becomes stronger with higher concentration of SiO_2 in the glass matrix.
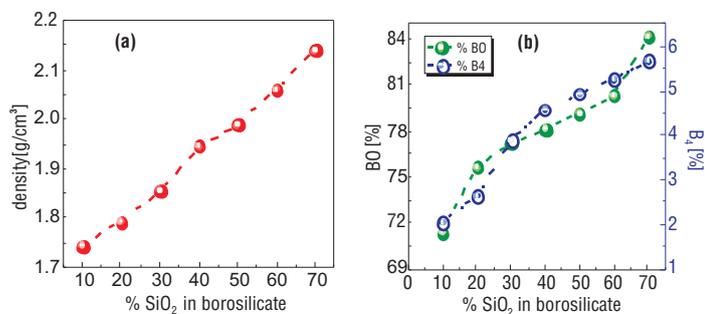
Fig.2(a): density and **(b)** bridging oxygen atoms (BO) (left Y axis) and BO$_4$- (B4) units (right Y axis) in borosilicate glass matrix.

Effect of Alkali addition: sodium silicate & sodium borate

The BOs were reduced with increasing Na$_2$O content (Fig.3(a)), which reflect that the excess alkali may lead to devitrification of glass and therefore need to be avoided. The density of sodium borate was seen to be increasing with the increase in Na$_2$O concentration till 40%, thereafter a decrease in density was observed with further addition of Na$_2$O as shown in Fig.3(b). In precise, the initially added sodium ions (for Na$_2$O < 40%) were seen to reside within the cavities formed by boroxyl rings, on the contrary, furthermore added sodium ions were observed to participate as network modifier. Occupancy of sodium ions in the interstitial positions causes larger increase in mass than the volume of glass matrix, therefore leads to increasing density with Na$_2$O concentration smaller than 40%. At the same time, the presence of alkali ions within the boroxyl cavities provides the charge compensation to BO$_4$- tetrahedrals and so contribute in BO$_3$ BO$_4$- conversion. As a results, the fraction of B4 in sodium borate glass matrix was observed to be increased with increase in Na$_2$O for concentration smaller than 40%. Such an altering behaviour of sodium ions in sodium borate glass was also confirmed by the angle distribution profiles shown in Fig.3(c). Akin to sodium silicate matrix, the BOs were reduced with increase in alkali concentration in the sodium-borate glass as shown in Fig.3(d).
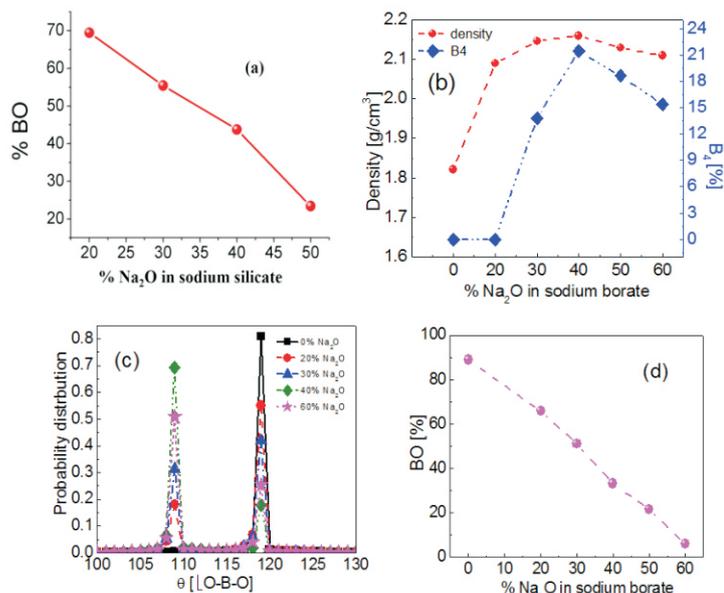
Fig.3(a): Number of BO in sodium silicate glass **(b)** density (left Y axis) and B4 units (right Y axis) in sodium borate glass matrix, **(c)** angle distribution profile for O-B-O in sodium borate glass matrix and **(d)** number of BO in sodium borate glass matrix.

Sodium borosilicate glass matrix (NBS)

Furthermore, the NBS glass with composition 21SiO$_2$.6B$_2$O$_3$.7Na$_2$O i.e. 59.70% SiO$_2$, 19.76% B$_2$O$_3$ and 20.53 %Na$_2$O was simulated, structure shown in Fig.4 (a). The density was measured to be 2.42 g/cm^3, which was in good agreement with the experimental density (*2.4 g/cm^3). The coordination and angle distribution profiles are shown in Fig.4(b, c) respectively. The CN was measured to be 4.0, 3.8 and 10.28 for Si-O, B-O and Na-O respectively. Also, the angle distribution profiles show tetrahedral coordination of oxygen to Si as peak for O-Si-O was obtained at 109.4^o. Two peaks were noticed for O-B-O at 109.4^o as well as at 120°, indicating tetrahedral coordination and trigonal coordination of B with O. The relative concentration of BO$_4$- and BO$_3$ was estimated to be ~63% and 29% respectively. The peaks for angles Si-O-Si, B-O-B and O-Na-O were found to be rather broad in nature, with peak position of 146°, 138° and 151° respectively, which is in good agreement with the available data[29].
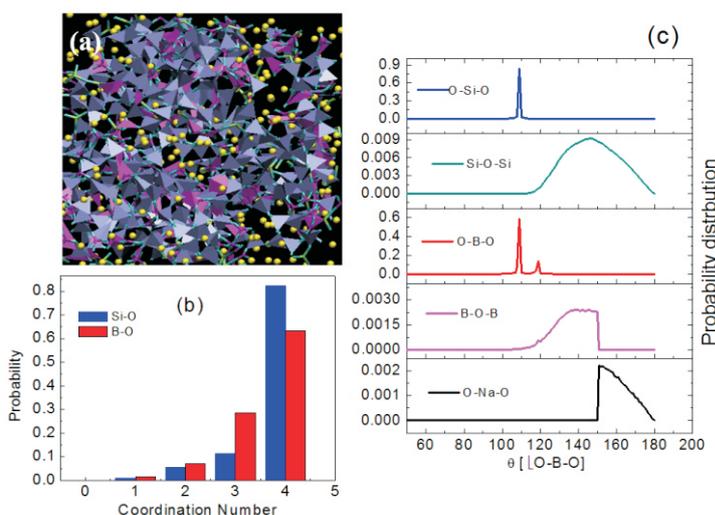
Fig.4(a): Snapshot for sodium borosilicate glass matrix [SiO$_4$ tetrahedrals shown blue, BO$_3$ & BO$_4$- units purple and sodium ions are shown yellow] **(b)** coordination number distribution and **(c)** angle distribution in sodium borosilicate (NBS) glass matrix.
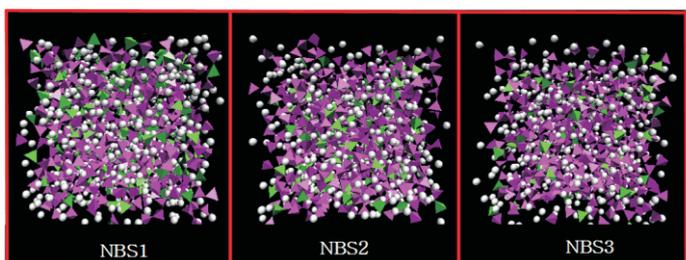
Fig.5: Snapshot for sodium borosilicate glass matrix SiO$_4$ tetrahedrals shown purple, BO$_3$ & BO$_4$- units green.

Table 1. Composition of NBS glasses

	N$_{SiO_2}$	N$_{B_2O_3}$	N$_{Na_2O}$	N$_{total}$
NBS1	720	262	328	4454
NBS2	780	260	260	4420
NBS3	700	350	260	4630

Subsequently, the composition dependence was tested by simulating three compositions of NBS glass matrix, named as NBS1, NBS2, and NBS3, composition shown in Table 1 and respective snapshots in Fig.5.

Table 2. Density, Number of Bridging Oxygens (BO), Non-Bridging Oxygen (NBO) and BO_4^- (B4) fraction in simulated NBS glasses.

	Density [g.cm⁻³]	% BO	% NBO	% B4
NBS1	2.273	80.23	19.77	57.44
NBS2	2.275	83.77	16.23	58.26
NBS3	2.269	82.43	17.57	48.42

Table 3. RDF First Peak Positions (r_{max}) and Coordination Number (CN) for sodium borosilicate glasses.

Pair	NBS1		NBS2		NBS3	
	r_{max}	CN	r_{max}	CN	r_{max}	CN
Si-O	1.61	4.00	1.61	4.00	1.61	4.0 0
B-O	1.62	3.67	1.54	3.63	1.62	3.56
Na-O	2.5	5.67	2.49	5.54	2.5	6.00
Si-Si	3.19	1.77	3.15	2.03	3.21	1.15
Si-B	3.09	1.94	3.09	1.82	3.13	2.81
B-B	3.05	1.22	3.03	1.23	3.14	1.47

The results in Table.2 show that the NBS2 had higher density than NBS1, as R and K both increase (with $Na_2O<40\%$) while going from NBS1 to NBS2. Similar to this, NBS1 having higher R and K than NBS3, corresponded to higher density for NBS1 than NBS3. The MD estimated trend for density are in well agreement with the experimental observations[22]. Furthermore, the results show that nearly 80% oxygen atoms are dedicated to form bridging oxygen, whereas remaining 20% oxygen atoms participate as non-bridging oxygen atoms. To be noted, both R and K play in reverse direction for availability of BOs. The highest R for NBS1 correspond to lowest BO and highest K for NBS2 contribute to maximum BO for NBS2. In particular, the highest $Na_2O\%$ for NBS1 correspond to minimum number of BO available for NBS1. On the other hand, for similar content of Na_2O for NBS2 and NBS3, availability of BO is dominated by $\%SiO_2$ in the glass. Interestingly, the number of BO_4 units in the glass matrix seem to follow the order as K i.e. NBS2>NBS1>NBS3. Additionally, the differences in short-range order of these glasses was determined in terms of minor changes in radial distribution functions and bond/angle distribution profiles. The average CN for atomic pairs is shown in Table.3.

In addition, the connectivity within structural network was noted in order Si-O-B4 > Si-O-Si > Si-O-B3 > B3-O-B4 > B4-O-B4 > B3-O-B3 for NBS1 and NBS2, whereas Si-O-B4 > Si-O-B3 > Si-O-Si > B3-O-B4 > B4-O-B4 > B3-O-B3 for NBS3. The results show that Si-O-B4 connections are favored over Si-O-Si connections. NBS3, having higher B_2O_3 content compared to NBS1 and NBS2, showed preferred connection for Si-O-B3 over Si-O-Si, on the other hand, for NBS1 and NBS2, the Si-O-Si connections were dominated over

Si-O-B3. On contrary to "B[4] avoidance" rule, the present study showed abundant presence of B4-O-B4 units. The results evidence that the intermixing B3-O-B4 connections were found to be preferred over either of B3-O-B3 or B4-O-B4 connections. Also, for the simulated glasses, the B4-O-B4 linking was preferred over B3-O-B3. In particular, the relative population of these units depends on the availability of B_2O_3 and SiO_2 content[13]. For NBO, the order was Si-NBO > B3-NBO > B4-NBO, reflecting that the negatively charged BO_4^- tetrahedrals usually accommodate least NBO species[12].

Furthermore, the fabrication easiness was measured in terms of glass transition temperature (Fig.6). As expected, the highest SiO_2 content in NBS2 corresponded to maximum T_g, on the other hand, the highest B_2O_3 content in NBS3 lead to lowest T_g (see Table.4). NBS1 showed the highest TEC due to the highest Na_2O content, while high B_2O_3 NBS3 was responsible for a higher TEC of NBS3 than NBS2.
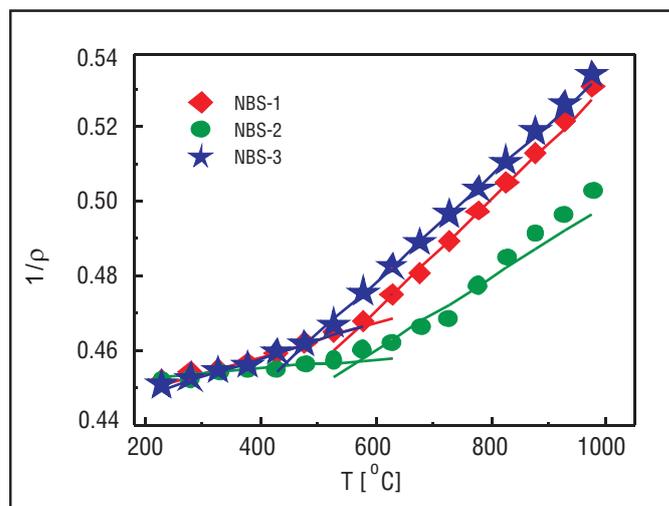
Fig.6: Inverse density vs. temperature profile for simulated NBS glasses.

Table 4. Glass Transition Temperature (T_g) and Thermal Expansion Coefficient (TEC) of simulated glasses.

	NBS1	NBS2	NBS3
$T_g(^{0}C)$	567.63	572.31	481.79
TEC (x 10^{-5})/^{0}C	1.13	0.73	1.05

Additionally, the mechanical strength of simulated glasses was demonstrated in terms of stress-strain relationship shown in Fig.7. The stress-strain profiles show a narrow span of plasticity before brittle fracture. The elasticity of these glasses was measured in terms of Young modulus (Y), estimated to be 40.65±1.94, 42.74±1.72, and 39.66±1.19 for NBS1, NBS2 and NBS3 respectively. The highest Y of NBS2 is owned by the highest SiO_2 and low B_2O_3 content. The modifier rich NBS1 and B_2O_3 rich NBS3 show nearly similar Y. Further, plastic nature of glass was determined in terms of yield stress, estimated to be 1.92GPa, 2.15GPa and 2.51GPa for NBS1, NBS2 and NBS3 respectively. The lowest yield stress for NBS1 is in accordance to the presence of highest Na_2O content. On the other hand, the highest yield strength for NBS3, seems to be linked with the maximum B_2O_3.
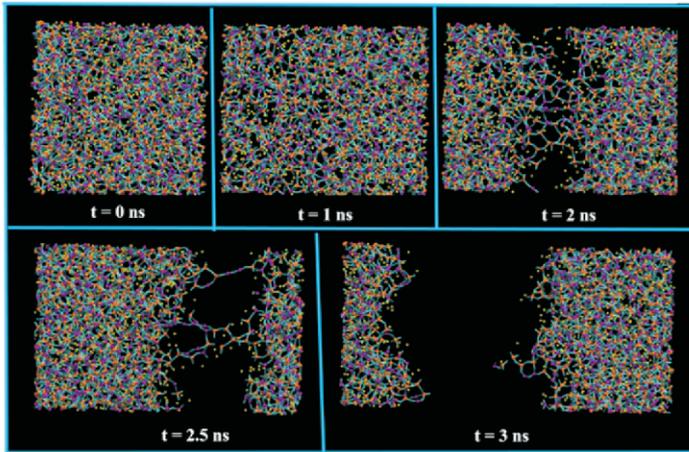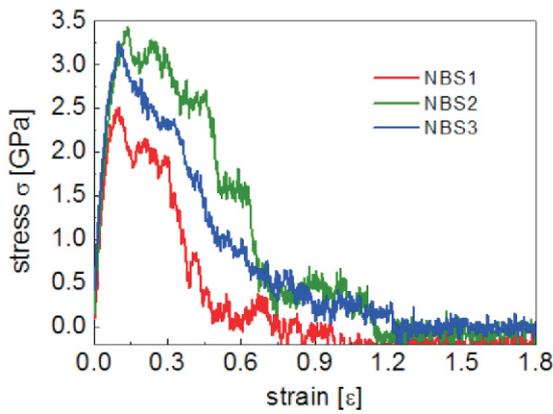
Fig.7: Stress-strain diagram and Snapshots for deformation of NBS1 glass matrix.
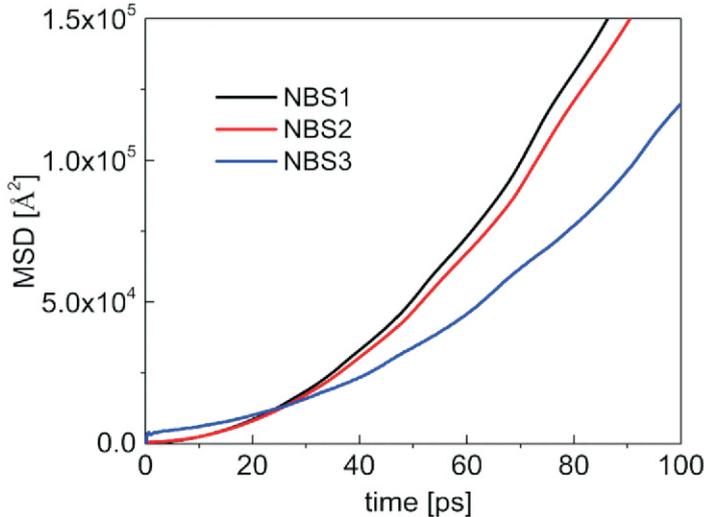
Fig.8: Mean Square Displacement (MSD) profile for sodium ions at 600K in NBS1, NBS2 and NBS3.

Table 5. Table 5. Diffusivity of sodium ions (D_{Na}) and boron atoms (D_B) [unit x10^{-7} cm^2/sec] at 600K.

Glass	D_{Na}	D_B
NBS 1	0.374 ± 0.012	0.359 ± 0.016
NBS 2	0.235 ± 0.009	0.221 ± 0.013
NBS 3	0.190 ± 0.011	0.182 ± 0.007

Furthermore, the chemical durability was determined in terms of diffusivity of component species, estimated using mean square displacement (MSD) profiles[26]. The MSD of sodium ions for the simulated glasses at 600K is shown in Fig.8 and the respective diffusion coefficients (D) are shown in Table.5. The data show that the diffusivity of sodium (Na) ions is marginally higher than the boron (B) atoms as predicted from the role of B and Na as a network former and network modifier respectively. Boron atoms, being part of network chain are not able to move freely. On the other hand, Na being network modifier, doesn't participate in network formation and so move comparatively faster than network formers. The diffusivity of both the sodium ions and boron atoms was found to be maximum for NBS1 and minimum for NBS3. The highest diffusivity of the sodium for NBS1 is linked with the presence of maximum Na_2O content for NBS1. In particular, higher the amount of network modifies, more the network connectivity is disrupted, and greater mobility of constituent atoms can be expected. However, for the similar content of Na_2O in NBS2 and NBS3, the minimum diffusivity of sodium ions and boron atoms for NBS3 is supposed to be linked with the higher B_2O_3 presence. In fact, with increasing the B_2O_3 quantity, requirement of Na^+ ions as a charge compensator to BO_4 tetrahedrals increases. It is expected that Na ions are less mobile while participating as charge compensator than their role as network modifier. As a result, the minimum diffusivity of Na^+ ions for NBS3 was observed. The presented diffusion results might be very helpful in determining the chemical durability as well as the radiation stability of simulated glass compositions as shown by Grimes and coworkers[30,31].

Effect of Cs and Sr doping in NBS glass

Cs^{137} and Sr^{90} are known as the major heat-generating isotopes in the nuclear waste, study of which is important from the perspective of chemical and mechanical strength of vitrified glass as well as for medical applications[32,33]. Here, the NBS glass was doped with 5% and 10% (by mass) Cs and Sr atoms, named as NBS-5Cs, NBS-5Sr, NBS-10Cs, and NBS-10Sr respectively. The density and T_g of these glasses is shown in Table.6.

A decrease in T_g can be noted while doping with Cs/Sr due to overall increase in alkali content which opens the network structure and reduces the melting point of glass matrix. In line to the alkali content, T_g of Sr doped glass was found to be smaller than Cs doped glass. The results in Fig.9 (a) show nearly similar number of BOs with 5% doping of Cs/Sr, however, a major difference was noticed with 10% doping of Cs/Sr. In fact, the conversion of BO to NBO depends on the charge and radius of dopant. Larger the dopant radius, more conversion of BO to NBO is expected. Secondly, the

Table 6. Density and glass transition temperature of doped sodium borosilicate glass matrixes.

Glass	Density(*exp) [g/cm^3]	T_g (*exp)[K]
NBS	2.42 (* 2.4)	590 (* 560)
NBS-5Cs	2.49	
NBS-10Cs	2.56 (* 2.5)	545 (* 532)
NBS-5Sr	2.49	
NBS-10Sr	2.55 (* 2.6)	540 (* 526)
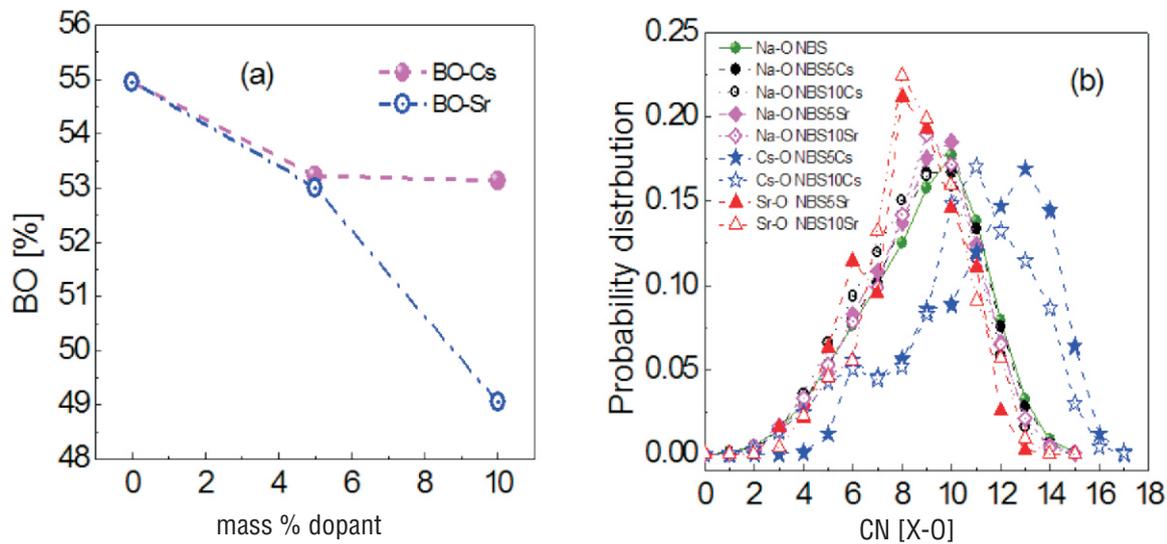
Fig.9: (a) BO and **(b)** coordination number distribution in NBS and doped NBS glass matrix.
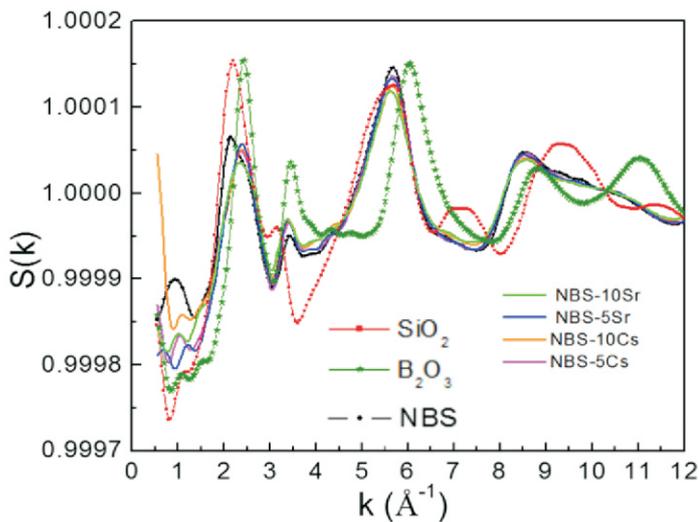
Fig.10: Structure factors for NBS glasses.

Fig.11: VDOS of NBS and doped NBS (NBS-10Cs and NBS-10Sr) and comparison with pure glass matrix of SiO$_2$ and B$_2$O$_3$.

dopants with higher charge will convert more BO to NBO; for example, with addition of one Cs atom only one BO will be converted to NBO; whereas presence of one Sr atom in glass matrix will convert two BOs in NBOs. Point to be noted is that the ionic radius of Cs (1.69 Å) is larger than Sr (1.33 Å), however, the charge of Cs (+1) is smaller than Sr (+2). Hereby, the ionic radius and charge on Cs and Sr interplay in the reverse direction. It seems that for lower concentration of dopants, the network connectivity is dominated by the ionic radius. However, for higher concentration of dopants (ex. 10% by mass), contribution of charges on dopants become more significant. Further, akin to other network formers, a wide spectrum for coordination number distribution was observed for Cs/Sr as shown in Fig.9 (b).

The effect of Cs and Sr doping on the intermediate range order of NBS glass was observed by structure factor (Fig.10), which showed noticeable effects in FSDP peaks of doped-NBS compared to base NBS. In particular, FSDP of NBS glass matrix were observed to split into sub-peaks while doping with Cs and Sr due to increase in alkali concentration. Another important observation was the difference in the intensity of peaks and dips, which were found to be in order of

NBS>NBS-5Sr~NBS-5Cs~NBS-10Cs>NBS-10Sr, in line to availability of the BOs.

Furthermore, the characteristic VDOS (Fig.11) showed only negligible differences for Cs/Sr doped NBS compared to the bare NBS. A minor post shift at 120 cm^{-1} and pre-shift at 1100 cm^{-1} for doped NBS compared to NBS was observed, which might be associated with the weakening of Si-O$_{BO}$-Si network and increasing Si-O$_{NBO}$ while doping. Also, one can notice the higher peak intensity at ~120 cm^{-1} for NBS matrix compared to pure matrix of SiO$_2$ and B$_2$O$_3$, and effects become more pronounced while doping of NBS with Cs and Sr, which might be associated with the increased bending and stretching motions of Si-O-Si while alkali addition.

Subsequently, the Arrhenius[34] semi-log plot of diffusivity lnD vs. 1/T was used to estimate the activation energy E_a, which were found to change while doping the NBS with Cs and Sr as shown in Table.7. In particular, the activation energy of sodium was reduced while doping or increasing the dopant concentration. Interestingly, the results show the activation energy of sodium, boron and dopants to be higher for Sr doped matrix than Cs doped matrix for doping

Table 7. Activation energy (unit eV) for migration of alkali ions and Boron atoms in NBS glass matrix and doped NBS matrix at temperature range 800K-1000K.

System	Na	Cs/Sr	B
NBS	0.942		1.065
NBS-5Cs	0.750	1.014	1.115
NBS-10Cs	0.622	0.925	0.999
NBS-5Sr	0.890	1.077	1.114
SBN10Sr	0.431	0.772	0.946

concentration of 5% by mass, however, the effects are reversed for doping concentration of 10%, where activation energy of elements was observed to be higher for Cs doped matrix than the Sr doped matrix. In real, the effects are more pronounced for Sr doping at 10%, which has been also observed while accounting of BOs in the doped NBS matrix.

Summary and Conclusion

In summary, the present article demonstrates that BKS potential model with the selected forcefield parameters can be utilized to simulate the glasses with varied composition. The results well capture the boron anomalies for varied concentration of network formers and network modifiers. Most importantly, the selected potential model and forcefield parameters not only well capture the structural distribution of glasses, but also validate the dynamic properties and characteristics vibration spectra. In addition, the validation of simulation data with the experimental observations assures the versatility of selected models for glasses of various compositions. The results establish the correlations between microscopic structure and macroscopic glass properties such as glass transition temperature, thermal expansion coefficient and mechanical integrity for glasses of varied composition. The MD results provide microscopic understanding of the glass structure and phenomena associated with the change in glass composition. The presented diffusion dynamics can be utilized to demonstrate the long-term leaching ability and radiation stability of these glasses.

The results might be very helpful in prediction of effects associated with the dopant's nature and concentration. Hereby, this article might have great academic as well technological significance for further guidance in composition selection of glass for various applications including nuclear waste immobilization.

Acknowledgement

Corresponding Author*

Sk. Musharaf Ali (musharaf@barc.gov.in)

References

[1] S. Al-Azzawi and F. Yasin, *Solar Wind Tech.*, 1985, **2**, 41-51.

[2] M.J. Plodinec, *Glass Technol-part A*, 2000, **41**, 186-192.

[3] C.P. Kaushik, *Procedia Mater. Sci.*, 2014, **7**, 16-22.

[4] H.K. Manaktala, An Assessment of Borosilicate Glass as a High-level Waste Form Nuclear Regulatory Commission Contract NRC-02-88-005 (CNWRA 92-017), San Antonio, Texas, 1992.

[5] L.-S. Du and J.F. Stebbins, *J. Phys. Chem. B* 2003, **107**, 10063-10076.

[6] S.W. Martin, A. Bhatnagar, C. Parameswar, S. Feller and J. MacKenzie, *J. Am. Ceram. Soc.*, 1995, **78**, 952-960.

[7] J.W. MacKenzie, A. Bhatnagar, D. Bain, S. Bhowmik, C. Parameswar, K. Budhwani, S.A. Feller, M.L. Royle and S.W. Martin, *J. Non-Crystal. Solids*, 1994, **177**, 269-276.

[8] A.A. Osipov, L.M. Osipova and V.E. Eremyashev, *Glass Phys. Chem.*, 2013, **39**, 105–112.

[9] Y. Yu, B. Stevensson and M. Edén, *J. Phys. Chem. C*, 2019, **123**, 25816–25832.

[10] A. Pedone, G. Malavasi, A.N. Cormack, U. Segre and M.C. Menziani, *Chem. Mater.*, 2007, **19**, 3144-3154.

[11] F. Gou, G.N. Greaves, W. Smith and R. Winter, *J. Non-Cryst. Solids.*, 2001, **293-295**, 539-546.

[12] B. Stevensson, Y. Yu and M. Eden, *Phys. Chem. Chem. Phys.*, 2018, **20**, 8192-8209.

[13] Y. Yu, B. Stevensson and M. Edén, *J. Phys. Chem. Lett.*, 2018, **9**, 6372–6376.

[14] T. Abe, *J. Am. Ceram. Soc.*, 1952, **35**, 284-299.

[15] A.C. Wright, *Phys. Chem. Glasses: Eur. J. Glass Science Technol. B*, 2010, **51**, 1-39.

[16] C.J. Phillips, *Glass Technol.*, 1964, **5**, 216-223.

[17] M.L. Williams and G.E. Scott, *Glass Technol.*, 1970, **11**, 76-79.

[18] N. Soga, *J. Non-Cryst. Solids.*, 1985, **73**, 305-313.

[19] B. Bridge, N.D. Patel and D.N. Waters, *Phys. Status Solidi A*, 1983, **77**, 655-668.

[20] S. Plimpton, *J. Comput. Phys.*, 1995, **117**, 1-19.

[21] B.W.H. v. Beest, G.J. Kramer and R.A. v. Santen, *Phys. Rev. Lett.*, 1990, **64**, 1955-1958.

[22] P. Sahu, S.M. Ali, K.T. Shenoy, S. Mohan, A. Arvind, G. Sugilal and C.P. Kaushik, *Phys. Chem. Chem. Phys.*, 2021, **23**, 14898.

[23] P. Sahu, A.A. Pente, M.D. Singh, I.A. Chowdhri, K. Sharma, M. Goswami, S.M. Ali, K.T. Shenoy and S. Mohan, *J. Phys. Chem. B*, 2019, **123**, 6290-6302.

[24] B.A. Luty and W.F.V. Gunsteren, *J. Phys. Chem.*, 1996, **100**, 2581–2587.

[25] L.-H. Kieu, J.-M. Delaye, L. Cormier and C. Stolz, *J. Non-Crystal. Solids*, 2011, **357**, 3313–3321.

[26] M.P. Allen and D.J. Tildesley, *Computer Simulation of*

Liquids, Clarendon Press, Oxford University, 2017.

[27] A.H. Verhoef and H.W. d. Hartog, *J. Non-Cryst. Solids*, 1992, **146**, 267-278.

[28] W. Kob and S. Ispas, *First-principles Simulations of Glass-formers*, 2016.

[29] L.-H. Kieu, J.-M. Delaye, L. Cormier and C. Stolz, *J. Non-Cryst. Solids*, 2011, **357**, 3313-3321.

[30] M. Bertolus, M. Freyss, B. Dorado, G. Martin, K. Hoang, S. Maillard, R. Skorek, P. Garcia, C. Valot, A. Chartier, L.V. Brutzel, P. Fossati, R.W. Grimes, D.C. Parfitt, C.L. Bishop, S.T. Murphy, M.J.D. Rushton, DragosStaicu, EugenYakub, SergiiNichenko, MatthiasKrack, FabienDevynck, RaoulNgayam-Happy, K. Govers, C.S. Deo and R.K. Behera, *J. Nucl. Mater.*, 2015, **462**, 475-495.

[31] K. Nordlund, S.J. Zinkle, A.E. Sand, F. Granberg, R.S. Averback, R.E. Stoller, T. Suzudo, L. Malerba, F. Banhart, W.J. Weber, F. Willaime, S. L. Dudarev and D. Simeone, *J. Nucl. Mater.*, 2018, **512**, 450-479.

[32] W.J. Weber, *Procedia Mater. Sci.*, 2014, **7**, 237-246.

[33] A. Vegiri, C.-P. E. Varsamis and E.I. Kamitsos, *J. Chem. Phys.*, 2005, **123**, 014508.

[34] S.A. Arrhenius, *Z. Phys. Chem.*, 1889, **4**, 96–116.

TECHNOLOGY

DEVELOPMENT
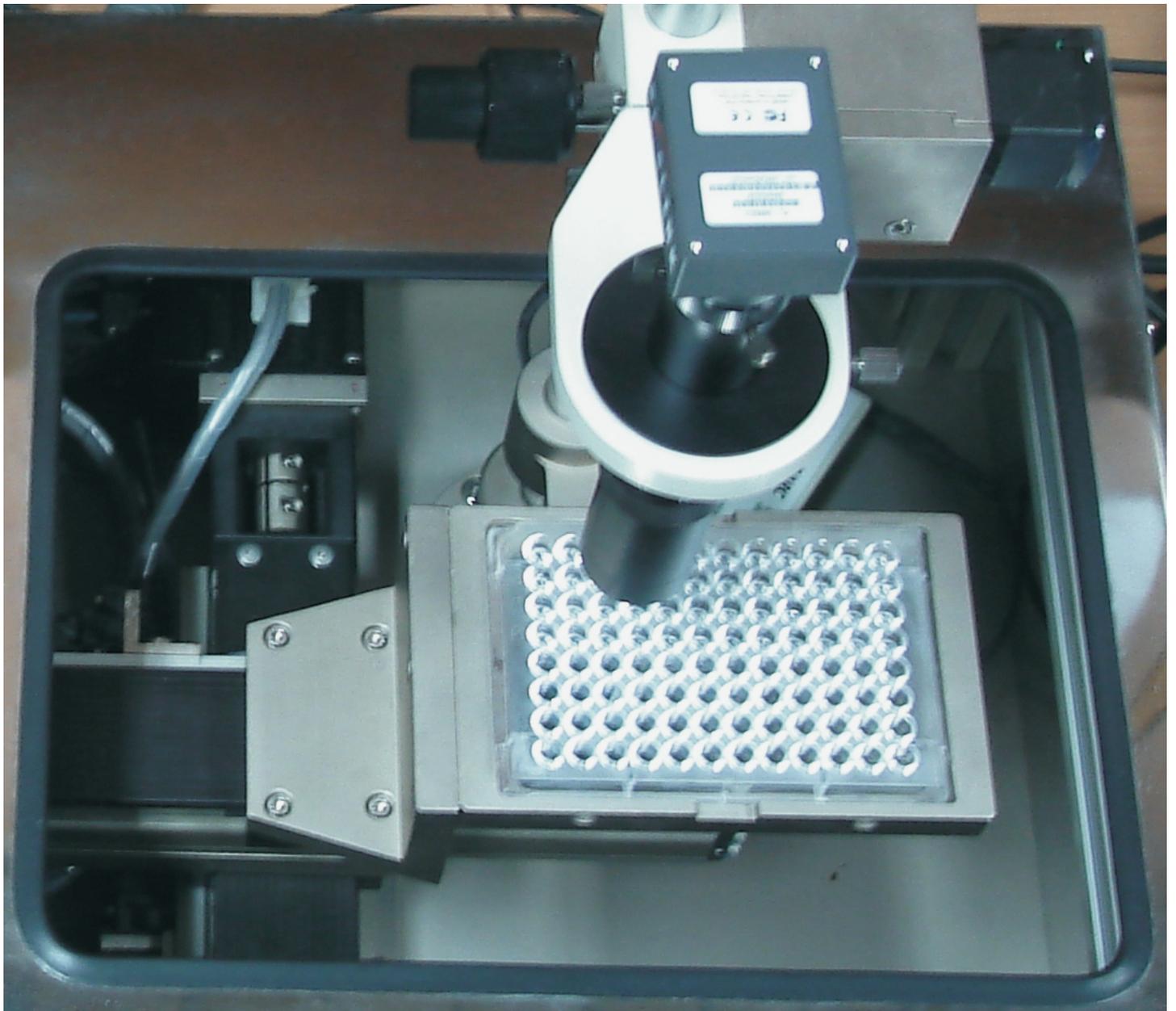
Imaging System

for Protein Crystallography

● High-resolution structures of biological macromolecules are essential for understanding diseases at molecular level

● The Protein Crystallization Imaging System helps monitor the progress of protein crystal growth during crystallization process

● Multi-focus images of protein crystals in multiple wells are captured by Imaging system

High-resolution structures of the biological macromolecules such as protein, DNA, RNA or their complexes are indispensable for understanding human disease pathways at the molecular level. This understanding is very important for rational drug design. Growth of single crystals of the biological macromolecules is often a bottleneck for macromolecular structure determination. It is difficult for researchers to predict exact conditions for formation of single crystals. Therefore, numerous crystallization trials are often required for a successful crystallization of biological macromolecules. Crystallization trials involve two important steps: a) Setting up the crystallization drops (typical volume 2 micro-litre) in 24 or 96 well plates by mixing equal volume of crystallization condition and solution of biological macromolecules; the setups are carried out using three different methods: hanging-drop, sitting-drop and under-oil microbatch. b) Monitoring crystallization drops during frequent intervals of time for checking the appearance of the single crystals. Various commercial systems have been developed for automation of the first step of the crystallization process [1]. While some limited automation systems are also available for monitoring the second step of the crystallization. All those automation systems are non-indigenous and maintenance of those systems is often costly and cumbersome. There are more than 100 research groups in India which use protein crystallography as a main technique for their structure determinations. Maintaining the records during second step of the crystallization process is often important for the reproduction of the successful crystallization trial which can be very well carried out by automation process. Due to non-availability of the affordable automated systems, the second step is often carried out manually in most of the laboratories. Moreover, some of the biological macromolecules are virus particles or toxic proteins which need to be handled by the automation system without human intervention for the bio-safety reasons. In view of these, we have designed and developed an indigenous protein crystallization imaging system for monitoring the growth of the single crystals, which deals with tasks of well control, image acquisition and analysis. Fig.1 depicts our developed protein crystallization imaging system (PCIS). Lysozyme protein crystals were grown using hanging drop, sitting drop and under-oil microbatch methods of crystallization. The crystal images from those drops as captured by PCIS are shown in Fig.2.

Image processing techniques are used to process the crystal images. Image segmentation and thresholding may help in determining the phase of crystallization. Useful distinguish features like high intensity, sharp boundaries can be extracted from segmented output. But usually due to noise or focusing issues, segmentation may not provide the expected output. Moreover, crystals inside a well are at a different depth of field. Therefore, multiple images of a single well at different depths are captured. Segmentation may be applied on each of these individual images or on a single focused stacked image.

Multiple focus depth images can be combined to form a single focus stack image to visualize all the crystals of well in a single image. Focus stacking is achieved by fusing different in-focus features from multi-depth images [2]. Features extracted with segmentation and thresholding may be used to classify the images into different categories of crystallization process (crystal, clear, precipitate etc.) [3]. A visualization of morphologically good quality crystals by imaging system is essential tool for protein crystallography.

We have developed a complete pipeline from well images capturing to image analysis to retrieval and storage. This paper is structured as follows. Section II elaborates the hardware and design features of the developed system. In Section III, different image analysis algorithm implemented for image fusion and filtering are discussed. In Section IV, software features are discussed.
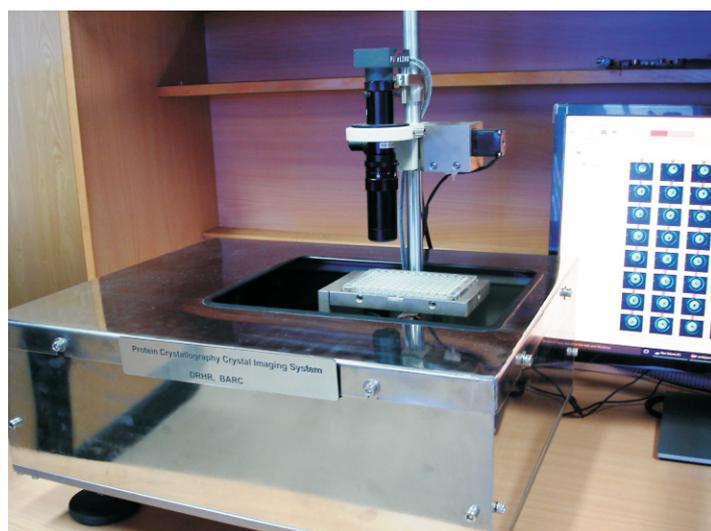
Fig.1: Protein crystallization Imaging System (PCIS).

This article was contributed by
[1]*Ratnesh S. Sengar*,* [2]*Rohit Sharma,* [3]*Ravindra D. Makde*
[1,2]*Division of Remote Handling & Robotics, BARC*
[3]*Beamline Development & Application Section, BARC*
*Corresponding Author email: rssengar@barc.gov.in
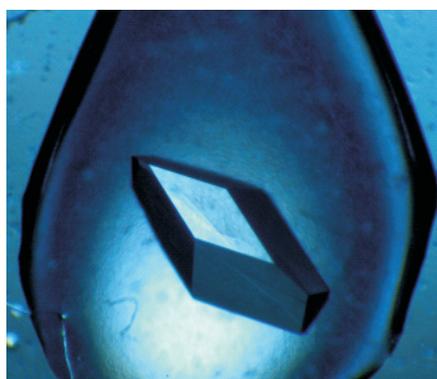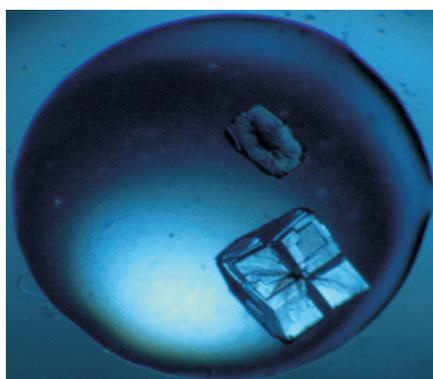
| Crystal Image I | Crystal Image II | Crystal Image III |
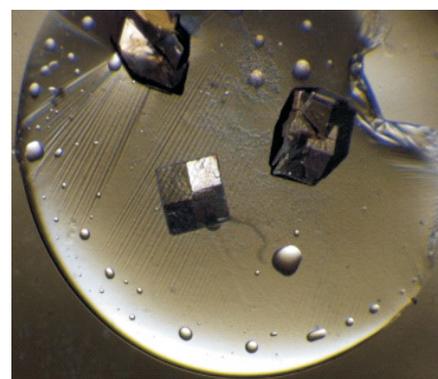
Fig.2: Crystallization drops as captured by PCIS.

The monitoring of microscopic size of crystals in 24/96 well by robotic imaging system demands very high accuracy. Various design considerations and the quality parameters to be accessed while monitoring crystals are also discussed in subsequent sections.

Hardware and design features

The important considerations while designing a precise imaging system for crystal monitoring are: a) micron level motion accuracy at a scale of 120mmx 120mm x 50mm with minimum vibration and b) automatic acquisition and visualization of multi-focal images of macromolecular protein crystals in standard multi-well crystallization plate. We achieved this by using a well damped table, grounded linear guides, servo motors with absolute encoders and custom designed high-resolution microscopic imaging system with image processing algorithms. The entire assembly is precisely leveled, while the frame structure below the table is utilized to hold the control panel. Typical setup for a crystallization imaging system involves number of components which are as follows:

a) *High resolution microscopic imaging system*: A camera and zoom lens is mounted on rack and pinion mount. Motor is coupled with rack and pinion mount to capture multi-focus images at different depth of a drop with different magnifications. A limit switch is placed on top of rack pinion mount for homing of imaging system which helps to calibrate the image and auto focusing of each well of crystallization plate.

b) *Customized illumination control to locate the drop*: 100% diffused light source with collimated optics is designed to focus all the crystallization drops without reflection.

c) *Robotic stages*: The robotic stage has a motion travel of 120mmx120mm in X and Y directions. A grounded linear guide is used to reduce the backlash error in each axis. A compact servo motor with absolute encoder is used for precise motion.

d) *Plate handler*: It holds standard crystallization plates of 24/96/384 wells. Inside the boundary of plate handler switch locator is provided to avoid the movement in the plate and precisely locate the drop in each well by illuminator.

e) *Control system for robotic stages and microscopic imaging system*: A realistic dynamic model of the robotic system is constructed [4] and tuned for stable operation in each axis. The position, speed and current loop compensators are implemented as software-based lead, lag compensator and notch filter. The corresponding bandwidth is achieved in position loop 40Hz, speed loop 100hz and current loop 1200Hz.

Image processing and feature extraction

Imaging of the crystallization drops in multi-well plate is challenging due to following reasons:

♦ Images may be captured under different illumination; therefore, global threshold segmentation algorithms do not work on these images [1].

♦ Crystals may appear at different depth of field in crystallization drop (typical drop volume of 2 microlitre) and entire drop cannot be focus at the same time due to optical limit of cylindrical zoom lens. Hence, auto-focus and real time image fusion algorithms are required on multi-focus images to maximise the depth of field.

♦ Sizes and number of crystals vary in a particular crystallization drop. Different Images captured at different phases of crystal growth may have varying shape and intensities. This poses a challenge in crystal classification.

These above challenges posed by protein crystal imaging lead us to propose different imaging steps and image classification methods. Each method provides different insights into the problem and significant improvements in the crystallization methods. Image segmentation plays a big role in image classification to find out the robust features for training the classification model.

Image segmentation plays a big role in image classification to find out the robust features for training the classification model

Image denoising

Protein crystal images contain features that are about 10-300 microns in size and having sharp boundaries. Sometimes, non-linear background and noise makes it difficult to extract the features from crystal images. Therefore, prior to feature extraction, image filtering is applied to remove noise from the image [1]. Traditional denoising techniques like Box filter, fourier transform, wavelet transform fail to denoise the crystal image. Either the image is blurred or sharp features are smoothened out. We compared different denoising algorithms in spatial as well as transform domain and found that for denoising of protein crystal images, anisotropic diffusion median (AMD) [6] results better in terms of SNR as well as in universal quality index.

Perona and Malik [5] anisotropic diffusion equation for noisy image I is given in below equation.

$$I_t = div(c(x,y,t)\nabla I) = c(x,y,t)\Delta I + \nabla c \cdot \nabla I \qquad (1)$$

where div is the divergence operator, Δ is the Laplacian operator and ∇ is the gradient operator and c(x, y, t) is diffusivity function. Anisotropic diffusion median (AMD)[6] incorporates a median filter into a diffusion step and works as a hybrid filter that achieves much better noise suppression with minimum edge blurring than any other diffusion algorithms. Diffusivity function for AMD is chosen as Tukey biweight function [9]. Tukey biweight function is given in below equation.

$$c(\nabla I, K) = \begin{cases} \frac{25}{16K}\left[1 - \left(\frac{\nabla I}{\sqrt{5}K}\right)^2\right]^2, & |\nabla I| \leq \sqrt{5}K \\ 0 & otherwise \end{cases} \qquad (2)$$

Where K acts as threshold and is constant as is tuned for particular application.

$$I_{i,j}^{n+1} = Median(I_{i,j}^{n+1}, W) \qquad (3)$$

W is the window for median operator. This diffusion algorithm converges in a smaller number of steps, thus makes it suitable for real time implementation.

The best SNR achieved on protein crystal images by diffusion methods, resulted in an improvement in feature extraction of crystals and classification of crystallization trails.

Feature extraction using image segmentation

Image thresholding techniques aid the segmentation algorithm by converting the image to binary image. Global thresholding works by maximizing the variance between the classes.

Ostu [7] technique works by finding the optimal threshold. But this is not always possible to find the distinctive peaks. Unlike global thresholding, local thresholding [1] works by analysing the features in local neighbourhood of image. This leads to increase in complexity and for poor illuminated images local thresholding may incorrectly classify background and foreground pixels. Gradient based image segmentation may give inaccurate results in poorly illumined images. Region-based segmentation combines similar pixels by region growing and gives promising results. Usually, region-based segmentation may involve user intervention e.g. by providing markers and may not be suitable for automated crystal image segmentation. Wavelet based image segmentation is a multi-resolution transform domain image segmentation technique which first decompose the image into high pass and low pass coefficients. Wavelets have limited frequency support and find features only in limited directions. We have implemented a contourlet-based multiresolution, multidirectional segmentation algorithm [8] to extract various features associated with crystals.

Image fusion or focus stacking

In-focus features extracted from segmentation algorithm of multi-depth images needed to be fused together to form a single composite fused image. Pixel based fusion algorithms uses maximum selection criteria by comparing the pixel values of all images and selects the maximum one.

Neighbourhood based fusion algorithms are based on utilizing the neighbourhood pixels within a fixed window [2]. Froster et al. proposed a complex wavelet transform based image fusion algorithm. Multiscale image fusion [2][10], data driven image fusion give better results but might leads to brightness distortions. A guided filter fusion [9] (GFF) method based on guided filtering is computationally efficient and can be used in real time applications but this algorithm also leads to brightness and contrast distortions. To overcome these limitations, we have proposed a fusion algorithm with combination of non-subsampled wavelet transform (NSWT) and guided filter.

A contourlet-based multi-resolution, multi-directional segmentation algorithm was implemented to extract various features associated with crystals
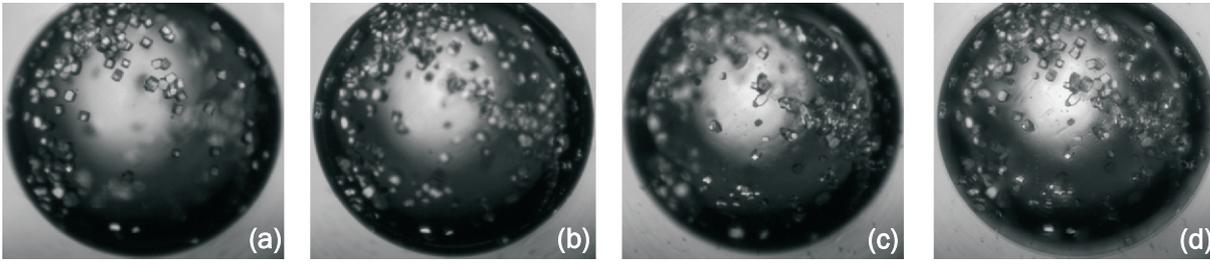
(i) Images (a-c) captured with different depths of focus and (d) is final fused image.
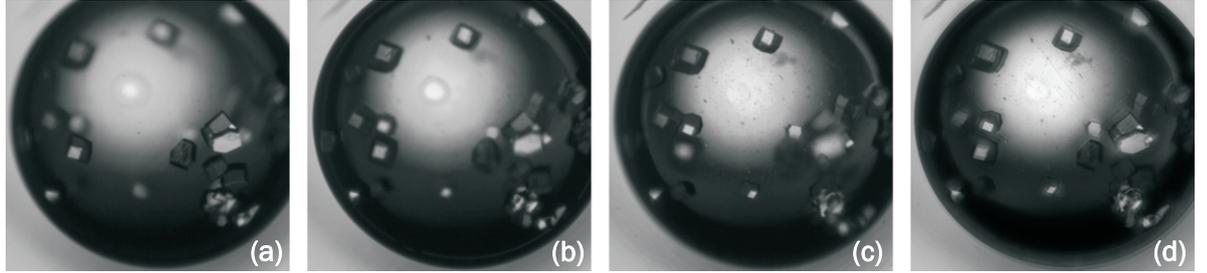
(ii) Images (a-c) captured with different depths of focus and (d) is final fused image.

Fig.3: Fusion algorithm results for two wells images captured with different depth of focus.

Our Proposed algorithm

The source input images are first decomposed using forward non subsampled wavelet transform (NSWT) [8]. Input image is decomposed to an approximation image and detail directional images using directional filter banks (DFBs). The discrete NSWT of source image I(x,y) of size MxN is given by:

$$W_\Phi^k(j_o, m, n) = \frac{1}{\sqrt{MN}} \sum_{x=0}^{M-1} \sum_{y=0}^{N-1} I^k(x,y) \Phi_{j_o,m,n}(x,y) \quad (4)$$

$$W_\psi^{k,i}(j_o, m, n) = \frac{1}{\sqrt{MN}} \sum_{x=0}^{M-1} \sum_{y=0}^{N-1} I^k(x,y) \psi_{j_o,m,n}^i(x,y),$$
$$i = \{H, V, D, ...\} \text{ and } j \geq j_o \quad (5)$$

$I^k(x,y)$ is k^{th} source image and $W_\varphi^k(j_o, m, n), W_\psi^{k,i}(j_o, m, n)$ are approximation and details coefficients for direction $i = \{H, V, D, ...\}$ respectively. j_o is starting scale and Φ, Ψ are scaling and wavelet function respectively. H, V, D are horizontal, vertical and diagonal directions respectively. Weight map is constructed by performing guided filtering on each bandpass image with source image as a guidance image.

$$W_B^k = G_{r_1,\epsilon_1}(W_\Phi^k, I^k) \quad , \quad W_D^{k,i} = G_{r_2,\epsilon_2}(W_\psi^{k,i}, I^k) \quad (6)$$

$r_1, \epsilon_1, r_2, \epsilon_2$ are parameters of guided filter G and are determined empirically. W_B^k and $W_D^{k,i}$ are refined weights of approximation and detail coefficients respectively and these weights are normalized. Approximation and details coefficients of different input images are fused together by weighted averaging.

$$\overline{W_\Phi^k(j_o, m, n)} = \sum_{k=1}^K W_B^k \, W_\Phi^k(j_o, m, n) \quad , \quad \overline{W_\psi^{k,i}(j_o, m, n)} = \sum_{k=1}^K W_D^{k,i} \, W_\psi^{k,i}(j_o, m, n) \quad (7)$$

Then, final fused image F(x,y) is found by applying inverse NSWT (INSWT) to refined coefficients $\overline{W_\Phi^k(j_o, m, n)}$ & $\overline{W_\psi^{k,i}(j_o, m, n)}$

$$F(x,y) = \frac{1}{\sqrt{MN}} \sum_m \sum_n \overline{W_\Phi^k(j_o, m, n)} \Phi_{j_o,m,n}(x,y)$$
$$+ \frac{1}{\sqrt{MN}} \sum_{i=H,V,D} \sum_{j=j_o}^{\infty} \sum_m \sum_n \overline{W_\psi^{k,i}(j_o, m, n)} \psi_{j_o,m,n}^i(x,y) \quad (8)$$

Experiments were performed on multiple images captured by our system and we have found that our proposed algorithm works better than other existing algorithms like Focus All [2], GFF [9], HOSVD [10], NSCT on the basis of quality index. Fused image output from our proposed algorithm is shown in Fig.3.

Crystal size measurement

Actual crystal shape and size can aid researchers to analyse the crystal quality for X-ray diffraction studies. Physical size calculation is not a trivial task and is limited by zoom-lens and focus setting. Existing zoom-lens calibration methods usually employ precisely measured targets as ground truth. Fraser and Al Ajlouni [11] used a 3D control field for zoom-lens calibration comprised of a 140 object point array covering an area of about 5m × 3m. In close-range computer vision applications using zoom-lens cameras, the lens and focus settings are subject to frequent changes, and this leads to frequent calibration which is not feasible and inefficient.

We have developed a flexible method to calibrate a zoom-lens camera. We have used a NIST certified calibration target

> *Actual crystal shape and size can aid researchers to analyse the crystal quality for X-ray diffraction studies.*
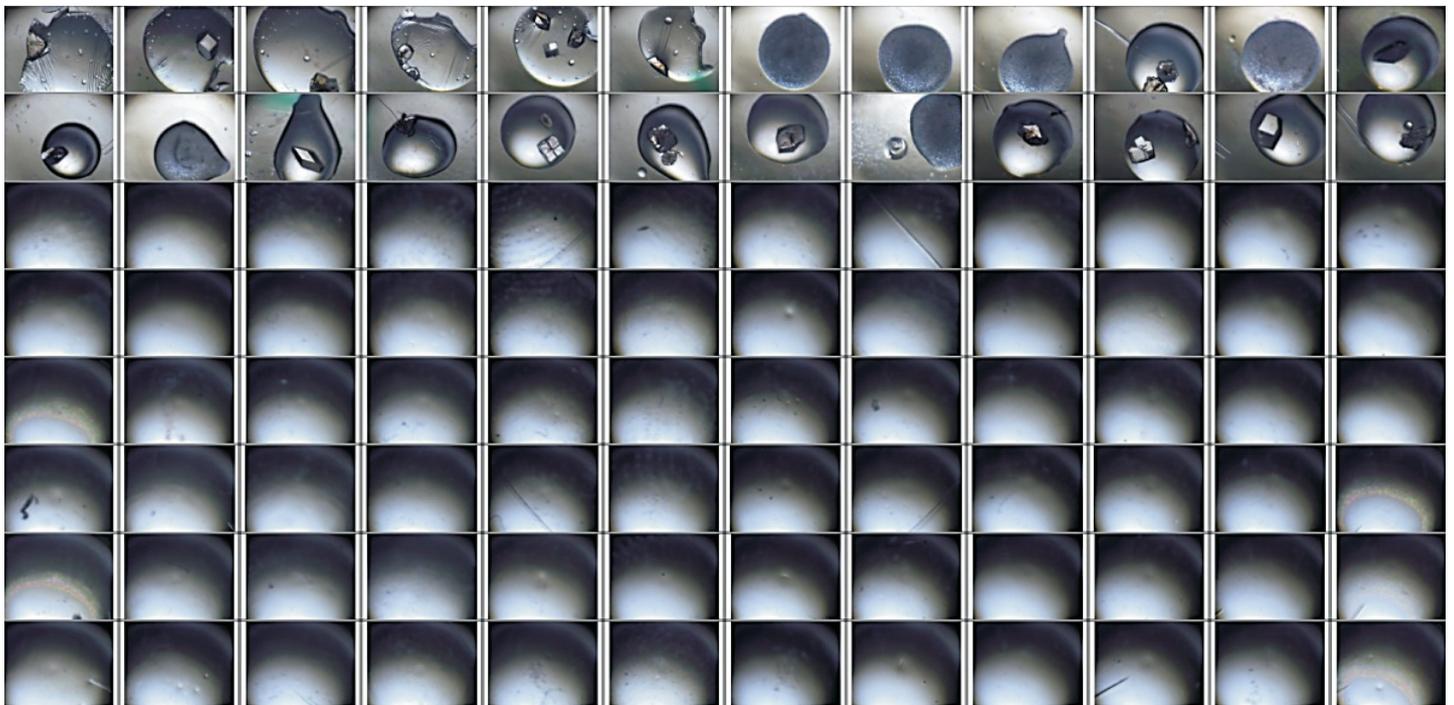
Fig.4: Crystallography software graphical user interface.

to calibrate zoom camera. First, multiple images of calibration target at different zooms and different heights are captured. A physical to pixel coordinates mapping is calculated. A multivariable linear regression model has been built using this data. Model coefficients are saved to a configuration file. Real time crystal size is estimated using these model coefficients. Accuracy of this model is established by comparing the actual size and calculated size. The error is less than 10 microns.

Protein crystallography imaging software

User friendly, intuitive, multithreaded, modular, robust, control and analysis software is developed by incorporating all the algorithms discussed in the previous sections. The software is developed by keeping in view the best practises followed in industry. Software main graphical user interface is shown in Fig.4.

Some of the features of software are given below (crystal vision software). Software provides seamless integration with hardware. Automatic scheduling is managed through the software. User can inspect the crystals in a well plate at any time by manual controls provided in the software. User can fine tune settings to improve the imaging accuracy. Once, control module has captured images. These images can be viewed in an image view.
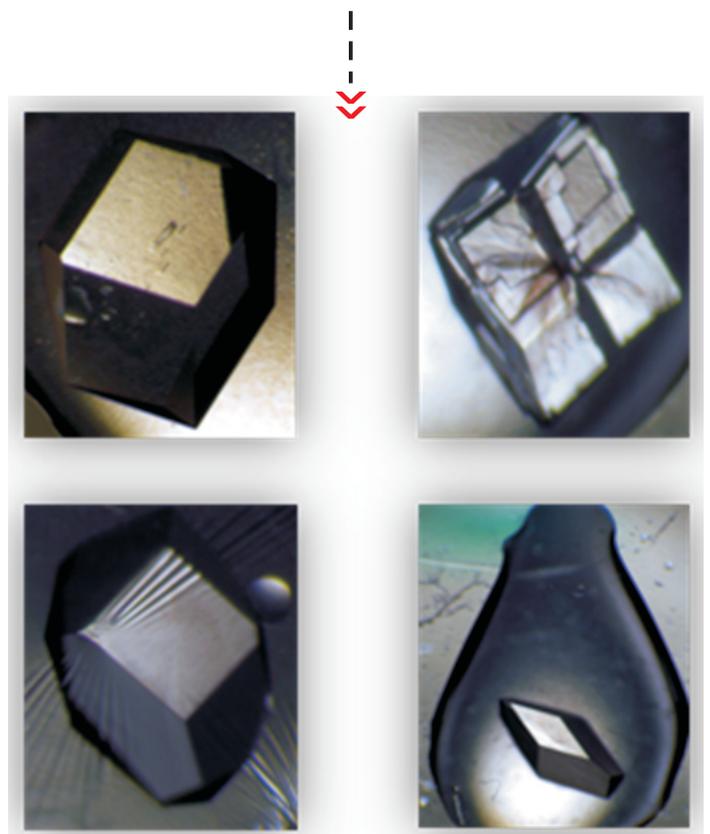
CRYSTAL VISION SOFTWARE - FEATURES

Control	Analysis	GUI
Robotic control	Autofocus algorithm	Workspace management (Project and experiment)
Well configuration and calibration	Feature extraction	Image viewing and comparison mode (canvas, well, drop)
Camera control	Image fusion	Image storage and retrieval
Manual movement module	Crystal classification	Job scheduler

Conclusion

The protein crystal imaging system (PCIS) is an attempt to indigenously develop high throughput system for monitoring the crystal growth in crystallization drops during the crystallization process. This facilitates the research using x-ray crystallography in the area of structural biology and rational drug discovery. Here, we described the design and implementation of standalone real-time, affordable system for protein crystallization image acquisition. High resolution imaging system coupled with diffused illumination light source and robotic stages provides support for imaging of a single wellplate of customizable configurations. Images at different depth for each well at different intervals of time are captured and stored in the database. Image analysis is carried out on crystal images. Comparison of different denoising algorithms yields the anisotropic diffusion-based algorithm the right choice for the crystal images. Focus stacked images of each well are fused together by powerful, fast and efficient NSCT-guided fusion algorithm. Advantage of this algorithm lays in efficiency and minimal brightness distortions. Image acquisition and processing for a 96 well plate take less than 12 minutes, hence greatly reducing manual inspection of the crystallization plate. Correct classification of images into crystals and non-crystals can further reduce the unnecessary inspection of the plate. As future work, we intend to develop a convolutional neural network (CNN) to classify the images into different categories.

References

[1] Pusey, Marc & Aygun, Ramazan, "Data Analytics for Protein Crystallization", 2017, 10.1007/978-3-319-58937-4.

[2] M.S. Sigdel, M. Sigdel, S. Dinç, I. Dinc, M.L. Pusey and R.S. Aygün, "FocusALL: Focal Stacking of Microscopic Images Using Modified Harris Corner Response Measure," in IEEE/ACM *Transactions on Computational Biology and Bioinformatics*, 2016, Vol. **13**, 2, 326-340, doi: 10.1109/TCBB.2015.2459685.

[3] Bruno, E Andrew *et al*. "Classification of crystallization outcomes using deep convolutional neural networks." *PloS one*, 2018, Vol.**13**, 6e0198883. doi:10.1371/journal.pone.0198883.

[4] Ogata Katsuhiko, "Modern control system" Prentice Hall, 1992.

[5] Pietro Perona and Jitendra Malik, "Scale-space and edge detection using anisotropic diffusion" (PDF). *IEEE Transactions on Pattern Analysis and Machine Intelligence,* 1990, Vol.**12,** 7, 629–639. doi:10.1109/34.56205.

[6] H. Ling and A.C. Bovik, "Smoothing low-SNR molecular images via anisotropic median-diffusion," in *IEEE Transactions on Medical Imaging*, 2002, Vol. **21**, 4, 377-384. doi:10.1109/TMI.2002.1000261.

[7] N. Otsu, "A Threshold Selection Method from Gray-Level Histograms," in *IEEE Transactions on Systems, Man, and Cybernetics*, 1979, Vol. **9**, 1, 62-66. doi: 10.1109/TSMC.1979.4310076.

[8] L. da Cunha, Jianping Zhou, and Minh N. Do, "The non subsampled contourlet transform: theory, design, and applications," *IEEE Transactions on Image Processing,* 2006, Vol. **15**, 10, 3089–3101.

[9] S. Li, X. Kang and J. Hu, "Image Fusion With Guided Filtering," in *IEEE Transactions on Image Processing*, 2013, Vol. **22**, 7, 2864-2875. doi:10.1109/TIP.2013.2244222.

[10] J. Liang , Y. He , D. Liu , X. Zeng ," Image fusion using higher order singular value decomposition", *IEEE Transactions on Image Processing*, 2012, Vol. **21**, 5, 2898-2909. doi:10.1109/tip.2012.2183140.

[11] C.S. Fraser, and S. Al-Ajlouni, "Zoom-dependent camera calibration in digital close-range photo grammetry", *Photogrammetric Engineering & Remote Sensing*, 2006, Vol. **72, 9**, 1017–1026.

RESEARCH SYNOPSIS

Cells *expressing fusion protein*

Cell-free *matrix with fusion protein*

Gene for domains of S-layer protein
Gene for MT/PhoN
Metal ion
Fusion protein
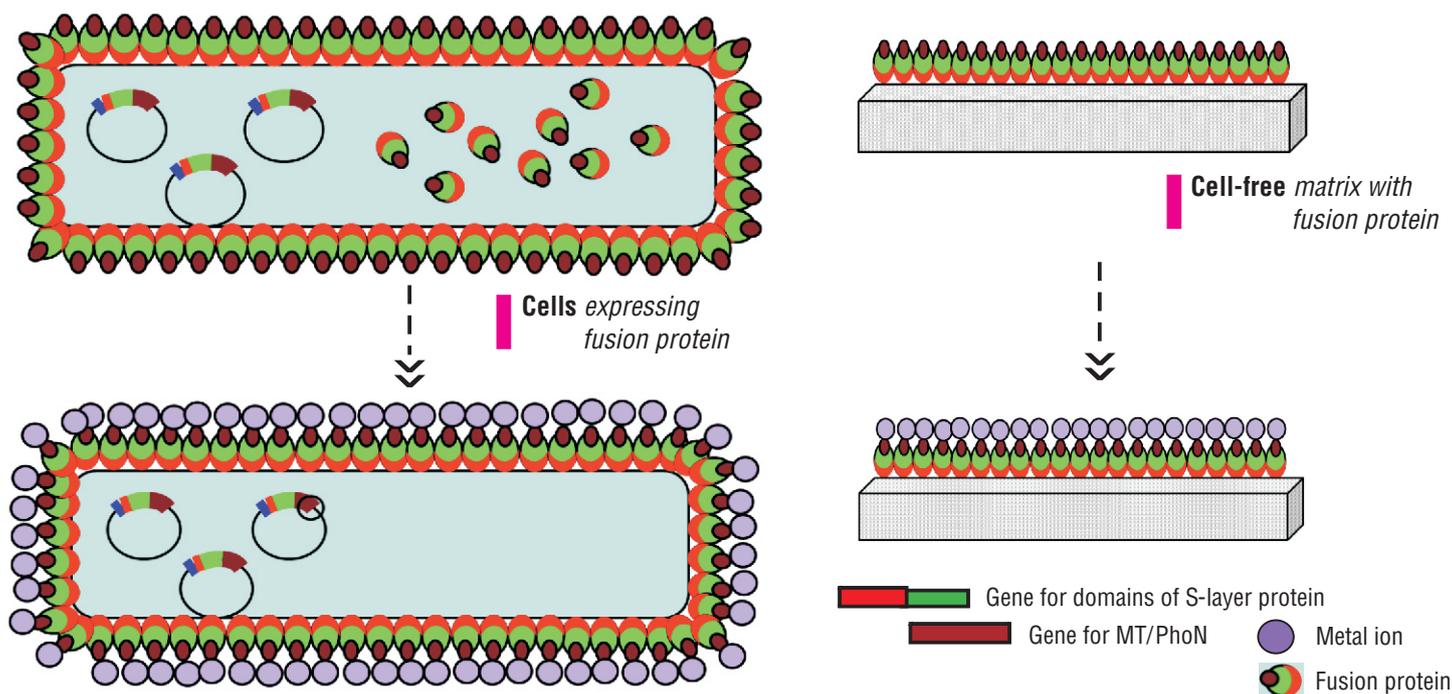
Fusion proteins for
enhanced metal bioremediation

The genetically modified cells of Deinococcus radiodurans genetically modified to display SmtA on cell surface could remove three-fold more cadmium from solution compared to cells expressing SmtA inside the cell

*This article was contributed by Chitra Seetharam Misra Applied Genomics Section Bioscience Group, BARC *Corresponding Author email: chitras@barc.gov.in*

Heavy metal pollution is a difficult problem, since unlike other pollutants, heavy metals cannot be destroyed, but only removed, concentrated or converted into non-toxic forms. Living forms possess several metabolic processes which either sequester heavy metals or convert them to non-toxic forms. Bioscience Group has been investigating microbes for metal remediation.

In a recent article, (C.S. Misra *et al*., 2021,'Metal removal by metallothionien (MT) and an acid phosphatase PhoN, surface-displayed on the cells of the extremophile, *Deinococcus radiodurans'*, Journal of Hazardous Materials, 419:126477) we reported the enhanced loading of Cd onto bacterial cell surface using surface display technique. This study reported the generation of a fusion protein consisting of Hpi and SmtA. Here, SmtA is a metallothionine, that is specialized to mop up metal ions such as cadmium and zinc from solutions and Hpi is a Surface Layer Protein (S-layer protein) that can form a densely-packed array on the cell surface (above image). Cells of Deinococcus radiodurans genetically modified to display SmtA on cell surface could remove three-fold more cadmium from solution compared to cells expressing SmtA inside the cell.

Additionally, we reported the construction of another fusion protein embedded into peptidoglycan, an inert cell wall matrix. This new material, called SPhoNP (above image) could precipitate uranium from 1 mM solution for up to five cycles, leading to a final U loading of 160mg U/g dry mass. The work demonstrates the utility of whole cell-based material and cell-free preparations for cadmium sequestration and uranium removal using recombinant DNA technology and surface-display approach*.
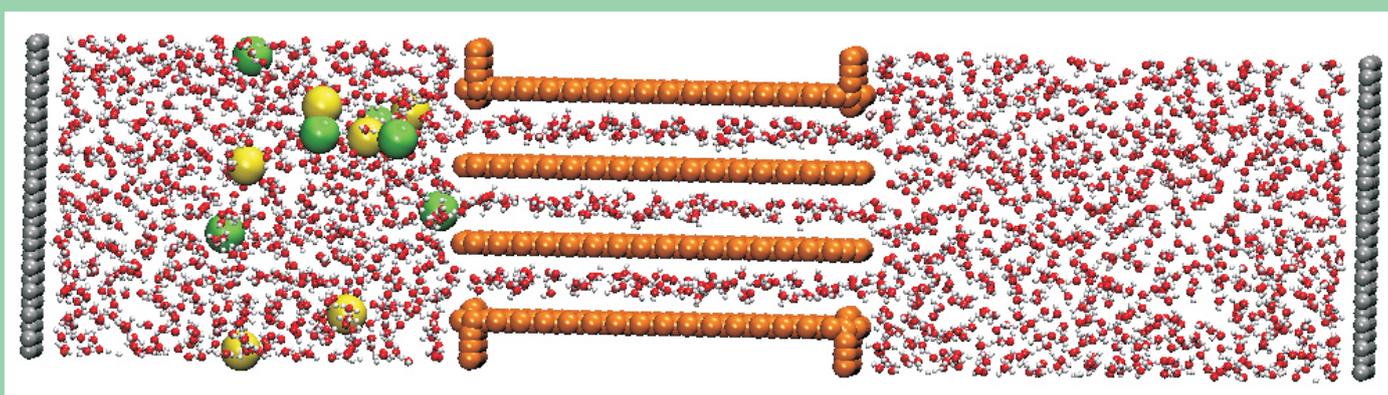
Water permeation through nanomembrane